PhD Thesis

Mads Lawaetz

uPAR-targeted molecular imaging of head and neck squamous cell carcinoma

Supervisors: Christian von Buchwald, Andreas Kjaer and Anders Christensen

This thesis has been submitted to the Graduate School of Health and Medical Sciences, University of Copenhagen 19th of March 2024

Name of department: Department of Otolaryngology, Head and Neck Surgery and Audiology, Rigshospitalet, Copenhagen University Hospital, Copenhagen, Denmark

Author: Mads Lawaetz; MD

Title: uPAR-targeted molecular imaging of head and neck squamous cell carcinoma

Principal supervisor: Christian von Buchwald; Professor, DMSc, MD

Department of Otolaryngology, Head and Neck Surgery and Audiology, Rigshospitalet, Copenhagen University Hospital, Copenhagen, Denmark

Primary co-supervisor: Andreas Kjær; Professor, PhD, DMSc, MD

Department of Clinical Physiology and Nuclear Medicine and Cluster for Molecular Imaging, Copenhagen University Hospital - Rigshospitalet & Department of Biomedical Sciences, University of Copenhagen, Copenhagen, Denmark

Secondary co-supervisor: Anders Christensen; Associate Professor, PhD, MD

Department of Otolaryngology, Head and Neck Surgery and Audiology, Rigshospitalet, Copenhagen University Hospital, Copenhagen, Denmark

Submitted on: 19th March 2024

Table of contents

Preface and acknowledgements

During the end of my post-graduate specialty education in oto-rhino-laryngology, Christian von Buchwald and Andreas Kjaer offered me the opportunity to start this PhD project, which was initiated as a collaboration between the Department of Otolaryngology, Head and Neck Surgery and Audiology and the Department of Clinical Physiology and, Nuclear Medicine and Cluster for Molecular Imaging (CMI), Copenhagen University Hospital, Rigshospitalet. I would like to thank Christian von Buchwald and Andreas Kjaer for giving me this chance and providing the framework and interdisciplinary network for performing my Ph.D. Working with you has been inspiring and I appreciate your style of leadership with balanced freedom and responsibility. You have made it possible to conduct three studies involving basic research, preclinical studies with the establishment of new animal models and a clinical trial with a novel radiotracer developed at CMI. The completion of these studies is partly attributable to Kirstine Karnov, who was instrumental in launching two of them. Sadly, she passed away before the projects were finished. Our thoughts are with her and her family.

Completing these studies would not have been possible without the contribution from several co-workers. At the Department of Otolaryngology, Head and Neck Surgery and Audiology, I would like to thank Anders Christensen for clinical guidance and introduction to the field of molecular imaging, Eva Lykke for collaboration with the establishment of animal models, Vivian Sønnicksen for her kindness and administrative support and Mads Klokker for supporting the professional research environment in the department. At the Ph.D. office I would like to thank my fellow PhD students for their support, discussions and for making the office a fun and pleasant workplace.

At the Department of Pathology, I would like to thank Anne-Marie Fiehn for help with immunohistochemistry and special thanks to Giedrius Lelkaitis for always being accessible for guidance and advice on how to optimize immunohistochemistry, digital pathology, and establishment of PDX-models. At CMI I would like to thank the whole

group of dedicated scientists for the warm welcome into the research unit. A special thanks to Tina Binderup and Karina Juhl for introducing me to the many disciplines of basic research, including immunohistochemistry, autoradiography, animal research and small animal PET-imaging. Furthermore, I would like to extend my gratitude to Anne Mette Fisker Hag, Line Knudsen and Katrine Qvist.

Lastly, I want to express my sincere appreciation to my family. My loving wife Trine who has managed to maintain love, humor, and balance in our family in times with heavy workload. Beyond this role, you always challenge the conventional way of thinking, asking curious and clever questions making me reconsider and refine my ideas. I also want to thank my three wonderful sons, Alfred, Conrad, and Walter for being the best distraction and a constant source of joy. Your presence always gives me a greater meaning in life.

Mads Lawaetz, January 2024

List of manuscripts

Paper I

Lawaetz M, Christensen A, Juhl K, et al. Potential of uPAR, αvβ6 Integrin, and Tissue Factor as Targets for Molecular Imaging of Oral Squamous Cell Carcinoma: Evaluation of Nine Targets in Primary Tumors and Metastases by Immunohistochemistry. Int J Mol Sci. 2023;24(4):3853. doi:10.3390/ijms24043853

Paper II

Lawaetz M, Christensen A, Juhl K, et al. Diagnostic Value of Preoperative uPAR-PET/CT in Regional Lymph Node Staging of Oral and Oropharyngeal Squamous Cell Carcinoma: A Prospective Phase II Trial. Diagnostics. 2023;13(21):3303. doi:10.3390/diagnostics13213303

Paper III

Lawaetz M, Binderup T, Christensen A, et al. Urokinase-Type Plasminogen Activator Receptor (uPAR) Expression and [64Cu]Cu-DOTA-AE105 uPAR-PET/CT in Patient-Derived Xenograft Models of Oral Squamous Cell Carcinoma. Mol Imaging Biol. 2023;25(6):1034-1044. doi:10.1007/s11307-023-01858-x

Abbreviations

^{18}F	Fluorine-18
^{64}Cu	Copper-64
^{68}Ga	Gallium-68
AE105	Asp-Cha-Phe-(D)Ser-(D)Arg-Tyr-Leu-Trp-Ser-CONH2
CT	Computed Tomography
DAHANCA	Danish Head and Neck Cancer Group
DOTA	1,4,7,10-tetraazacyclododecane-1,4,7,10-tetraacetic acid (($CH_2CH_2NCH_2CO_2H)_4$)
EGFR	Epidermal Growth Factor Receptor
ECM	Extracellular matrix
EpCAM	Epithelial Cell Adhesion Molecule
[^{18}F]FDG-PET	2-deoxy-2-[^{18}F]fluoro-D-glucose positron emission tomography
FFPE	Formalin-Fixed Paraffin-Embedded
[^{18}F]FLT	3'-Deoxy-3'-[^{18}F]fluorothymidine
[^{18}F]FMISO	[^{18}F]F-fluoromisonidazole
GPI	Glycosylphosphatidylinositol
HNSCC	Head and Neck Squamous Cell Carcinoma
HPV	Human papillomavirus
H-score	Histochemical Score
IHC	Immunohistochemistry
MRI	Magnetic Resonance Imaging
MBq	Mega Becquerel
mSv	Millisievert
N0 neck	Clinical negative neck

NMRI	Naval Medical Research Institute
NOTA	1,4,7-triazacyclononane-1,4,7-triacetic acid $(C_{12}H_{21}N_3O_6$-3HCl)
OPSCC	Oropharyngeal Squamous Cell Carcinoma
OSCC	Oral Squamous Cell Carcinoma
PARP-1	Poly (ADP-ribose) Polymerase 1
PET	Positron Emission Tomography
PDX	Patient-Derived Xenograft
SUV	Standardized Uptake Value
uPAR	Urokinase-type Plasminogen Activator Receptor
VEGFR1	Vascular Endothelial Growth Factor Receptor 1
VEGFR2	Vascular Endothelial Growth Factor Receptor 2

Summary in English

Imaging is essential for staging and treatment planning of head and neck cancer, particularly oral and oropharyngeal cancer. Traditional imaging modalities, like computed tomography (CT) and magnetic resonance imaging (MRI), have several limitations, including diagnostic accuracy in the identification of lymph node metastases and delineating tumor tissue in pre-treated patients. 2-deoxy-2-[^{18}F]fluoro-D-glucose positron emission tomography ([^{18}F]FDG-PET) has an important role in posttreatment evaluation in head and neck squamous cell carcinoma (HNSCC) but lacks the sensitivity for staging and surgical planning. Molecular imaging has gained increasing interest in recent years due to the ability to target specific biomarkers in tumor tissue and provide earlier and more precise information than morphological imaging. This may contribute to the comprehension of cancer biology and enhance the diagnosis and treatment of HNSCC. Several biomarkers have been investigated in HNSCC, but no established tumor specific molecular imaging techniques exist.

The aim of this thesis was to investigate the imaging potential of promising biomarkers in HNSCC with emphasis on urokinase-type plasminogen activator receptor (uPAR). In the first paper, we investigated a range of biomarkers in oral squamous cell carcinoma (OSCC) using immunohistochemistry. In the second paper, we investigated the diagnostic value of a novel gallium-68-labeled peptide radiotracer, [^{68}Ga]Ga-NOTA-AE105, targeting the biomarker uPAR in OSCC and oropharyngeal squamous cell carcinoma (OPSCC). In the third paper, we established patient-derived xenograft (PDX) mouse models by implanting tumor tissue from OSCC patients into immunodeficient mice and subsequently investigating the tumor specificity of the Cobber-64-labeled peptide radiotracer [^{64}Cu]Cu-DOTA-AE105.

In Paper I, we demonstrated that the biomarkers integrin αvβ6, tissue factor, and uPAR are highly expressed in both primary tumor tissue and metastases from OSCC, with an

expression pattern that makes them potential targets for molecular imaging. In Papers II and III, we demonstrated the diagnostic properties of [^{68}Ga]Ga-NOTA-AE105 and [^{64}Cu]Cu-DOTA-AE105 in patients and preclinical models, respectively. We present evidence that uPAR-targeted PET-imaging has a high target and tumor-specific tracer uptake and that both tracers show a diagnostic potential for patients with OSCC and OPSCC.

Dansk Resume

Billeddannelse har stor betydning i stadieinddelingen og behandlingen af hoved-halskræft, i særdeleshed mundhule og svælgkræft. Traditionelle billedmodaliteter som CT og MR har flere diagnostiske begrænsninger herunder evnen til at identificere lymfeknude metastaser samt præoperativ afgrænsning af tumorvæv. ^{18}F-FDG PET/CT spiller en vigtig rolle i den postoperative kontrol af patienter med hoved-halskræft, men mangler sensitiviteten for at kunne benyttes til stadieinddeling og kirurgisk planlægning. Interessen for molekylær billeddannelse er tiltagende. Dette skyldes muligheden for at benytte sporstoffer, der er målrettet tumor specifikke biomarkører, som potentielt vil kunne bidrage med mere præcis information på et tidligere tumorstadie sammenlignet med morfologisk billeddannelse. Molekylær billeddannelse giver mulighed for at bidrage til forståelsen af kræftbiologien og forbedre diagnostik og behandling af hoved-hals kræft. Flere biomarkører har været undersøgt for planocellulære karcinomer i hoved-halsområdet, men aktuelt findes der ingen veletablerede tumorspecifikke molekylære billeddannende teknikker.

Formålet med denne afhandling var at undersøge en række lovende biomarkører i hoved-halskræft med fokus på uPAR. I det første studie undersøgte vi potentialet for molekylær billeddannelse af en række biomarkører i orale planocellulære karcinomer ved hjælp af immunhistokemi. I det andet studie undersøgte vi den diagnostiske værdi af et nyt gallium-mærket radioaktivt sporstof, [^{68}Ga]Ga-NOTA-AE105, som er målrettet uPAR, i patienter med orale -og oropharyngeale planocellulære carcinomer. I det tredje studie etablerede vi patient-deriverede xenograft modeller ved at implantere tumor væv i immunsupprimerede mus og efterfølgende undersøge tumorspecificiteten af det radioaktive kobber-mærkede sporstof [^{64}Cu]Cu-DOTA-AE105.

I studie 1 viste vi, at biomarkørerne integrin αvβ6, tissue factor og uPAR er højt udtrykt i både primære tumorer og metastaser fra mundhulekræft, med et ekspressionsmønster

der gør disse biomarkører potentielle mål for molekylær billeddannelse. I studie 2 og 3 demonstrerede vi de diagnostiske egenskaber for sporstofferne, [^{68}Ga]Ga-NOTA-AE105 og [^{64}Cu]Cu-DOTA-AE105 i hhv. patienter og prækliniske modeller. Vi viste, at PET-billeddannelse af hoved-halskræft med sporstoffer målrettet uPAR har en høj specificitet for både uPAR og kræftvæv samt at både [^{68}Ga]Ga-NOTA-AE105 og [^{64}Cu]Cu-DOTA-AE105 har et diagnostisk potentiale for patienter med orale og oropharyngeale planocellulære karcinomer.

Introduction

Imaging plays a key part in the staging of oral and oropharyngeal cancer and is essential for determining the most effective treatment approaches. Traditional imaging techniques, such as CT and MRI, have been instrumental in providing anatomical information. However, these modalities have several limitations, including diagnostic accuracy in the identification of lymph node metastases and delineating primary tumor tissue in pre-treated patients. This has been reflected in a high rate of patients with occult lymph node metastasis (*1–3*) and inadequate margins after surgical resection of primary tumor (*4–6*). As the incidence of head and neck cancer, particularly oropharynx cancer, increases (*7*), the need for improved imaging modalities for visualizing tumor tissue grows. Molecular imaging techniques integrate radiological and biological information, offering unprecedented insights into the complex molecular and cellular processes associated with cancer. By targeting specific molecular markers, molecular imaging allows for the detection and characterization of cancerous lesions at a molecular level, which hold immense potential for improving diagnosis, staging accuracy, and treatment planning in this patient population. Additionally, these techniques facilitate the development of personalized therapies by enabling the selection of appropriate biomarkers for targeted interventions, such as image guided surgical resection and radionuclide therapy.

uPAR is an interesting target for molecular imaging of cancer. It is minimally expressed in normal tissue, but has been found to be significantly upregulated in numerous solid tumors, including HNSCC (*8,9*), where it promotes tumor invasion and metastases (*10*). High uPAR expression has also been associated with poor prognosis (*11–13*). These characteristics render uPAR a desirable imaging and therapeutic target.

The aim of this thesis was to investigate potential imaging targets in HNSCC with focus on positron emission tomography (PET) imaging of uPAR in both preclinical and clinical settings.

Aims and hypothesis

Paper I

The aim was to examine the expression of nine potential/interesting biomarkers by immunohistochemistry in primary tumor and matched metastatic tissue from OSCC to evaluate their potential as targets for molecular imaging.

Our hypothesis was, that among the nine biomarkers examined, we could identify potential imaging targets in OSCC primary tumors and metastases.

Paper II

The aim was to determine the diagnostic value of uPAR-PET/CT to identify locoregional lymph node metastases in patients diagnosed with OSCC and OPSCC using the novel radioligand [^{68}Ga]Ga-NOTA-AE105. Furthermore, we wanted to compare this modality with conventional imaging modalities (MRI/CT).

We hypothesized that [^{68}Ga]Ga-NOTA-AE105-PET/CT could identify regional lymph node metastases and add diagnostic value compared to current imaging modalities (MRI/CT).

Paper III

The aim was first to develop OSCC PDX mouse models and then secondly to explore the use of [^{64}Cu]Cu-DOTA-AE105 for uPAR-targeted PET/CT in these models and evaluate the tumor specificity of the radioligand.

Our hypothesis was that OSCC PDX models resemble human tumor tissue and therefore could be a possible preclinical translational platform for developing new molecular imaging modalities in OSCC. Furthermore, we hypothesized that the tracer uptake in OSCC PDX mouse models corresponded to the uPAR expression determined by immunohistochemistry.

Background

Oral and oropharyngeal squamous cell carcinoma

Head and neck cancer is the seventh most prevalent cancer entity in the world with an incidence of 850,000 new cases per year (*14*). A large proportion of these are located in the oral cavity or the oropharynx, of which squamous cell carcinoma (SCC) accounts for more than 90 % (*15*). The incidence of both OSCC and OPSCC has been increasing globally, with the largest increase in human papillomavirus (HPV)-related OPSCC cases in Western countries, including Denmark (*16–19*). Head and neck squamous cell carcinoma is characterized by local invasive tumor growth and a high tendency of metastasis to regional cervical lymph nodes (*20*). Distant metastases are rare at the time of diagnosis (<5%) and are generally considered a late event in tumor progression. The lung, bone, liver, and brain are the most prevalent organs affected by distant metastases (*21*).

Detecting regional metastases is crucial in the diagnostic procedure and staging of OSCC and OPSCC. Cervical lymph node metastases have been found to be one of the most important prognostic factors (*1,22,23*) and the knowledge of its presence and location of lymph nodes with metastatic tumor deposits is essential in treatment planning. However, the detection of regional metastases is a challenge in OSCC and OPSCC, where between 20-30 % of patients with early-stage disease have occult metastases at the time of diagnosis (*2,3,24*). These metastases are not detected by clinical examinations nor routine imaging like ultrasound, computed tomography (CT) of magnetic resonance imaging (MRI). [^{18}F]FDG-PET/CT has an established role in surveillance of treatment response after chemoradiotherapy (*25*), for detection of distant metastases (*26–28*) and in diagnostic process of detecting unknown primaries in patients with metastatic SCC in cervical lymph nodes (*29*). For detection of nodal disease in HNSCC patients with clinically negative neck (N0), [^{18}F]FDG-PET/CT has shown varying results and moderate diagnostic performance (*30,31*). Preoperative

[^{18}F]FDG-PET/CT can provide additional information for surgical planning, primarily in patients with more advanced tumors (*32*), but has a challenge with false positive findings due to the non-tumor specific [^{18}F]FDG uptake seen in benign lesions, inflammation and infection (*33,34*). Consequently, [^{18}F]FDG-PET/CT are not recommended for pretreatment evaluation of early-stage disease (*30*).

The management of HNSCC in Denmark is described in the Danish Head and Neck Cancer Group (DAHANCA) guidelines (*35*), which are based on new international evidence-based research and involve a multidisciplinary approach. Surgery is the preferred modality in OSCC primary tumors, if tumor extent is locoregional and reconstruction can be accomplished with acceptable aesthetic and functional results. For OPSCC, transoral robotic surgery has gained increasing attention in recent years and has, in several countries, replaced radiotherapy as the most common treatment for OPSCC (*36*). At our institution we have shown that this modality is a good alternative to traditional radiotherapy (*37*) and currently quality of life after transoral robotic surgery for OPSCC patients is investigated in a national multicenter study (QoLATI/DAHANCA 34) (*38*). The primary objective for curative surgery in OSCC and OPSCC is to achieve a clear margin of 5 mm and 2 mm, respectively, of non-cancerous tissue around the tumor to minimize the risks of local recurrence (*39,40*). This is difficult because tumors are frequently surrounded by multiple critical anatomical structures, and the line between tumor and healthy tissue is not clearly defined. Therefore, OSCC and OPSCC are among the solid tumors with the highest positive surgical margin rate (12-30%) (*4–6*). Frozen section microscopy is used for intraoperative margin assessment to reduce the risk of positive margins. Though effective, this approach is time-consuming and might lead to inaccurate results due to sampling and interpretation issues (*41*). Unfortunately, there are currently no well-established intraoperative imaging tools for differentiating normal from malignant tissue in OSCC.

The degree of surgical therapy of the neck lymph nodes is determined by the clinical stage of the neck; thus, correct staging is crucial to the treatment plan. In short, patients without clinically or radiologically signs of lymph node metastases are

candidates for sentinel node biopsy or elective neck dissection (*24,42,43*). This is to ensure that no lymph node metastases are missed in the diagnostic process. Sentinel node biopsy is a diagnostic invasive procedure with identification and excision of the sentinel node/nodes which are the first to receive lymphatic drainage from the primary tumor and, hence are the most likely location for metastases. A neck dissection is subsequently performed if the sentinel node biopsy reveals metastatic disease. Radiotherapy and/or chemotherapy are used as postoperative treatments for advanced disease or as primary treatment for patients with unresectable disease due to either comorbidity or tumor extension.

Despite advances in treatment modalities, the prognosis for patients with OSCC and OPSCC, particularly those with HPV-negative tumors, remains poor. (*44,45*).

A non-invasive tumor specific imaging modality for detecting tumor tissue, both the primary tumor and lymph node metastasis in patients with head and neck cancer, could potentially help reverse this development.

Molecular imaging in head and neck cancer

Molecular imaging is defined as the characterization, visualization, and measurement of biological processes at the molecular and cellular levels in living systems (*46*). With molecular imaging, the expression and activity of specific targets, e.g., cell surface receptors and biological processes such as angiogenesis, can be visualized non-invasively in real-time. This is in contrast to conventional imaging modalities like CT or MRI, which only provide anatomical information (*47*). Various modalities are used in molecular imaging including, single photon emission tomography (SPECT), PET, and fluorescence imaging, all with different properties regarding spatial resolution, depth, cost, and type of read-outs (quantitative vs qualitative data) (*48*)

By combining PET with MRI or CT as a hybrid technique, it is possible to acquire both anatomical and molecular data simultaneously.

Although endogenous molecules can be used for molecular imaging, the majority of cancer imaging approaches require exogenous probes to provide contrast to non-

tumorous tissue. Most probes have been designed with a targeting component, such as a peptide, antibody or small molecule, and a signaling component such as a radionuclide (PET/SPECT) or a fluorophore (optical imaging) (*49*)

The most frequently used molecular imaging modality for HNSCC is [^{18}F]FDG-PET. This modality involves the injection of a radiolabeled glucose analog which is accumulated in tissue with high glucose metabolism e.g. cancer tissue. [^{18}F]FDG-PET is important in the management of HNSCC, specifically in the assessment of therapy response. However, [^{18}F]FDG-PET does not possess the necessary sensitivity to substitute sentinel node biopsy or elective neck dissection for the purposes of staging and surgical planning (*33*). Several other PET-tracers have been investigated in HNSCC. Radiotracers targeting tumor proliferation, like [^{18}F]Fluorothymidine ([^{18}F]FLT) and hypoxia, like ^{18}F-fluoromisonidazole ([^{18}F]FMISO), have been studied in HNSCC and have shown to provide additional information, such as areas of tumor hypoxia, which could be useful for treatment planning. However these modalities have not been able to replace the role of ^{18}F-FDG-PET (*50*).

Recently, fibroblast activation protein inhibitor (FAPI), a new PET target, has received increased attention. Studies have shown promising results in HNSCC patients and the radiotracer ^{68}Ga-FAPI-04-PET/CT was found to outperform ^{18}F-FDG PET in preoperative neck staging in HNSCC patients (*51,52*).

Despite extensive research in the field of molecular imaging of head and neck cancer, there are currently no cancer-specific imaging agents routinely used for staging head and neck cancer.

PET-imaging is the primary focus of the studies included in this thesis, although other imaging modalities are briefly mentioned in Paper I as part of the discussion regarding the search for molecular imaging targets. The principles of PET/CT, which were applied clinically in Paper II and preclinically in Paper III, will be discussed below.

Basic principles of PET/CT

PET is a functional imaging technique that uses intravenously injected radiotracers to measure biochemical processes in the body. Radiotracers are composed of a positron-emitting isotope like ^{18}F, ^{68}Ga, or [64]Cu (the two latter used in Paper II and III, respectively) conjugated with a molecule that is designed to target a particular target or process. The radioactive isotopes (radionuclide) decay by positron emission. The positron travels a few millimeters in the body, known as positron range, depending on the specific radionuclide and the tissue in the body. The subsequent collision with an electron is known as annihilation. In this process two high energy photons (gamma ray) are formed and emitted in opposite direction at 180°±0.5°. The emitted photons are registered by a ring-shaped PET detector that surrounds the patient/animal being examined. By registering the arrival of annihilated photons and by assuming that they are oppositely directed on a straight line (line of response), two photons registered with in a narrow time frame (typically 3-15 nanoseconds) can be registered as an event, and the location of the annihilation can be determined. Because of the many annihilation reactions occurring within a short time frame, there is a risk of two different annihilation events being incorrectly registered as a pair (random events). In PET detectors with higher time resolution (time of flight), it is possible to localize the point of annihilation more precisely. Other sources of noise, like scatter, the process of a photon being deflected off its initial course because of interaction with tissue, need to be corrected with statistical image reconstruction algorithms. CT is based on measuring the attenuation of external gamma rays that pass through the body. Variable tissue composition and density produce distinct attenuation coefficients that can be used to recreate anatomical pictures (*53–55*). Since 1998, it has been possible to combine the functional information from PET with the anatomical information from CT to an integrated PET/CT, giving a superior image compared to the single modalities (*55*). While PET/CT offers numerous advantages, such as penetration depth, whole-body imaging, and quantitative read-out, there are also some disadvantages. Among these

are radiation exposure, the expense, limited spatial resolution, and the long acquisition time (*56,57*).

Identifying biomarkers for molecular imaging of tumors tissue

Targeted molecular imaging is dependent on a target or biomarker that indicates the presence of the specific disease type that is to be investigated, e.g., cancer. All biomarkers in cancer have a role in tumor development, which can be classified according to the hallmarks of cancer proposed by Hanahan and Weinberg (Figure 1) (*58*). The existence of a universally expressed biomarker across all types of malignancies has not been found and is unlikely to be discovered in the future.

Biomarkers are, in general, membrane proteins or ligands to membrane proteins/receptors expressed on the surface of tumor cells or tumor stromal cells, but can also be localized intracellularly like some of the targets studied in this thesis e.g. Poly (ADP-ribose) Polymerase 1 (PARP-1) or Cathepsin E. The advantages of cell membrane bound biomarkers is that the imaging agent does not need to penetrate the cell membrane barrier (*59*). Other biomarker characteristics which is considered important for imaging is; increased upregulation in tumor tissue compared to normal surrounding cells (tumor to background ratio), expression rate of biomarker in tumor tissue and expression pattern of the biomarker (*60*). The pattern of biomarker expression in the primary tumor is, e.g., crucial for fluorescence guided surgery. If the tumor margin is to be distinguished from the surrounding normal tissue during surgery, the expression at the tumor margin is considerably more important than expression at the center of tumor. On the contrary, this would be of less importance in PET detection of lymph node metastases in HNSCC.
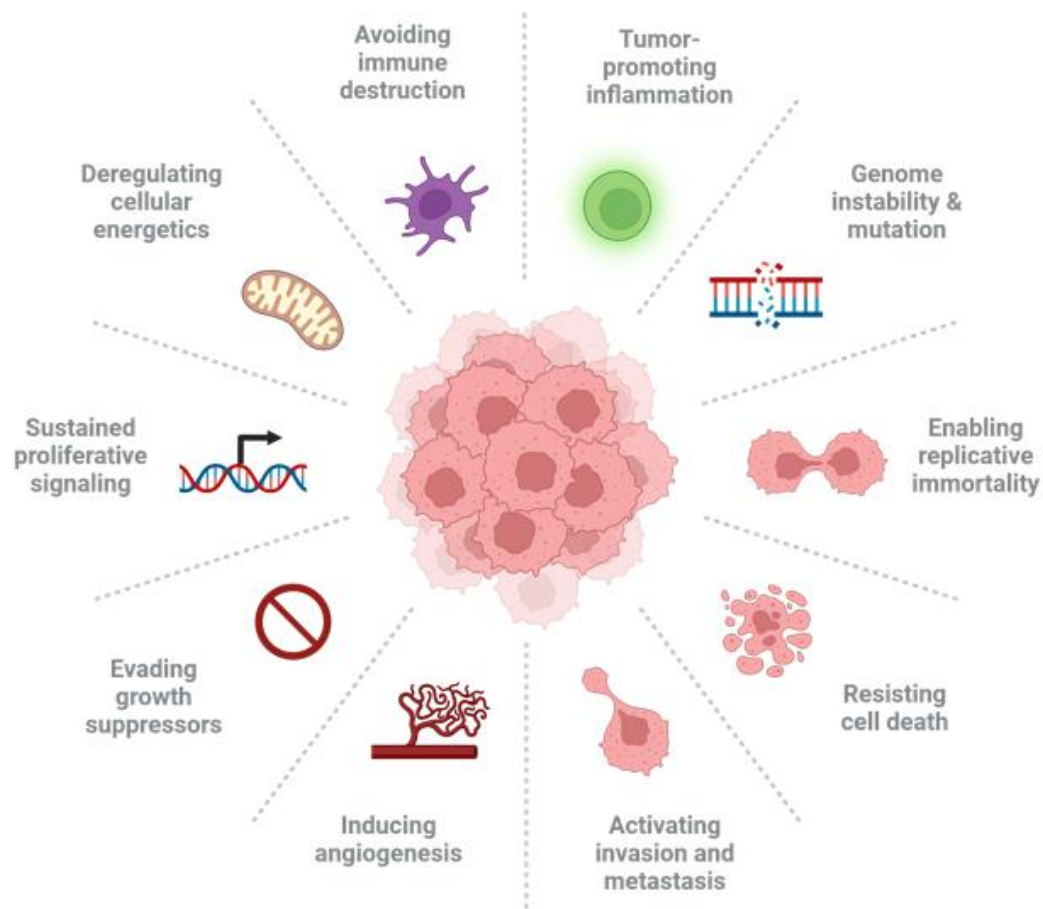
Figure 1. Modified illustration of the hallmarks of cancer as proposed by Hanahan and Weinberg (*58*). The targets investigated in this thesis are essential parts of the different capabilities necessary for tumor growth. Illustration made with Biorender.

In Paper I, the expression of nine biomarkers in tissue from primary tumor, recurrence, and metastases was investigated, and their potential as targets for molecular imaging was evaluated. In the following, these biomarkers will be discussed with a focus on uPAR, which was the primary target investigated in Papers II and III.

Urokinase-type plasminogen activator receptor (uPAR)

uPAR is a glycosylphosphatidylinositol (GPI)-anchored transmembrane receptor comprised of three domains (DI, DII and DII) attached to the cell by a glycolipid-anchor

(*61*). It is a key component of the plasminogen activator receptor system, which is involved in numerous physiological and pathological processes, such as tissue remodeling, inflammation, and cancer. The cellular mechanisms of uPAR are illustrated in Figure 2.

Under normal physiological conditions, uPAR expression is low in cells and tissue. However, during the process of tissue remodeling, wound healing and inflammation, uPAR is significantly increased. This has been shown during placenta development (*62*), in keratinocytes at the edge of wounds (*63*), and in the central nervous system after trauma/ischemia (*64*). In contrast to normal tissue, uPAR is overexpressed in most solid cancers, including breast, prostate, bladder, brain, lung, gastric, colon, oral, and oropharyngeal cancer (*8,65–68*), with exceptionally high expression at the invasive front (*69*). High uPAR-expression in tumors has been associated with metastases and poor prognosis (*70*).

One of the main functions of uPAR is to bind the inactive form of urokinase-type plasminogen activator (pro-uPA) on the cell surface which triggers a series of proteolytic reactions. The binding of pro-uPA to uPAR activates uPA which then converts plasminogen to plasmin, resulting in increased extracellular matrix (ECM) degradation and subsequent tumor invasion and metastasis.
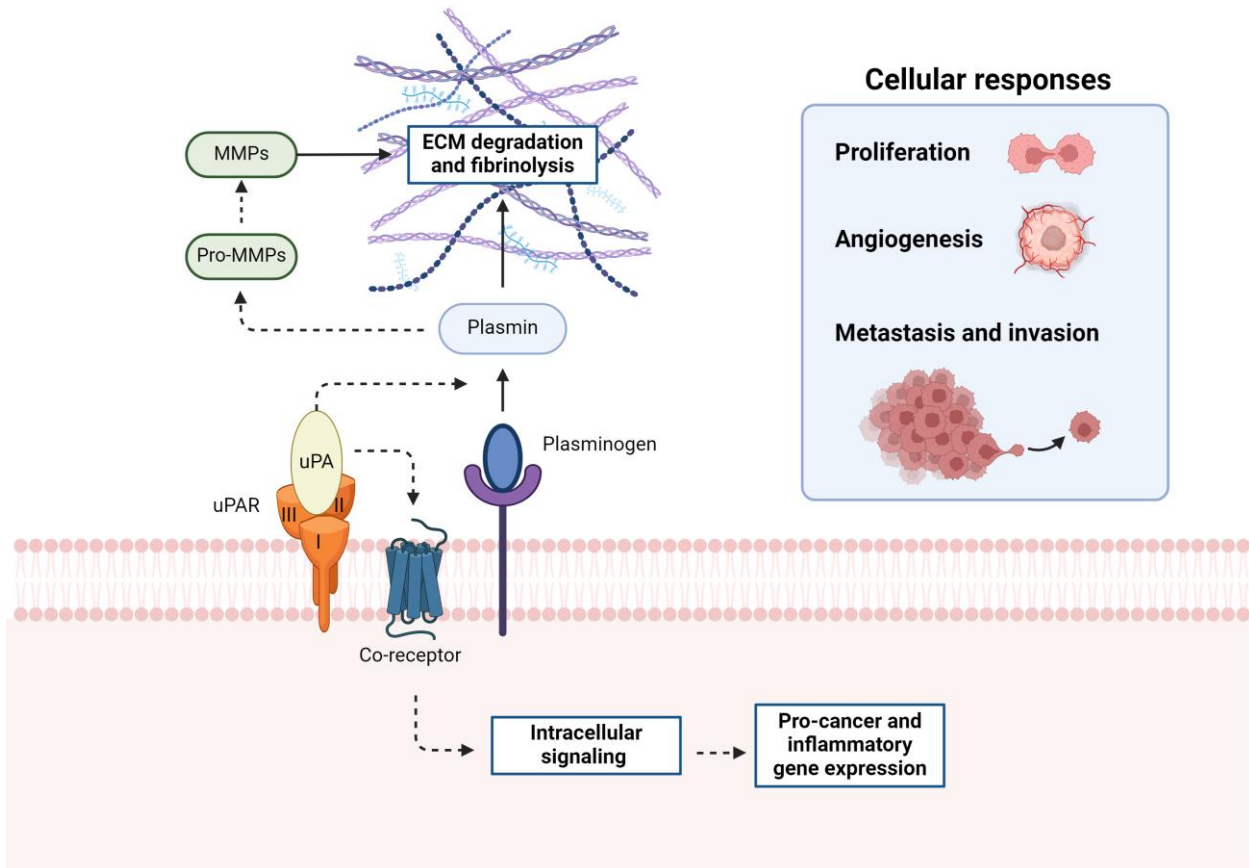
Figure 2. A simplified illustration of the cellular mechanisms of uPAR in cancer cells, which lead to several cancer-promoting responses, including cancer cell proliferation, angiogenesis, metastasis, and invasion. Illustration made with Biorender.

uPAR also has several nonproteolytic roles in cancer. The interaction between uPAR and uPA activates intracellular signaling pathways, including the PI3K/Akt and MAPK pathways, which contribute to tumor cell proliferation, migration, and angiogenesis. Additionally, uPAR can react with different cell surface receptors, such as integrins and growth factor receptors activating other intracellular signaling pathways, including expression of pro-cancer genes (*10*). uPAR's selective overexpression in cancer compared to normal tissue, its involvement in tumor progression and metastases and its association with prognosis makes it an interesting target for molecular imaging and personalized medicine.

Integrin αvβ3 and integrin αvβ6

Integrins are transmembrane cell surface receptors made up of an alpha- and beta-unit and play an important role in cell to cell signaling and cell to ECM interactions (*71*). Both integrin αvβ3 and αvβ6 recognize and bind to the tripeptide Arginyl-Glycyl-Aspartic acid (RGD), which is present on many ECM molecules (*72*).

Integrin αvb3 has been shown to play an essential part in tumor-induced angiogenesis (*73*). HNSCC, which are well-vascularized tumors, require angiogenesis for tumor progression and invasion. Several studies have shown varying amount of upregulation of αvβ3 in tumor cells, endothelial cells and tumor stromal cells of HNSCC (*74,75*).

Molecular imaging of αvβ3-expression using radiolabeled RGD-peptide tracer has been investigated in different cancers where a correlation between immunohistochemical expression of integrin αvβ3 and standard uptake values (SUV) was demonstrated (*76*). A pilot study compared the integrin αvβ3-specific tracer [^{68}Ga]Ga-NODAGA-RGD to ^{18}F-FDG for PET/CT imaging of primary tumors in head and neck cancer. They found that all tumors were visible with both tracers, however, with lower SUV-values for [^{68}Ga]Ga-NODAGA-RGD and different spatial resolution (*77*).

Integrin αvb6 facilitate adhesion between cells and between cells and the ECM and has been found to be involved in different hallmarks of cancer, including progression and invasion (*78–80*). Numerous studies have reported overexpression of integrin αvβ6 in HNSCC, especially at the profound tumor margin, and no or weak expression in normal epithelium (*78,81*). Integrin αvβ6 has been used as a target for molecular imaging in several studies. For PET imaging, a first in human study has investigated a non-RGD integrin αvβ6-binding peptide, radiolabeled with ^{18}F. The study included patients with lung, breast, and pancreatic cancer, in which the tracer demonstrated significant uptake both in primary and metastatic lesions (*82*). In a subsequent study, a ^{68}Ga-labeled peptide was investigated in patients with HNSCC and pancreatic cancer. The findings of

this investigation revealed a notable and specific accumulation of the tracer within tumor tissue, while no uptake was observed in areas associated with tumor-related inflammation (*83*). Integrin αvβ6, as a target for fluorescence imaging in HNSCC, is currently being studied in a clinical trial (NCT04191460) to determine if this modality might increase the rate of adequate surgical resection margins in OSCC.

Tissue factor

Tissue factor is a transmembrane receptor that initiates coagulation by binding to the coagulation serine protease factor VII/VIIa. This results in platelet activation and fibrin deposition. Tissue factor is in normal tissue expressed, especially in fibroblasts of the vessel wall, and is activated in case of injury. In cancer, the expression of tissue factor by tumor cells has been shown to contribute to tumor growth, thrombosis, metastasis, and angiogenesis (*84*). Tissue factor expression levels have been found elevated in several malignancies, including HNSCC (*8,68*). The potential of tissue factor as an imaging target has been investigated in various malignancies, but limited in HNSCC. In preclinical tumor models of anaplastic thyroid cancer, glioblastoma, and pancreatic cancer, tissue factor has been investigated as a target for fluorescence guided surgery, SPECT, and PET with positive results (*85–87*).

Poly (ADP-ribose) polymerase 1 (PARP-1)

PARP-1 is an enzyme mostly present in the cell nucleus and involved in DNA repair and gene transcription. The PARP-1 gene has been shown to be upregulated in many malignancies, including OSCC (*88,89*). Furthermore, PARP inhibitors have been approved as an antineoplastic treatment for several cancer entities (*90*). Molecular imaging of PARP-1 in HNSCC has been investigated for both fluorescent imaging and PET imaging. A first-in-human trial examined the radiotracer [^{18}F]F-PARPi's ability to detect tumor tissue in individuals diagnosed with OSCC and OPSCC. The study revealed that [^{18}F]F-PARPi successfully identified both primary tumors and metastases at a rate that was comparable to [^{18}F]F-FDG (*91*). Another phase I study with early-

stage OSCC patients investigated the topically applied PARP-1 specific fluorescence agent and found a tumor to background ratio >3 (*92*).

Vascular endothelial growth factor receptor 1 and 2 (VEGFR1 and VEGFR2)

VEGFR 1 and VEGFR2 are transmembrane receptors that are expressed by endothelial cells. The binding of vascular endothelial growth factor (VEGF) to these receptors initiates a series of signaling events that play a key part in the process of angiogenesis. Solid tumors are unable to grow sufficiently in the absence of an adequate vascular supply. Thus, VEGFR receptors are essential to the progression of cancer and a promising target for therapeutic interventions and imaging techniques. (*93*). Overexpression of VEGF, VEGR1 and VEGFR2 have been found in varying degrees in tissue from OSCC and laryngeal squamous cell carcinoma (*94*,*95*). Extensive examination of PET imaging for targeting the VEGFR/VEGF-system has been conducted in preclinical investigations, as well as in a limited number of clinical trials, with the majority of recent studies reporting favorable outcomes. However, to the best of our knowledge, VEGFR-targeted PET imaging of HNSCC has not been explored (*96*).

Epithelial Cell Adhesion Molecule (EpCAM)

EpCAM is a transmembrane glycoprotein that is overexpressed in several malignancies, including OSCC (*97*). The role of EpCAM in cancer is not fully understood but it is believed that EpCAM inhibits cathepsins, proteases frequently generated by tumor cells and implicated in metastasis. It has been proposed that the inhibition protects tumor cells from their own cathepsins. EpCAM has been identified as essential for tumor cell proliferation, invasiveness, and migration (*98*). Intratumoral administration of anti-EpCAM therapy for patients with recurrent HNSCC following radiotherapy and/or chemotherapy has been investigated in a phase I trial with positive response to treatment for EpCAM positive patients (*99*). Several studies have investigated the use of fluorescence probes for fluorescence guided surgery in orthotopic tumor models including HNSCC and found that tumor could be clearly delineated (*100*,*101*).

Radionuclide probes targeting EpCAM have also shown tumor specific uptake in preclinical breast cancer xenograft models (*102*).

Cathepsin E:

Cathepsin E is a protease that is found intracellular and expressed in different cells including immune -and cancer cells. The precise function of Cathepsin E is not fully understood (*103*). Elevated Cathepsin E levels have been associated with different cancer entities, especially pancreatic cancer, where preclinical studies have tested Cathepsin E targeting fluorescence probes and demonstrated a threefold higher tumor signal compared to background (*104*,*105*). Cathepsin E expression levels in HNSCC are poorly investigated.

PDX-models

Animal models play an essential role in cancer research, serving as valuable tools for understanding disease mechanisms, investigating new targets and developing novel drugs/imaging agents. Among the various types of animal models, patient-derived xenograft (PDX)-models have emerged as a valuable tool in cancer research.
PDX models are preclinical cancer models, where tumor tissue from patients is directly implanted either subcutaneously or into the anatomically correct location (orthotopic) within the immunodeficient animal. The PDX models rely primarily on immunodeficient mice, which are deficient in either B cells, T cells, natural killer (NK) cells, or all three. Nude mice (used in Paper III), also known as athymic nude mice, are commonly used for in vivo studies of human tumors. The nude mouse is a strain with a spontaneous mutation in the genome (FOXN1-gene) that causes absence of thymus function which results in impaired T-cell development. This immune defect makes it possible to implant tissue from other species (xenograft) without a rejection response (*106*). The absence of an intact immune system prevents human tumor cells and the host's immune system

from interacting. This may influence the behavior of the tumor, including its potential for metastasis, which does not accurately reflect the clinical scenario.

In PDX models, the fresh surgical tumor tissue from a patient undergoing surgical resection, is cut into small pieces (3-5 mm^3) before implantation. The generation-bearing patient-derived material is designated as P0, and the following generations are numbered consecutively (P1, P2, etc.). Usually, tumor "take", i.e the development of a steadily growing tumor, occurs within the first couple of months, but it can take up to six months (*107*). Contrary to other animal cancer models, like cell line-derived xenograft models and transgenic tumor models, PDX models retain heterogeneity and mutations from patients tumor as well as the tumor microenvironment (*108*). The latter is especially important when studying targets like uPAR, which is not only expressed in the tumor cells, but also by macrophages and fibroblasts in the tumor-stromal compartment (*61,66*). Due to the retained tumor microenvironment, which plays a crucial role in both local and distant tumor dissemination, PDX models are considered valuable for investigating the biology of metastasis. The advantages of PDX models over conventional cancer models also make it a promising tool for the development of novel treatment and molecular imaging strategies, as well as for improving the field of precision oncology.

Methods

Study design

Paper I was an immunohistochemical study investigating tumor tissue from OSCC patients surgically treated at Rigshospitalet between 2000 – 2011. The method is outlined in figure 3. Patients were selected from the Copenhagen Oral Squamous Cell Carcinoma Database (*109*). Only cases which had formalin-fixated paraffin-embedded (FFPE) tumor samples with surrounding normal tissue were chosen for analysis. Tissue from the primary tumor, lymph node metastases and recurrence was retrieved. Clinicopathological data was collected retrospectively. Nine interesting biomarkers were chosen, all with reported overexpression in cancer and with a potential for fast translation into clinical settings due to prior probe development. The immunohistochemical expression of all biomarkers was determined on all retrieved tumor tissue. Two specialized head and neck pathologists scored all samples for intensity in tumor compartment, expression pattern in tumor tissue (heterogeneous vs. homogeneous), proportion of stained tumor tissue in tumor compartment and intensity in normal epithelium. A total immunostaining score was calculated, and a statistical comparison was made between the various targets and malignant tissue types.
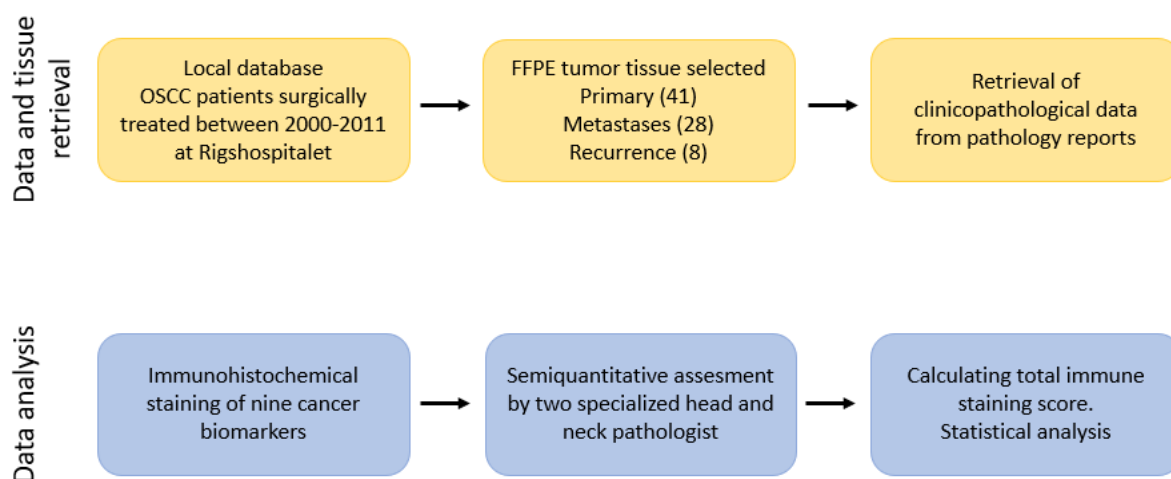
Figure 3. Overview of the process of data and tissue retrieval (yellow boxes) and analysis (blue boxes) in paper I.

Paper II was a prospective phase II trial including patients between 18-85 years with biopsy verified OSCC and OPSCC, with or without regional metastases, referred to primary surgical treatment at the Department of Otorhinolaryngology, Head and Neck Surgery and Audiology, Rigshospitalet. Exclusion criteria were pregnancy and weight above 140 kg. Additionally, patients with prior neck surgery or radiotherapy to the neck were excluded, as this may alter the local lymph node drainage. There was no control group in this study. Prior to surgery, the [^{68}Ga]Ga-NOTA-AE105 PET/CT scan was performed in conjunction with the conventional diagnostic imaging work-up (CT/MRI). A radiology team, consisting of an experienced nuclear physician and a specialized radiologist, blinded to clinical data and prior imaging work up, evaluated the uPAR-PET/CT scans. Lymph nodes were classified as positive if higher uptake was found visually compared with surrounding tissue. These results were compared to the pathology results (considered the gold standard) from the neck surgery, i.e., sentinel node biopsy and/or selective neck dissection. The diagnostic performance of [^{68}Ga]Ga-NOTA-AE105 PET/CT in detecting regional lymph node disease was calculated as the

31

presence or absence of metastatic disease and not per-lesion. The sensitivity and specificity for [68Ga]Ga-NOTA-AE105 PET/CT and standard diagnostic workup (CT/MRI) were compared. However, the diagnostic performance for the different modalities was not completely comparable. The [68Ga]Ga-NOTA-AE105 PET/CT was evaluated blinded to prior clinical and paraclinical data, whereas the routine CT/MRI was evaluated according to the department's routine standard, i.e., with all available clinical and paraclinical data.

Furthermore, tissue from primary tumors were immunohistochemical stained for uPAR. The product of the histochemical score (H-score) and tumor depth was compared to the SUV_{max} value.

Paper III was a preclinical in vivo study with the establishment of PDX-models with implantation of tumor tissue from OSCC patients into NMRI mice. Patients with OSCC undergoing primary surgery at the Department of Otorhinolaryngology, Head and Neck Surgery and Audiology, Rigshospitalet, were included and contacted regarding the donation of a biopsy. Tumor tissue from patients was implanted in the flank of NMRI mice (passage 0), and followed until exponential growth (Figure 4). Subsequently, the mice were euthanized, and tumor tissue was implanted in 5 mice (Passage 1) for further expansion. When tumor in passage 1 mice reached a volume of more than 1000 mm^3, tumor was passaged to 10-16 mice (passage 2). To evaluate histological stability through passages, HE-stained tumor samples were evaluated by a specialized head and neck pathologist. [64Cu]Cu-DOTA-AE105 PET/CT was performed on passage 2 mice. Subsequently the mice were euthanized. Autoradiography and immunohistochemistry were performed on tumor tissue from the [64Cu]Cu-DOTA-AE105 PET/CT scanned mice, to validate the distribution of the radiotracer in the tumor tissue. Normal muscle tissue was also used for autoradiography as a negative control.
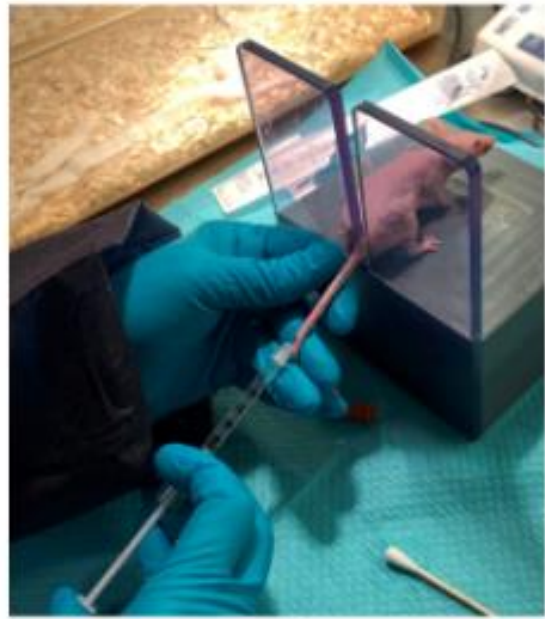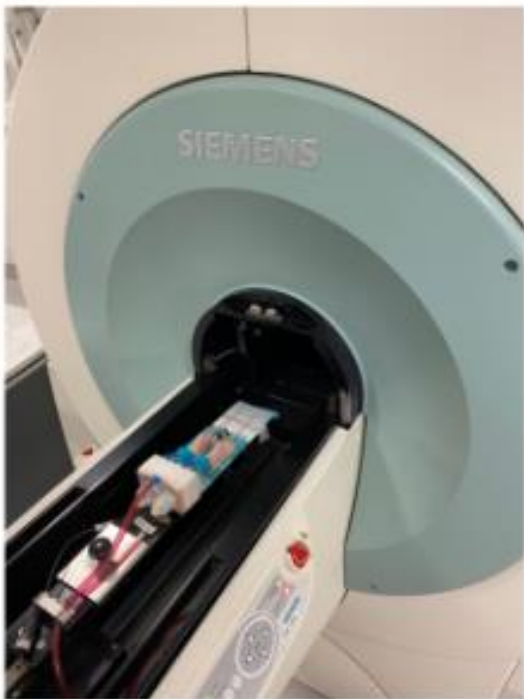
Figure 4. A. OSCC PDX models in NMRI mice with subcutaneous flank tumors. B. Injection of ^{64}Cu-DOTA-AE105 in tail vein 60 minutes before PET/CT. C. PET/CT of two anesthetized NMRI mice in a

dedicated animal scanner. D. Resection of a subcutaneous flank tumor from a euthanized NMRI mouse after [64Cu]Cu-DOTA-AE105 PET/CT. The resected tumor was subsequently divided for histology/immunohistochemistry and autoradiography analysis. Unpublished own data.

Immunohistochemistry

In all three Papers immunohistochemical analysis were performed. In Paper I, the analyses were performed partly using a semi-automated autostainer (Ventana Benchmark Ultra, Roche Diagnostics) in the Department of Pathology, Rigshospitalet and partly manually in the IHC laboratory at Cluster for Molecular Imaging, Copenhagen University Hospital. In Paper II and III, immunohistochemical analysis were only performed manually in the IHC laboratory at Cluster for Molecular Imaging, Panum, Copenhagen University Hospital.

Assessment of biomarker expression in tumor tissue

In Paper I, two specialized head and neck pathologists manually evaluated the expression of each biomarker by semiquantitative scoring intensity (0-3) and proportion (0-4) of tissue in tumor compartment and non-cancerous epithelium. The intensity and proportion score were multiplied to provide a total biomarker expression score ranging from 0-12, as previously described in other studies (*110*,*111*).

In Paper II and Paper III the biomarker expression was quantified digitally using the open software Qupath version 0.3.2 (*112*) which uses the H-score. The H-score is calculated with the formula: (0 x percent negative cells) + (1 x weakly positive cells) + (2 x percent moderately positive cells) + (3 x percent strongly positive cells), which gives a score ranging from 0-300. A specialized pathologist supervised the digital delineation of tumor compartment and the settings for identifying cells.

Radiotracer synthesis and PET acquisition

Two different radiotracers were used. In Paper II, [68Ga]Ga-NOTA-AE105 was administered to patients and in Paper III, [64Cu]Cu-DOTA-AE105 were administered to

mice. In summary, a cyclotron was used to produce ^{64}Cu (Hevesy Laboratory, DTU, Nutech Risø) whereas ^{68}Ga was produced in house on a ^{68}Ga-generator as previously described (*113*). NOTA-AE105 and DOTA-AE105 was then radiolabeled with ^{68}Ga and ^{64}Cu, respectively, in a buffered solution by an in-house chemist at the Department of Clinical Physiology and Nuclear Medicine, Rigshospitalet.

In Paper II, whole body PET/CT scans, skull base to proximal thigh were performed 20 minutes after intravenous injection of approximately 200 MBq of [^{68}Ga]Ga-NOTA-AE105. Patients were scanned on an integrated whole-body PET/CT system (Siemens Biograph mCT 64 slice, Siemens, Germany).

In Paper III PET/CT scans were performed one hour and again 24 hours after injection of [^{64}Cu]Cu-DOTA-AE105 in the lateral tail vein. Mice were scanned on a small animal PET/CT scanner (Inveon, Siemens Medical Systems, PA, USA).

PET/CT analysis

In Paper II, the images were analyzed by a team consisting of an experienced nuclear physician and an experienced radiologist, blinded to clinical data. The team contoured the regions of interest and the [^{68}Ga]Ga-NOTA-AE105 uptake in this region was measured as SUVmax.

In Paper III, images were analyzed using the Inveon software (Siemens Medical Systems, PA, USA) on the fused PET/CT images. On CT scans, regions of interest (ROIs) were delineated and then projected to the fused PET image. ROIs were created on every fourth tumor slide in the axial plane, and tumor sizes were calculated based on all ROIs. SUV_{max} and SUV_{mean} were calculated for each tumor.

Ethical consideration

In Paper II:

The study was approved by the Danish Medicines Agency and the Danish Research Ethics Committee and monitored by the Good Clinical Practice Unit of Capital Region, Denmark. No side effects have been reported in the phase I trial using ^{68}Ga-NOTA-

AE105 (*113*). The radiation dose from ^{68}Ga-NOTA-AE105 at 200 MBq is 3 mSv (*113*). A diagnostic full body CT scan exposes the patient for approximately 12 mSv. The total effective radiation burden is therefore approximately 15 mSv. Theoretically, this increases the probability of acquiring a fatal cancer from 25.0% to 25.12%. For individuals with diagnosed cancer, the additional radiation dose is considered appropriate in relation to the potential benefit of developing a new diagnostic imaging modality.

In Paper III: animal ethical considerations
The study was approved by the Danish Research Ethics Committee (H-17025452) and the Danish Animal Experiment Inspectorate (license no. 2021-15-0201-01041). Tumor tissue for implantation in mice was retrieved from the resected primary tumor specimen by a head and neck pathologists making sure no surgical margins were compromised. Animals were treated according to the guidelines for standardized procedures in animal experiments and tumor models including all humane endpoints (e.g., tumor size, skin ulceration, weight loss).

Summary of results

Paper I

In total, tumor tissue from 41 patients surgically treated for OSCC at Rigshospitalet between 2000-2011 were included. Tumor tissue was initially available for 41 primary tumors, 28 matched metastases and 8 matched local recurrence. The expression of nine targets were evaluated by immunohistochemistry in all available tumor specimens. In short, three targets, uPAR, Integrin αvβ6 and tissue factor, showed both a tumor specific expression pattern in OSCC and high overall total immune staining scores. Four targets, PARP-1, VEGFR1, EpCAM and VEGFR2, showed varying degrees of expression in tumor tissue. However, the expression was either not tumor specific (PARP-1, VEGFR1) or had a low total immune staining score (VEGFR2 and EpCAM). Two biomarkers, integrin αvβ3 and cathepsin E, were largely unexpressed in tumor tissue. In the following, the results from the three most promising targets in OSCC tissue, uPAR, integrin αvβ6 and tissue factor are summarized (Table 1). The expression rate was high for both uPAR, integrin αvβ6 and tissue factor with an expression rate in all tumor specimens of 97%, 97% and 86%, respectively. Tissue factor and uPAR expression were largely tumor-specific, exhibiting low levels of expression in non-cancerous cells surrounding the tumor compartment and normal epithelium. This resulted in a clear contrast between tumor compartment and the surrounding non-cancerous tissue for both primary tumors, lymph node metastases and local recurrence. For integrin αvβ6, a high expression was seen in tumor compartment but also in normal epithelium, but little expression was seen in non-epithelial normal cells surrounding tumor. Consequently, a difference in integrin αvβ6 expression between normal cells and tumor tissue was negligible at the superficial margin but clearly visible at the profound margin. An apparent contrast in integrin αvβ6 expression was also seen in lymph node metastatic tissue compared to the surrounding normal cells.

Biomarker	Expression rate	Median Intensity score (IQR)	Median proportion score (IQR)	Median total immune staining score (IQR)	Homogenous expression in tumor compartment	Contrast superficial margin Tumor vs normal epithelium	Contrast deep margin Tumor vs normal cells
uPAR	97%	3(2.75-3)	2(2-3)	6(6-9)	80%	yes	yes
Integrin αvβ6	95%	3 (3-3)	4(4-4)	12(12-12)	51%	no	yes
Tissue Factor	93%	3(2-3)	2(1-3)	6(2.5-7.5)	3%	yes	yes

Table 1. immunohistochemical expression pattern in primary OSCC tumors of the three most promising biomarkers investigated in Paper I.

Paper II:

In total, 66 patients with OSCC or OPSCC were included of which 61 patients had a [^{68}Ga]Ga-NOTA-AE105 PET/CT performed. No adverse events were reported. Most patients (79%) were diagnosed with OSCC, while 21% were identified with OPSCC. According to the 8th edition of the UICC guidelines, 60% of tumors were early-stage (I-II) with a high proportion of small primary tumors (79% T1-T2).

All the scanned patients underwent curative intended surgery with removal of the primary tumor. Two patients chose watchful waiting instead of surgical neck intervention, leaving 59 patients with histologically defined neck status. Twenty-five patients had histological verified lymph node metastases and in 14 of these patients [^{68}Ga]Ga-NOTA-AE105 PET/CT found regional metastatic disease (example shown in figure 4). Standard imaging work-up (CT/MRI) also identified 14 patients, but discordance was seen in four patients.

The median size of the regional metastatic lesions detected by [^{68}Ga]Ga-NOTA-AE105 PET was 14 mm (range 3-27mm), which was significantly larger than those not detected (p=0.006). Diagnostically, MRI/CT and [^{68}Ga]Ga-NOTA-AE105 PET/CT were equally effective; each modality had a 56% sensitivity, a 100% specificity, a 100% positive predictive value, and a 76% negative predictive value. However, when [^{68}Ga]Ga-NOTA-AE105 was combined with routine imaging, the sensitivity increased to 64% and additionally 18 % (2/11) of the patients with subclinical nodal disease was identified.
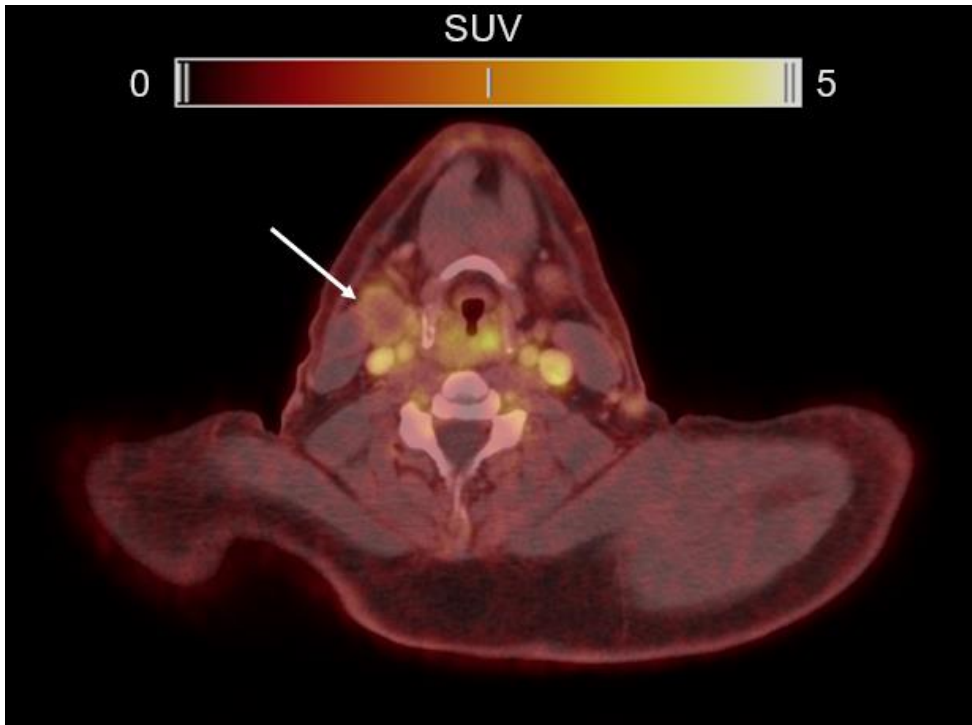
Figure 4. Axial plane of ^{68}Ga-uPAR-PET/CT showing a PET-positive lymph node metastasis with central necrosis.

The uPAR expression was determined by immunohistochemistry on FFPE samples from resected primary tumors and metastases (Figure 5). To determine the target specificity of the [^{68}Ga]Ga-NOTA-AE105 PET tracer, we calculated the correlation between uPAR expression in primary tumors (H-score) and matched PET-signal (SUVmax) and found a significant positive correlation in (r=067; p=0.003). Due to lack of tissue available from resected lymph node metastasis it was not possible to make a meaningful correlation analysis between uPAR-expression and PET-signal in metastases.
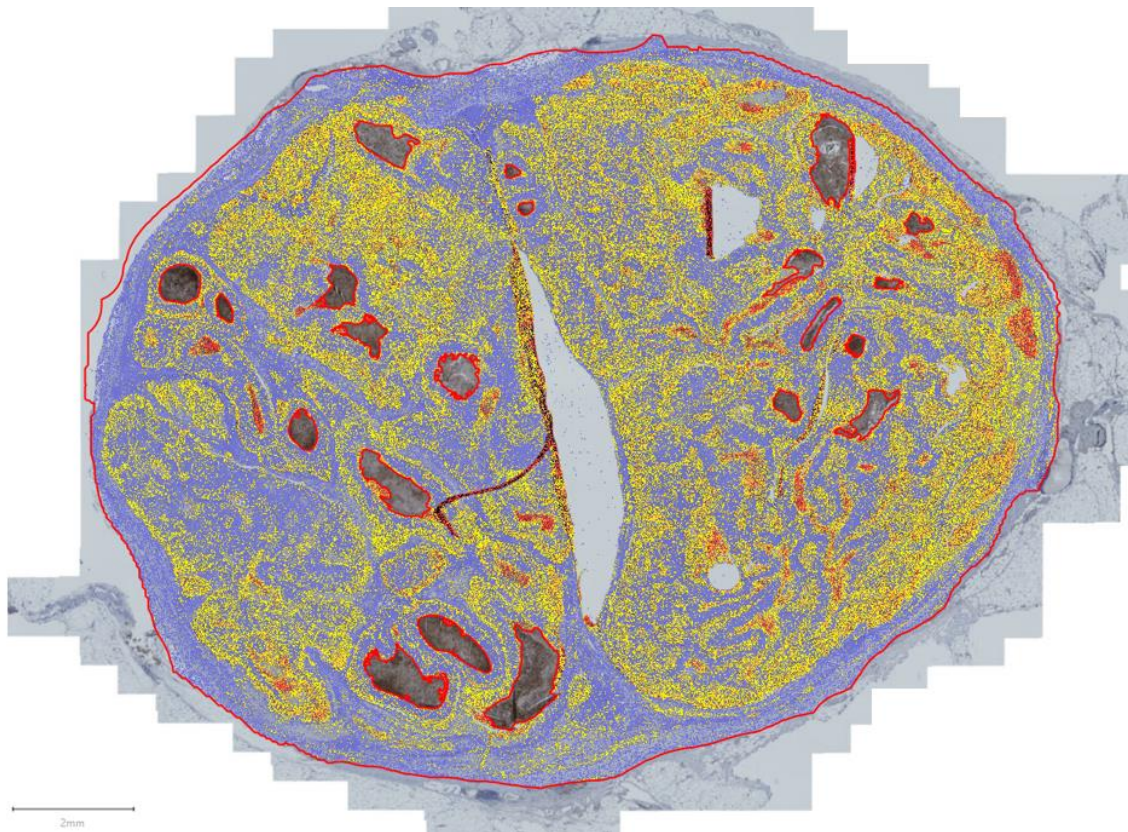
FIGURE 5. uPAR expression determined with immunohistochemistry in a cross-section of excised lymph node metastasis from OSCC. The expression is quantified digitally using the Qupath software. Staining intensities of negative (0), weak (1+), moderate (2+), and severe (3+) correspond to the following colors: blue, yellow, orange, and red, respectively. The red annotated areas represent necrosis and have been excluded from H-score calculations.

Paper III:

In the first part of Paper III, PDX models were established.

Tumor tissue from three patients with advanced OSCC was used. All patients had HPV-negative, stage III-IV disease with moderate to poor differentiation. Across all models, the rate of tumor growth accelerated from initial implantation (P0) to subsequent passages. The mean time between implantation and PET/CT for Passage two models was 67 days, with a range of 29 to 106 days.

A specialized head and neck pathologist examined the histopathological characteristics in tumor tissue. From the donor tumor to passage 2 tumor tissue, there were no significant changes observed in pleomorphism, the extent of degenerative alterations (such as cystic formation, focal necrosis, and keratinization), or the configuration of the invasive front. Additionally, across the various PDX models (P0-P2), the uPAR in tumor cells remained unaltered compared to donor tumors. Around necrosis/cysts and in the invasive front of all models, uPAR expression was highest.

In the second part of Paper III, we investigated [^{64}Cu]Cu-DOTA-AE105 PET/CT in 29 mice from three of the above mentioned OSCC PDX models (Figure 6). The mean (± SD) SUV$_{max}$ was 1.50 (±0.24), 1.96(±0.33) and 1.97 (±0.41) for models 1, 2 and 3, respectively. Heterogenic uptake was observed in most tumors. Tracer uptake varied between the models, with lower uptake in model 1 and areas with higher uptake in model 3. Several tumors exhibited peripheral enhancement. Autoradiography of the tumor revealed that the distribution pattern of the tracer ^{64}Cu-DOTA-AE105 visually correlated with the uPAR expression found by immunohistochemical staining from the same tumor. Autoradiography of the quadriceps muscle tissue showed minimal tracer uptake, which confirmed the low background tracer uptake. uPAR expression was seen in all models with varying H-score. We were not able to show a significant positive correlation between uPAR expression (H-score) and tracer uptake in tumor after 1 hour (SUVmax).
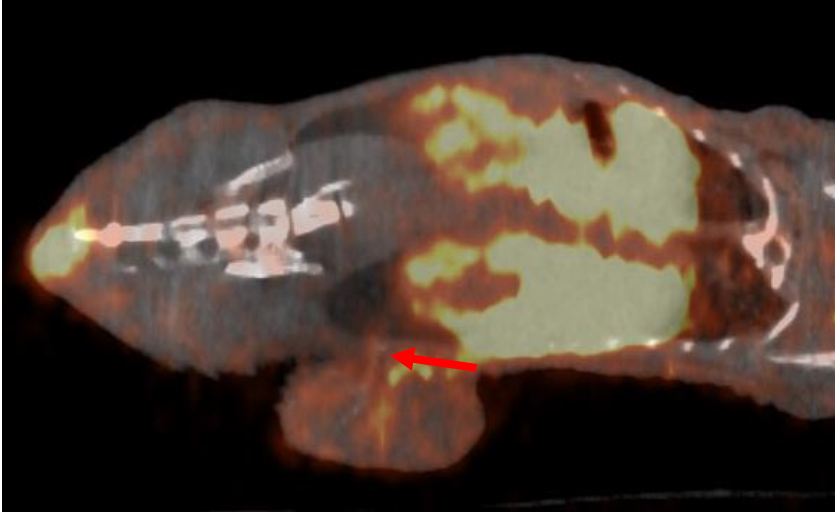
Figure 6. ^{64}Cu-uPAR-PET/CT of NMRI-mouse with OSCC tumor tissue implanted in the flank (PDX model). Red arrow shows the flank tumor.

An interesting correlation (r=-0.40, p=0.03) was observed between uPAR expression (H-score) and tumor growth (days from implantation to 400 mm^3 in volume). The expression of Ki67 did not exhibit a statistically significant correlation with tumor growth. This finding suggests that higher uPAR expression is associated with increased tumor growth.

Discussion

Potential targets for molecular imaging of HNSCC

In Paper I, we evaluated the immunohistochemical expression of nine biomarkers in tissue from OSCC primary tumor and their corresponding lymph node metastases and local recurrence to assess their potential as molecular imaging targets. Based on the expression level and expression pattern in tumor tissue and surrounding non-cancerous tissue, we found that uPAR, integrin αvβ6, and tissue factor were potential imaging targets. uPAR was found expressed in various degree in almost all lymph node metastases and primary tumors. In primary tumor tissue, uPAR expression was found to be intermediate overall, whereas expression in normal epithelium was almost absent. In the normal stromal tissue surrounding tumor, only few cells expressed uPAR. These expression characteristics are desirable in various molecular imaging modalities, e.g., fluorescence-guided surgery where a clear visual demarcation of tumor tissue is necessary. Almost all lymph node metastases (96%) expressed uPAR, most with low to intermediate expression. Since uPAR is expressed at both locations, it seems theoretically feasible to apply combined uPAR-targeted molecular imaging strategies which target both the primary tumor and metastases. The immunohistochemical results for uPAR is comparable to prior studies in OSCC, however none of these examined primary tumors were with matched tissue from lymph node metastases and tumor recurrence (*8,68*).

Similar to uPAR, tissue factor exhibited tumor specific expression; however, it did so at a reduced rate (86%) and with a non-homogenous pattern. In lymph node metastases, tissue factor expression was lower compared to the expression in primary tumor tissue. These results are consistent with prior studies examining primary tumor tissue from OSCC and OPSCC (*8,68*).

Despite limited research of tissue factor as a target for molecular imaging in head and neck, its potential has been explored in various other malignancies. With promising

results, tissue factor specific monoclonal antibodies have been utilized in preclinical studies to examine this biomarker as a target for fluorescence-guided surgery, SPECT, and PET in xenografts of anaplastic thyroid cancer, glioblastoma, and pancreatic cancer (*85–87,114*). Recently a new antibody-drug conjugate (tisotumab vedotin) targeting tissue factor was approved for use in patients with metastatic cervical cancer (*115*). A tissue factor targeted PET tracer has subsequently been studied and proposed as a diagnostic tool prior to select patients for this therapy. This illustrates that tissue factor as an imaging target has the potential to be extended to other types of cancer, such as HNSCC, where it appears to be expressed to a greater extent.

Integrin αvβ6 was highly expressed in tumor tissue from both primary tumor, lymph node metastases, and recurrence. In primary tumors a clear contrast between tumor and normal tissue at the deep margin was seen. But a high expression of integrin αvβ6 was also found in normal epithelium, and no significant intensity difference was found between tumor and normal squamous cell epithelium. These results indicate that molecular imaging targeting integrin αvβ6 in OSCC could potentially yield a noticeable contrast effect in the deeper regions and in lymph node metastases, where normal squamous cell epithelium is not present. At the superficial border, nevertheless, the differentiation between normal tissue and tumor tissue is anticipated to be challenging. Recent research has investigated the potential of integrin αvβ6 as an imaging target in HNSCC. PET imaging targeting integrin αvβ6 in cancer was initially investigated in humans in 2019 (*82*). Subsequently, a study has shown tumor-specific uptake in HNSCC and pancreatic cancer with a gallium-labeled peptide tracer (*83*). Currently, integrin αvβ6-targeted fluorescence guided surgery is being examined as a tool for achieving tumor-free resection margins in prospective phase II trials in OSCC (NCT04191460) as well as in laryngeal and hypopharyngeal cancer (NCT05752149).

The remaining six biomarkers (integrin αvβ3, PARP-1, ePCAM, VEGFR1, VEGFR2 and cathepsin E) examined in Paper I, did either not show tumor-specific expression

patterns or had low expression levels and were from this perspective deemed less suitable as imaging targets in OSCC.

Paper I has several limitations. It is difficult to ascertain preclinically whether a biomarker is suitable for use as an imaging target. In addition to its level of expression and tumor-specific expression, several other factors must be considered. Other biomarker characteristics that have been suggested (*60*) include the following: 1) internalization by cancer cells, which could prolong and increase the imaging signal. 2) Accessibility, meaning that the biomarker should be accessible for the imaging probe, e.g, cell membrane receptors. 3) Stability; the biomarker should have a stable expression in different stages of cancer including primary tumor, metastases, and tumor recurrence. 4) Involvement in biological functions critical for cancer development (e.g., angiogenesis, tumor invasion and metastasis). Imaging of these processes could provide insight into disease progression.

A challenge in this paper was that the expression of the various biomarkers was only semi-quantitatively scored in normal epithelium (the superficial border) and not in the normal stroma surrounding tumor (at the deep border). In the normal stroma, only the expression in the different cell types was described. A similar semi-quantitative scoring of the expression in the normal stromal tissue would have been valuable; however, achieving uniformity in this regard may prove difficult due to the considerable variation in the distribution of various tissue types (e.g., vessels, nerve cells, muscle) within the normal stroma. This distribution is primarily dependent upon the anatomical location of the histology sample.

Some targets, like Integrin αvβ3, showed almost no expression in OSCC tissue, although other studies have demonstrated imaging potential with this biomarker in HNSCC (*116*,*117*). Several factors could account for this discrepancy, including variations in the immunohistochemistry technique and the assessment of results. Since

positive and negative staining have been carried out, the results are most likely valid. But, there is a risk of inaccurate or false negative results when performing immunohistochemistry, especially with targets, that are not routinely examined in the Department of Pathology. Potential problems are antibody specificity, tissue fixation and processing, antigen retrieval, as well as several technical factors including antibody concentration and incubation time.

There are also several problems when assessing the IHC-stained tissue samples. It is difficult for the human eye to quantify immunohistochemistry pictures consistently. There is a risk of interpretation subjectivity, especially when scored by various pathologists over time, with a very rough semiquantitative score. Digital pathology/AI interpretation is a method of evaluation that could be more consistent/have a higher degree of reproducibility. Digital pathology was not performed in this paper, but was implemented in Paper II and 3.

There are several promising imaging targets for HNSCC in the literature (*118*,*119*), which would have been interesting to include in Paper I. However, due to practical and financial considerations, this was not feasible. Some of the other promising targets where molecular imaging probes have been developed and tested in clinical trials include fibroblast activation protein inhibitor (FAPI) (*52*,*120*), epidermal growth factor receptor (EGFR) (*121*,*122*) and programmed death-ligand 1 (PD-L1) (*123*).

The role of [⁶⁸Ga]Ga-NOTA-AE105 PET/CT in OSCC and OPSCC

The aim of paper II was to examine the diagnostic value of [⁶⁸Ga]Ga-NOTA-AE105 PET/CT for identifying lymph node metastases, in patients diagnosed with OSCC and OPSCC planned for curative surgical treatment. We found that on a per-patient basis, the sensitivity and specificity were 56% and 100%, respectively. These numbers were equivalent to routine imaging (CT/MRI). This means that [⁶⁸Ga]Ga-NOTA-AE105 PET/CT can only correctly identify regional metastatic disease in 56% of cases where

one or more metastases are truly present. Thus, [^{68}Ga]Ga-NOTA-AE105 PET/CT has a high false negative rate, failing to identify 44% of patients with metastases. In contrast, this modality can correctly rule out metastases in all cases where the patients do not have regional disease. An additional 18% of patients with occult metastatic disease were detected when combining the diagnostic findings of [^{68}Ga]Ga-NOTA-AE105 PET/CT with the existing imaging workup, underlining that there is an added value of this modality compared to CT/MRI. These numbers are based on a per patient analysis approach, where the patient, as a whole, is positive or negative for regional disease, and not on a node-to-node analysis. The node-to-node analysis could provide a more detailed understanding of this imaging modality's performance, but was not considered practically possible.

The detection of smaller lymph nodes using [^{68}Ga]Ga-NOTA-AE105 PET/CT proved to be challenging. The PET positive lymph nodes differed significantly (p = 0.006) from the negative lymph nodes in terms of size; the median identified node measured 14 mm (range: 3-27 mm), whereas the negative nodes measured 5 mm (range: 0.1-10 mm). This suggests that the strength of the PET signal could be influenced by both the degree of uPAR expression in tumor cells and the size of the tumor. The median SUV$_{max}$ values for lymph node metastases and primary tumors were 2.62 and 2.83. This is considerable lower than the SUV$_{max}$ values seen in e.g [^{18}F]FDG-PET/CT (*13*,*124*), but is comparable to a previous study examining the prognostic value of [^{68}Ga]Ga-NOTA-AE105 PET/CT in advanced OSCC (*13*). This low uptake of the PET tracer makes it more challenging to detect smaller lesions (both primary tumors and metastases) and to delineate tumor from surrounding tissue; the sensitivity is reduced. Several pharmacokinetic and pharmacodynamic factors could have played a role in the relatively low SUV$_{max}$ values, including limited penetration into cancer tissue, heterogeneous or low target expression, and restricted binding affinity.

In Paper II, we found a significant correlation between uPAR expression in primary tumor determined by immunohistochemistry (product of H-score and tumor depth) and SUVmax, which confirms the uPAR-specificity of ^{68}Ga-NOTA-AE105 found in previous studies ([125],[126]).

However due to the low sensitivity of [^{68}Ga]Ga-NOTA-AE105 PET/CT for tumor tissue, this modality cannot be used for nodal staging in OSCC and OPSCC and is not able to replace the current surgical methods at our institution - sentinel node biopsy or neck dissection.

Paper II has other limitations. Initially, the study was estimated to include 90 patients; however, due to several issues including difficulties with recruiting patients, the Covid-19 pandemic, and issues with achieving PET time slots, it was not possible to include more than 61 patients. This increases the likelihood of a type II error and reduces the precision of the results.

The [^{68}Ga]Ga-NOTA-AE105 PET/CT results were compared with routine imaging (CT/MRI). A comparison between [^{68}Ga]Ga-NOTA-AE105 PET/CT and [^{18}F]FDG-PET/CT, the gold standard of molecular imaging in HNSCC, would have been preferable instead of comparing the results with routine imaging (CT/MRI). This was unfortunately not possible due to several reasons including the national fast track cancer patient pathway, where patients need to be diagnosed and surgically treated within a limited number of days.

Another constraint in this paper was related to the procedure of matching histology findings with PET images. In cases where a neck dissection reveals multiple lymph node metastases at a particular level of the neck but only one positive lymph node on [^{68}Ga]Ga-NOTA-AE105 PET/CT, the identity of the positive node among those that were dissected becomes ambiguous. Likewise, if the exact opposite is true. Reducing the risk of mismatch would necessitate exclusively including patients who underwent sentinel node biopsy, a procedure in which typically only one or two selected

nodes are evaluated. This would require the inclusion of a greater number of patients, given that sentinel node procedures are only performed on patients in whom metastases are not suspected and occur infrequently.

While PET-imaging using the radiotracer [^{68}Ga]Ga-NOTA-AE105 does not seem to be effective for the detection of lymph node metastases, it could potentially serve other purposes in HNSCC. A recent study at our institution investigated the prognostic value of this tracer in patients with advanced HNSCC who were referred for curative intended radiotherapy. The findings revealed that high SUV$_{max}$ values function as a predictor of recurrence and could potentially be used to identify patients with an increased risk of recurrence (*13*).

Patient derived xenograft models of oral squamous cell carcinoma

In the first part of Paper III, we created three new PDX mouse models of OSCC by transplanting pieces of tumor tissue from locally advanced OSCC patients into mice with compromised immune systems. When the tumor grew to a critical size in the first passage of mice, the tumor was engrafted and expanded in a new passage of mice. We found that the histological characteristics in the tumor cells and the stromal cells were stable from patient tumor through the different passages (P0-P2). The Ki-67 expression and uPAR expression remained consistent across the various passages and uPAR exhibited the same heterogeneous pattern. Our findings align with previous research, which has shown that histological characteristics and biomarker expression remain constant from donor tumor through the first passages (*127–129*).

The histological characteristics were evaluated by a specialized head and neck pathologist using qualitative description. In contrast, the expression of uPAR and Ki-67 was quantified and compared using digital pathology. The validation methodologies used to demonstrate that PDX models retain tumor characteristics from the donor tumor

49

is a limitation in this section of paper III. Quantitative analysis of histology characteristics and incorporation of additional HNSCC biomarkers into IHC analyses would have enhanced the study's validity. Furthermore, gene expression analysis and drawing comparisons between donor tumors and PDX models, as observed in some previously conducted PDX studies (*130*), would have added more detailed information regarding the level of similarity.

[^{64}Cu]Cu-DOTA-AE105 PET/CT in patient derived xenograft models

In the second part of Paper III, we studied the use of [^{64}Cu]Cu-DOTA-AE105 PET/CT in 29 tumors from three OSCC PDX-models. We found a heterogeneous uptake of [^{64}Cu]Cu-DOTA-AE105 in all the models.

A target-specific tracer uptake was visualized by comparing autoradiography and uPAR immunohistochemistry from the same tumor samples. The uPAR positive areas in tumor ,seen with immunohistochemistry, corresponded to the areas with high signal on autoradiography. We were not able to show a significant correlation between SUV_{max} values and H-scores measured from single cross sections through the tumors. The tumor specificity of [^{64}Cu]Cu-DOTA-AE105 was illustrated by comparing the autoradiography signal in tumor tissue and the signal in normal muscle tissue. The significant correlation we found between tumor growth and uPAR expression indicates a prognostic potential of uPAR targeted imaging as demonstrated by Risør et al. in a phase II trial (*13*).

This paper is the first to study the tracer [^{64}Cu]Cu-DOTA-AE105 in heterogenous HNSCC. So far this tracer has only been investigated in a single study using homogenous cell line models (*131*). In theory, the isotope ^{64}Cu utilized in Paper III has the potential to improve the precision and accuracy of detecting smaller tumor volumes compared to the isotope ^{68}Ga employed in Paper II. This is due to the shorter positron

range of ^{64}Cu (1mm) compared to ^{68}Ga (4 mm). Therefore, it might be interesting to explore the tracer [^{64}Cu]Cu-DOTA-AE105 in patients with HNSCC.

In summary, these findings suggest that OSCC PDX models are suitable for studying novel molecular imaging techniques, such as [^{64}Cu]Cu-DOTA-AE105 PET/CT, and may more accurately mimic real tumor tissue compared to the more homogeneous cell line xenograft models. Furthermore, the tracer exhibits specificity towards both the target (uPAR) and tumor in OSCC PDX models. Finally, the findings confirm existing research indicating that uPAR may possess prognostic capabilities in HNSCC.

Conclusion

In conclusion, the findings presented in this thesis underscore that uPAR is highly expressed in OSCC primary tumors and metastases with an expression pattern that makes it interesting as a target for molecular imaging, also compared to several other promising imaging targets.

As a diagnostic tool for identifying lymph node metastases in OSCC and OPSCC, [68Ga]Ga-NOTA-AE105-PET/CT has shown high specificity, but a sensitivity to low for staging of nodal disease. The modality is limited in identifying smaller volumes and is therefore not able to replace sentinel node dissection. The diagnostic accuracy is comparable to routine imaging modalities (CT/MRI). There is an added value of [68Ga]Ga-NOTA-AE105-PET/CT when combined with routine imaging which suggest a diagnostic potential.

We have presented evidence that it is possible to successfully create OSCC PDX models, which exhibit histological characteristics and uPAR expression that closely resemble those of donor tumors. [64Cu]Cu-DOTA-AE105 PET/CT is found as a tumor and target specific tracer in OSCC PDX-models. The correlation between uPAR expression and tumor growth, suggests a prognostic potential of uPAR-PET imaging in OSCC tumors.

Perspectives for further research

There is a great need to improve the non-invasive diagnostic tools for patients with oral and oropharyngeal carcinoma to achieve more accurate nodal staging and improved pre -and perioperative visualization of the extent of the primary tumor.

The biomarker uPAR exhibits several potential applications within the field of molecular imaging, including prognostic, therapeutic, and diagnostic capabilities (*13,132*).

First, there is a diagnostic potential in PET imaging for staging. The modality [^{68}Ga]Ga-NOTA-AE105 PET/CT is not a diagnostic tool which can be used for staging OSCC and OPSCC, but we have shown that there is a diagnostic potential in uPAR targeted PET imaging. Given the observed improvement in metastatic disease detection for uPAR-PET combined with MRI, it is conceivable that uPAR-PET/MRI could increase sensitivity. Additionally, alternative isotopes such as ^{64}Cu have the potential to improve resolution, thereby enhancing the accuracy of diagnostics. This is a path which could be interesting to investigate further, especially since the tracer [^{64}Cu]Cu-DOTA-AE105 is already available. Secondly, there is a prognostic potential in uPAR-targeted imaging. We demonstrated a significant positive correlation between tumor growth and uPAR expression. Consistent with this, a recent clinical study at our institution found a prognostic value of [^{68}Ga]Ga-uPAR PET in HNSCC (*13*). It is therefore plausible that uPAR targeted imaging can assist in the process of risk stratification of patients, which could be useful in, e.g., de-escalating strategies, discussed for HPV-positive HNSCC tumors (*133*), or risk stratified follow-up schemes.

Thirdly, there is therapeutic potential within uPAR-targeted molecular imaging. An area of investigation at present at our institution is uPAR-targeted fluorescence-guided surgery. This modality involves the injection of a uPAR-targeting fluorescent probe prior to primary tumor resection. Following this, the surgeon employs a fluorescence camera to delineate the tumor. An additional intriguing aspect of fluorescence-guided surgery is the increasing utilization of transoral robotic surgery for patients with oropharyngeal carcinoma. This is because these robots come with the technology for detecting

fluorescence emission; thus, the technology is already in the operation room. uPAR-targeting PET-imaging could potentially be used as a diagnostic companion to select patients for uPAR-targeted fluorescence-guided surgery. The hope is that this could result in a reduced frequency of patients with T -and N-site recurrence for patients with HNSCC.

uPAR targeted radionuclide therapy is another therapeutic modality which could be interesting to look further into. In radionuclide therapy, radioisotopes (alfa- or beta-particle emitting agents) are delivered to tumor-associated targets, e.g., a biomarker expressed on cancer cells or in the tumor microenvironment, and the harmful ionizing radiation harms the adjacent cells. This modality exploits the selective accumulation of radioactive particles within tumor tissue to deliver therapeutic doses, while the doses in healthy tissue are limited. There are many advantages with this modality compared to conventional radiotherapy, including the possibility to assess the amount of target cells before therapy, limited toxicity to normal tissue, and the option for treating several metastases at the same time. Radionuclide therapy has been used for many years for patients with thyroid cancer (*134*) and has recently been available for patients with prostate-specific membrane antigen(PSMA)-positive prostate cancer (*135*) and patients with somatostatin-receptor-positive neuroendocrine tumors (*136*).

Well-defined PDX mouse models expressing uPAR as developed in Paper III, with either subcutaneous tumors or implantation of tumors in the head and neck mucosa (orthotopic PDX mouse models) could work as a translational platform for further developing diagnostic, prognostic, and therapeutic uPAR-targeted molecular imaging modalities for patients with HNSCC.

References

1. Shimizu KI, Inoue H, Saitoh M, et al. Distribution and impact of lymph node metastases in oropharyngeal cancer. *Acta Otolaryngol*. 2006;126:872-877.

2. Amit M, Yen TC, Liao CT, et al. Clinical nodal stage is a significant predictor of outcome in patients with oral cavity squamous cell carcinoma and pathologically negative neck metastases: Results of the international consortium for outcome research. *Ann Surg Oncol*. 2013;20:3575-3581.

3. Barrera JE, Miller ME, Said S, Jafek BW, Campana JP, Shroyer KR. Detection of occult cervical micrometastases in patients with head and neck squamous cell cancer. *Laryngoscope*. 2003;113:892-896.

4. Orosco RK, Tapia VJ, Califano JA, et al. Positive Surgical Margins in the 10 Most Common Solid Cancers. *Sci Rep*. 2018;8.

5. Binahmed A, Nason RW, Abdoh AA. The clinical significance of the positive surgical margin in oral cancer. *Oral Oncol*. 2007;43:780-784.

6. Mcmahon J, O'brien CJ, Pathak I, et al. Influence of condition of surgical margins on local recurrence and disease-specific survival in oral and oropharyngeal cancer. *Br J Oral Maxillofac Surg*. 2003;41:224-231.

7. Jakobsen KK, Grønhøj C, Jensen DH, et al. Increasing incidence and survival of head and neck cancers in Denmark: a nation-wide study from 1980 to 2014. *Acta Oncol (Madr)*. 2018;57:1143-1151.

8. Christensen A, Kiss K, Lelkaitis G, et al. Urokinase-type plasminogen activator receptor (uPAR), tissue factor (TF) and epidermal growth factor receptor (EGFR): Tumor expression patterns and prognostic value in oral cancer. *BMC Cancer*. 2017;17.

9. C. Boonstra M, W. Verspaget H, Ganesh S, et al. Clinical Applications of the Urokinase Receptor (uPAR) for Cancer Patients. *Curr Pharm Des*. 2011;17:1890-

1910.

10. Noh H, Hong S, Huang S. Role of urokinase receptor in tumor progression and development. *Theranostics*. 2013;3:487-495.

11. Fosbøl MØ, Kurbegovic S, Johannesen HH, et al. Urokinase-Type Plasminogen Activator Receptor (uPAR) PET/MRI of Prostate Cancer for Noninvasive Evaluation of Aggressiveness: Comparison with Gleason Score in a Prospective Phase 2 Clinical Trial. *J Nucl Med*. 2021;62:354-359.

12. Carlsen EA, Loft M, Loft A, et al. Prospective Phase II Trial of Prognostication by 68Ga-NOTA-AE105 uPAR PET in Patients with Neuroendocrine Neoplasms: Implications for uPAR-Targeted Therapy. *J Nucl Med*. 2022;63:1371-1377.

13. Risoer LM, Clausen MM, ujmajuridze zaza, et al. Prognostic value of Urokinase-type Plasminogen Activator Receptor (uPAR)-PET/CT in Head and Neck Squamous Cell Carcinomas and Comparison with 18 F-FDG-PET/CT: A single-center prospective study . *J Nucl Med*. 2021:jnumed.121.262866.

14. Sung H, Ferlay J, Siegel RL, et al. Global Cancer Statistics 2020: GLOBOCAN Estimates of Incidence and Mortality Worldwide for 36 Cancers in 185 Countries. *CA Cancer J Clin*. 2021;71:209-249.

15. Lambert R, Sauvaget C, De Camargo Cancela M, Sankaranarayanan R. Epidemiology of cancer from the oral cavity and oropharynx. *Eur J Gastroenterol Hepatol*. 2011;23:633-641.

16. Gormley M, Creaney G, Schache A, Ingarfield K, Conway DI. Reviewing the epidemiology of head and neck cancer: definitions, trends and risk factors. *Br Dent J*. 2022;233:780-786.

17. Fenger Carlander A-L, Grønhøj Larsen C, Hebbelstrup Jensen D, et al. Continuing rise in oropharyngeal cancer in a high HPV prevalence area: A Danish population-based study from 2011 to 2014. *Eur J Cancer*. 2017;70:75-82.

18. Zamani M, Grønhøj C, Jensen DH, et al. The current epidemic of HPV-associated oropharyngeal cancer: An 18-year Danish population-based study with 2,169 patients. *Eur J Cancer*. 2020;134:52-59.

19.   Mehanna H, Taberna M, von Buchwald C, et al. Prognostic implications of p16 and HPV discordance in oropharyngeal cancer (HNCIG-EPIC-OPC): a multicentre, multinational, individual patient data analysis. *Lancet Oncol.* 2023;24:239-251.

20.   Wang Y, Ow TJ, Myers JN. Pathways for cervical metastasis in malignant neoplasms of the head and neck region. *Clin Anat.* 2012;25:54-71.

21.   Takes RP, Rinaldo A, Silver CE, et al. Distant metastases from head and neck squamous cell carcinoma. Part I. Basic aspects. *Oral Oncol.* 2012;48:775-779.

22.   Faisal M, Dhanani R, Ullah S, et al. Prognostic outcomes of treatment naïve oral tongue squamous cell carcinoma (OTSCC): a comprehensive analysis of 14 years. *Eur Arch Oto-Rhino-Laryngology.* 2021;278:3045-3053.

23.   Teraphongphom N, Kong CS, Warram JM, Rosenthal EL. Specimen mapping in head and neck cancer using fluorescence imaging. *Laryngoscope Investig Otolaryngol.* 2017;2:447-452.

24.   Schilling C, Stoeckli SJ, Haerle SK, et al. Sentinel European Node Trial (SENT): 3-year results of sentinel node biopsy in oral cancer. *Eur J Cancer.* 2015;51:2777-2784.

25.   Mehanna H, Wong W-L, McConkey CC, et al. PET-CT Surveillance versus Neck Dissection in Advanced Head and Neck Cancer. *N Engl J Med.* 2016;374:1444-1454.

26.   Senft A, de Bree R, Hoekstra OS, et al. Screening for distant metastases in head and neck cancer patients by chest CT or whole body FDG-PET: A prospective multicenter trial. *Radiother Oncol.* 2008;87:221-229.

27.   Cacicedo J, Fernandez I, del Hoyo O, et al. Should PET/CT be implemented in the routine imaging work-up of locally advanced head and neck squamous cell carcinoma? A prospective analysis. *Eur J Nucl Med Mol Imaging.* 2015;42:1378-1389.

28.   Haerle SK, Schmid DT, Ahmad N, Hany TF, Stoeckli SJ. The value of 18F-FDG PET/CT for the detection of distant metastases in high-risk patients with head and

neck squamous cell carcinoma. *Oral Oncol.* 2011;47:653-659.

29. Rudmik L, Lau HY, Matthews TW, et al. Clinical utility of PET/CT in the evaluation of head and neck squamous cell carcinoma with an unknown primary: A prospective clinical trial. *Head Neck.* 2011;33:935-940.

30. Ferris RL, Cramer JD, Branstetter BF. Positron Emission Tomography/Computed Tomography in Evaluation of the Clinically N0 Neck in Head and Neck Squamous Cell Carcinoma. *J Clin Oncol.* 2019;37:1683.

31. Sohn B, Koh YW, Kang WJ, Lee JH, Shin NY, Kim J. Is there an additive value of 18 F-FDG PET-CT to CT/MRI for detecting nodal metastasis in oropharyngeal squamous cell carcinoma patients with palpably negative neck? *Acta radiol.* 2016;57:1352-1359.

32. Lowe VJ, Duan F, Subramaniam RM, et al. Multicenter Trial of [18F]fluorodeoxyglucose Positron Emission Tomography/Computed Tomography Staging of Head and Neck Cancer and Negative Predictive Value and Surgical Impact in the N0 Neck: Results From ACRIN 6685. *J Clin Oncol.* 2019;37:1704.

33. Plaxton NA, Brandon DC, Corey AS, et al. Characteristics and limitations of FDG PET/CT for imaging of squamous cell carcinoma of the head and neck: A comprehensive review of anatomy, metastatic pathways, and image findings. *Am J Roentgenol.* 2015;205:W519-W531.

34. Purohit BS, Ailianou A, Dulguerov N, Becker CD, Ratib O, Becker M. FDG-PET/CT pitfalls in oncological head and neck imaging. *Insights Imaging.* 2014;5:585.

35. Dahanca. Danish Head and Neck Cancer Group. https://www.dahanca.dk/.

36. Nichols AC, Theurer J, Prisman E, et al. Radiotherapy versus transoral robotic surgery and neck dissection for oropharyngeal squamous cell carcinoma (ORATOR): an open-label, phase 2, randomised trial. *Lancet Oncol.* 2019;20:1349-1359.

37. Rubek N, Channir HI, Charabi BW, et al. Primary transoral robotic surgery with concurrent neck dissection for early stage oropharyngeal squamous cell

carcinoma implemented at a Danish head and neck cancer center: a phase II trial on feasibility and tumour margin status. *Eur Arch Oto-Rhino-Laryngology*. 2017;274:2229-2237.

38. von Buchwald C, Rubek N, Channir HI. Quality of Life After primary TORS vs IMRT " The QoLATI study " for patients with early-stage oropharyngeal squamous cell carcinoma : A Randomized National Trial Registered DAHANCA 34 protocol. *https://dahanca.dk/assets/files/PRO_DAHANCA%2034.pdf*. 2018.

39. Berlin E, Ma DJ, Bakst RL, Quon H, Lin A, Lukens JN. Close Margins After Transoral Robotic Surgery for Human Papillomavirus–Positive Oropharyngeal Carcinoma: A Review of the Literature and Practical Recommendations. *Pract Radiat Oncol*. 2023;13:251-255.

40. Woolgar JA, Triantafyllou A. A histopathological appraisal of surgical margins in oral and oropharyngeal cancer resection specimens. *Oral Oncol*. 2005;41:1034-1043.

41. Du E, Ow TJ, Lo YT, et al. Refining the utility and role of Frozen section in head and neck squamous cell carcinoma resection. *Laryngoscope*. 2016;126:1768-1775.

42. D'Cruz AK, Vaish R, Kapre N, et al. Elective versus Therapeutic Neck Dissection in Node-Negative Oral Cancer. *N Engl J Med*. 2015;373:521-529.

43. Ding Z, Li Y, Pan X, Xuan M, Xie H, Wang X. Sentinel lymph node biopsy versus elective neck dissection in squamous cell carcinoma of the oral cavity with a clinically N0 neck: Systematic review and meta-analysis of prospective studies. *Head Neck*. 2021;43:3185-3198.

44. Kim YJ, Kim JH. Increasing incidence and improving survival of oral tongue squamous cell carcinoma. *Sci Rep*. 2020;10:1-11.

45. Olsen MH, Frederiksen K, Lassen P, et al. Association of Smoking, Comorbidity, Clinical Stage, and Treatment Intent with Socioeconomic Differences in Survival after Oropharyngeal Squamous Cell Carcinoma in Denmark. *JAMA Netw Open*. 2022;5:E2245510.

46. Mankoff DA. A definition of molecular imaging. *J Nucl Med*. 2007;48.

47. McDermott S, Kilcoyne A. Editor's choice: Molecular imaging—its current role in cancer. *QJM An Int J Med*. 2016;109:295.

48. Weissleder R, Pittet MJ. Imaging in the era of molecular oncology. *Nature*. 2008;452:580-589.

49. Kircher MF, Hricak H, Larson SM. Molecular imaging for personalized cancer care. *Mol Oncol*. 2012;6:182-195.

50. Marcus C, Subramaniam RM. Role of Non-FDG-PET/CT in Head and Neck Cancer. *Semin Nucl Med*. 2021;51:68-78.

51. Röhrich M. Fibroblast Activation Protein Inhibitor PET Imaging in Head and Neck Cancer. *PET Clin*. 2023;18:315-323.

52. Jiang Y, Wen B, Li C, et al. The performance of 68Ga-FAPI-04 PET/CT in head and neck squamous cell carcinoma: a prospective comparison with 18F-FDG PET/CT. *Eur J Nucl Med Mol Imaging*. 2023;50:2114-2126.

53. Basu S, Kwee TC, Surti S, Akin EA, Yoo D, Alavi A. Fundamentals of PET and PET/CT imaging. *Ann N Y Acad Sci*. 2011;1228:1-18.

54. James ML, Gambhir SS. A molecular imaging primer: Modalities, imaging agents, and applications. *Physiol Rev*. 2012;92:897-965.

55. Fonti R, Conson M, Del Vecchio S. PET/CT in radiation oncology. *Semin Oncol*. 2019;46:202-209.

56. Pysz MA, Gambhir SS, Willmann JK. Molecular Imaging: Current Status and Emerging Strategies. *Clin Radiol*. 2010;65:500.

57. Derlin T, Grünwald V, Steinbach J, Wester HJ, Ross TL. Molekulare Bildgebung in der Onkologie mittels Positronenemissionstomographie. *Dtsch Arztebl Int*. 2018;115:175-181.

58. Hanahan D, Weinberg RA. Hallmarks of cancer: The next generation. *Cell*. 2011;144:646-674.

59. Boonstra MC, De Geus SWL, Prevoo HAJM, et al. Selecting Targets for Tumor Imaging: An Overview of Cancer-Associated Membrane Proteins. *Biomark*

Cancer. 2016;8:BIC.S38542.

60. Van Oosten M, Crane LMA, Bart J, Van Leeuwen FW, Van Dam GM. Selecting Potential Targetable Biomarkers for Imaging Purposes in Colorectal Cancer Using TArget Selection Criteria (TASC): A Novel Target Identification Tool. *Transl Oncol.* 2011;4:71-82.

61. Jacobsen B, Ploug M. The Urokinase Receptor and its Structural Homologue C4.4A in Human Cancer: Expression, Prognosis and Pharmacological Inhibition. *Curr Med Chem.* 2008;15:2559-2573.

62. Floridon C, Nielsen O, Hølund B, et al. Localization and significance of urokinase plasminogen activator and its receptor in placental tissue from intrauterine, ectopic and molar pregnancies. *Placenta.* 1999;20:711-721.

63. Solberg H, Ploug M, Høyer-Hansen G, Nielsen BS, Lund LR. The murine receptor for urokinase-type plasminogen activator is primarily expressed in tissues actively undergoing remodeling. *J Histochem Cytochem.* 2001;49:237-246.

64. Beschorner R, Schluesener HJ, Nguyen TD, et al. Lesion-associated accumulation of uPAR/CD87- expressing infiltrating granulocytes, activated microglial cells/macrophages and upregulation by endothelial cells following TBI and FCI in humans. *Neuropathol Appl Neurobiol.* 2000;26:522-527.

65. Gutova M, Najbauer J, Gevorgyan A, et al. Identification of uPAR-positive Chemoresistant Cells in Small Cell Lung Cancer. *PLoS One.* 2007;2.

66. Illemann M, Bird N, Majeed A, et al. Two distinct expression patterns of urokinase, urokinase receptor and plasminogen activator inhibitor-1 in colon cancer liver metastases. *Int J Cancer.* 2009;124:1860-1870.

67. Nielsen BS, Rank F, Illemann M, Lund LR, Danø K. Stromal cells associated with early invasive foci in human mammary ductal carcinoma in situ coexpress urokinase and urokinase receptor. *Int J Cancer.* 2007;120:2086-2095.

68. Christensen A, Grønhøj C, Jensen JS, et al. Expression patterns of uPAR, TF and EGFR and their potential as targets for molecular imaging in oropharyngeal squamous cell carcinoma. *Oncol Rep.* 2022;48.

69. Andreasen PA, Egelund R, Petersen HH. The plasminogen activation system in tumor growth, invasion, and metastasis. *Cell Mol Life Sci*. 2000;57:25-40.

70. Lv T, Zhao Y, Jiang X, et al. uPAR: An Essential Factor for Tumor Development. *J Cancer*. 2021;12:7026.

71. Schnapp LM, Wilson CL, Hung CF. Integrins. *Encycl Respir Med Second Ed*. 2021;1:123-129.

72. Ahmedah HT, Patterson LH, Shnyder SD, Sheldrake HM. RGD-Binding Integrins in Head and Neck Cancers. *Cancers (Basel)*. 2017;9.

73. Brooks PC, Clark RAF, Cheresh DA. Requirement of vascular integrin αvβ3 for angiogenesis. *Science (80-)*. 1994;264:569-571.

74. Fabricius EM, Wildner GP, Kruse-Boitschenko U, Hoffmeister B, Goodman SL, Raguse JD. Immunohistochemical analysis of integrins αvβ3, αvβ5 and α5β1, and their ligands, fibrinogen, fibronectin, osteopontin and vitronectin, in frozen sections of human oral head and neck squamous cell carcinomas. *Exp Ther Med*. 2011;2:9-19.

75. Li P, Liu F, Sun L, et al. Chemokine receptor 7 promotes cell migration and adhesion in metastatic squamous cell carcinoma of the head and neck by activating integrin αvβ3. *Int J Mol Med*. 2011;27:679-687.

76. Beer AJ, Haubner R, Sarbia M, et al. Positron emission tomography using [18F]Galacto-RGD identifies the level of integrin αvβ3 expression in man. *Clin Cancer Res*. 2006;12:3942-3949.

77. Beer AJ, Schwaiger M. Imaging of integrin αvβ3 expression. *Cancer Metastasis Rev*. 2008;27:631-644.

78. Li HX, Zheng JH, Fan HX, Li HP, Gao ZX, Chen D. Expression of αvβ6 integrin and collagen fibre in oral squamous cell carcinoma: association with clinical outcomes and prognostic implications. *J Oral Pathol Med*. 2013;42:547-556.

79. Ramos DM, Dang D, Sadler S. The role of the integrin αvβ6 in regulating the epithelial to mesenchymal transition in oral cancer. *Anticancer Res*. 2009;29:125-130.

80. Niu J, Li Z. The roles of integrin αvβ6 in cancer. *Cancer Lett.* 2017;403:128-137.

81. Baart VM, van Duijn C, van Egmond SL, et al. Egfr and αvβ6 as promising targets for molecular imaging of cutaneous and mucosal squamous cell carcinoma of the head and neck region. *Cancers (Basel).* 2020;12.

82. Hausner SH, Bold RJ, Cheuy LY, et al. Preclinical development and first-in-human imaging of the integrin a v b 6 with [18 F]a v b 6 -binding peptide in metastatic carcinoma. *Clin Cancer Res.* 2019;25:1206-1215.

83. Gerard Quigley N, Steiger K, Hoberück S, et al. PET/CT imaging of head-and-neck and pancreatic cancer in humans by targeting the "Cancer Integrin" αvβ6 with Ga-68-Trivehexin. *Eur J Nucl Med Mol Imaging.* 2022;49:1136-1147.

84. Kasthuri RS, Taubman MB, Mackman N. Role of Tissue Factor in Cancer. *J Clin Oncol.* 2009;27:4834.

85. Wei W, Liu Q, Jiang D, et al. Tissue Factor-Targeted ImmunoPET Imaging and Radioimmunotherapy of Anaplastic Thyroid Cancer. *Adv Sci.* 2020;7.

86. Takashima H, Tsuji AB, Saga T, et al. Molecular imaging using an anti-human tissue factor monoclonal antibody in an orthotopic glioma xenograft model. *Sci Reports 2017 71.* 2017;7:1-13.

87. Sugyo A, Aung W, Tsuji AB, et al. Anti-tissue factor antibody-mediated immuno-SPECT imaging of tissue factor expression in mouse models of pancreatic cancer. *Oncol Rep.* 2019;41:2371-2378.

88. Ossovskaya V, Koo IC, Kaldjian EP, Alvares C, Sherman BM. Upregulation of poly (ADP-Ribose) polymerase-1 (PARP1) in triple-negative breast cancer and other primary human tumor types. *Genes and Cancer.* 2010;1:812-821.

89. Wang F, Gouttia OG, Wang L, Peng A. PARP1 Upregulation in Recurrent Oral Cancer and Treatment Resistance. *Front Cell Dev Biol.* 2022;9:1-9.

90. Wang L, Liang C, Li F, et al. PARP1 in Carcinomas and PARP1 Inhibitors as Antineoplastic Drugs. *Int J Mol Sci.* 2017;18.

91. Schöder H, de Souza França PD, Nakajima R, et al. Safety and feasibility of PARP1/2 imaging with 18F-PARPi in patients with head and neck cancer. *Clin*

Cancer Res. 2020;26:3110-3116.

92. Demétrio de Souza França P, Kossatz S, Brand C, et al. A phase I study of a PARP1-targeted topical fluorophore for the detection of oral cancer. *Eur J Nucl Med Mol Imaging.* May 2021:1-13.

93. Carmeliet P. VEGF as a key mediator of angiogenesis in cancer. *Oncology.* 2005;69:4-10.

94. Denhart BC, Guidi AJ, Tognazzi K, Dvorak HF, Brown LF. Vascular permeability factor/vascular endothelial growth factor and its receptors in oral and laryngeal squamous cell carcinoma and dysplasia. *Lab Investig.* 1997;77:659-664.

95. Stîngă AC, Mărgăritescu O, Stîngă AS, et al. VEGFR1 and VEGFR2 immunohistochemical expression in oral squamous cell carcinoma: A morphometric study. *Rom J Morphol Embryol.* 2011;52:1269-1275.

96. Masłowska K, Halik PK, Tymecka D, Misicka A, Gniazdowska E. The Role of VEGF Receptors as Molecular Target in Nuclear Medicine for Cancer Diagnosis and Combination Therapy. *Cancers (Basel).* 2021;13:1-46.

97. Winter MJ, Nagtegaal ID, Van Krieken JHJM, Litvinov S V. The Epithelial Cell Adhesion Molecule (Ep-CAM) as a Morphoregulatory Molecule Is a Tool in Surgical Pathology. *Am J Pathol.* 2003;163:2139.

98. Baeuerle PA, Gires O. EpCAM (CD326) finding its role in cancer. *Br J Cancer.* 2007;96:417-423.

99. MacDonald GC, Rasamoelisolo M, Entwistle J, et al. A phase I clinical study of intratumorally administered VB4-845, an anti-epithelial cell adhesion molecule recombinant fusion protein, in patients with squamous cell carcinoma of the head and neck. *Med Oncol.* 2009;26:257-264.

100. van Driel PBAA, Boonstra MC, Prevoo HAJM, et al. EpCAM as multi-tumour target for near-infrared fluorescence guided surgery. *BMC Cancer.* 2016;16.

101. Boogerd LSF, Boonstra MC, Prevoo HAJM, et al. Fluorescence-guided tumor detection with a novel anti-EpCAM targeted antibody fragment: Preclinical validation. *Surg Oncol.* 2019;28:1-8.

102. Vorobyeva A, Bezverkhniaia E, Konovalova E, et al. Radionuclide Molecular Imaging of EpCAM Expression in Triple-Negative Breast Cancer Using the Scaffold Protein DARPin Ec1. *Molecules*. 2020;25.

103. Pontious C, Kaul S, Hong M, et al. Cathepsin E Expression and Activity: Role in the Detection and Treatment of Pancreatic Cancer. *Pancreatology*. 2019;19:951.

104. Keliher EJ, Reiner T, Earley S, et al. Targeting Cathepsin E in Pancreatic Cancer by a Small Molecule Allows In Vivo Detection 1,2. *Neoplasia*. 2013;15:684-693.

105. Abd-Elgaliel WR, Cruz-Monserrate Z, Logsdon CD, Tung CH. Molecular imaging of Cathepsin E-positive tumors in mice using a novel protease-activatable fluorescent probe. *Mol Biosyst*. 2011;7:3207.

106. Pantelouris EM. Absence of Thymus in a Mouse Mutant. *Nat 1968 2175126*. 1968;217:370-371.

107. Tentler JJ, Tan AC, Weekes CD, et al. Patient-derived tumour xenografts as models for oncology drug development. *Nat Rev Clin Oncol*. 2012;9:338-350.

108. Abdolahi S, Ghazvinian Z, Muhammadnejad S, Saleh M, Asadzadeh Aghdaei H, Baghaei K. Patient-derived xenograft (PDX) models, applications and challenges in cancer research. *J Transl Med*. 2022;20.

109. Jensen JS, Jakobsen KK, Mirian C, et al. The Copenhagen Oral Cavity Squamous Cell Carcinoma database: Protocol and report on establishing a comprehensive oral cavity cancer database. *Clin Epidemiol*. 2019;11:733-741.

110. Fedchenko N, Reifenrath J. Different approaches for interpretation and reporting of immunohistochemistry analysis results in the bone tissue - a review. *Diagn Pathol*. 2014;9:221.

111. van der Fels CAM, Palthe S, Buikema H, van den Heuvel MC, Leliveld A, de Jong IJ. Potential receptors for targeted imaging of lymph node metastases in penile cancer. *Diagnostics*. 2020;10.

112. Bankhead P, Loughrey MB, Fernández JA, et al. QuPath: Open source software for digital pathology image analysis. *Sci Rep*. 2017;7.

113. Skovgaard D, Persson M, Brandt-Larsen M, et al. Safety, Dosimetry, and Tumor

Detection Ability of 68Ga-NOTA-AE105: First-in-Human Study of a Novel Radioligand for uPAR PET Imaging. *J Nucl Med*. 2017;58:379-386.

114. Nielsen CH, Erlandsson M, Jeppesen TE, et al. Quantitative PET Imaging of Tissue Factor Expression Using 18F-Labeled Active Site–Inhibited Factor VII. *J Nucl Med*. 2016;57:89-95.

115. Food and Drug Administration. FDA grants accelerated approval to tisotumab vedotin-tftv for recurrent or metastatic cervical cancer. U.S Food and Drug administration. https://www.fda.gov/drugs/resources-information-approved-drugs/fda-grants-accelerated-approval-tisotumab-vedotin-tftv-recurrent-or-metastatic-cervical-cancer.

116. Durante S, Dunet V, Gorostidi F, et al. Head and neck tumors angiogenesis imaging with 68Ga-NODAGA-RGD in comparison to 18F-FDG PET/CT: a pilot study. *EJNMMI Res*. 2020;10.

117. Lobeek D, Rijpkema M, Terry SYA, et al. Imaging angiogenesis in patients with head and neck squamous cell carcinomas by [68Ga]Ga-DOTA-E-[c(RGDfK)]2 PET/CT. *Eur J Nucl Med Mol Imaging*. 2020;47:2647-2655.

118. Wu J, Yuan Y, Tao XF, Lyu P. Targeted molecular imaging of head and neck squamous cell carcinoma: a window into precision medicine. *Chin Med J (Engl)*. 2020;133:1325.

119. Hanna C, Kwok L, Finlay-Schultz J, Sartorius CA, Cittelly DM. Labeling of Breast Cancer Patient-derived Xenografts with Traceable Reporters for Tumor Growth and Metastasis Studies. *J Vis Exp*. 2016.

120. Linz C, Brands RC, Kertels O, et al. Targeting fibroblast activation protein in newly diagnosed squamous cell carcinoma of the oral cavity – initial experience and comparison to [18F]FDG PET/CT and MRI. *Eur J Nucl Med Mol Imaging*. 2021;48:3951-3960.

121. Vonk J, De Wit JG, Voskuil FJ, et al. Epidermal Growth Factor Receptor–Targeted Fluorescence Molecular Imaging for Postoperative Lymph Node Assessment in Patients with Oral Cancer. *J Nucl Med*. 2022;63:672-678.

122. de Wit JG, Vonk J, Voskuil FJ, et al. EGFR-targeted fluorescence molecular imaging for intraoperative margin assessment in oral cancer patients: a phase II trial. *Nat Commun.* 2023;14.

123. Verhoeff SR, van de Donk PP, Aarntzen EHJG, et al. 89Zr-DFO-Durvalumab PET/CT Before Durvalumab Treatment in Patients with Recurrent or Metastatic Head and Neck Cancer. *J Nucl Med.* 2022;63:1523-1530.

124. Koekkoek-doll PK De, Vogel W, Maas M, Castelijns J, Smit L. ajnmmi0011-0178-SUV max values at FDG PET-CT to predict malignancy in lymph nodes. 2021;11:178-187.

125. Persson M, Skovgaard D, Brandt-Larsen M, et al. First-in-human uPAR PET: Imaging of Cancer Aggressiveness. *Theranostics.* 2015;5:1303.

126. Persson M, Madsen J, Østergaard S, et al. Quantitative PET of human urokinase-type plasminogen activator receptor with 64Cu-DOTA-AE105: Implications for visualizing cancer invasion. *J Nucl Med.* 2012;53:138-145.

127. Kang HN, Kim JH, Park AY, et al. Establishment and characterization of patient-derived xenografts as paraclinical models for head and neck cancer. *BMC Cancer.* 2020;20.

128. Swick AD, Stein AP, McCulloch TM, et al. Defining the boundaries and expanding the utility of head and neck cancer patient derived xenografts. *Oral Oncol.* 2017;64:65.

129. Makita H, Endo K, Kasahara Y, et al. Xenografts derived from patients with head and neck cancer recapitulate patient tumour properties. *Oncol Lett.* 2021;21.

130. Schuch LF, Silveira FM, Wagner VP, et al. Head and neck cancer patient-derived xenograft models – A systematic review. *Crit Rev Oncol Hematol.* 2020;155:103087.

131. Christensen A, Juhl K, Persson M, et al. uPAR-targeted optical near-infrared (NIR) fluorescence imaging and PET for image-guided surgery in head and neck cancer: Proof-of-concept in orthotopic xenograft model. *Oncotarget.* 2017;8:15407-15419.

132. Masucci MT, Minopoli M, Di Carluccio G, Motti ML, Carriero MV. Therapeutic Strategies Targeting Urokinase and Its Receptor in Cancer. *Cancers (Basel)*. 2022;14.

133. Chen AM. De-escalated radiation for human papillomavirus virus-related oropharyngeal cancer: evolving paradigms and future strategies. *Front Oncol*. 2023;13:1-12.

134. Sgouros G, Bodei L, McDevitt MR, Nedrow JR. Radiopharmaceutical therapy in cancer: clinical advances and challenges. *Nat Rev Drug Discov 2020 199*. 2020;19:589-608.

135. Sartor O, de Bono J, Chi KN, et al. Lutetium-177–PSMA-617 for Metastatic Castration-Resistant Prostate Cancer. *N Engl J Med*. 2021;385:1091-1103.

136. Strosberg J, El-Haddad G, Wolin E, et al. Phase 3 Trial of 177 Lu-Dotatate for Midgut Neuroendocrine Tumors . *N Engl J Med*. 2017;376:125-135.

Article

Potential of uPAR, αvβ6 Integrin, and Tissue Factor as Targets for Molecular Imaging of Oral Squamous Cell Carcinoma: Evaluation of Nine Targets in Primary Tumors and Metastases by Immunohistochemistry

Mads Lawaetz [1,2,*], Anders Christensen [1,2], Karina Juhl [2], Kirstine Karnov [1,2,†], Giedrius Lelkaitis [3], Anne-Marie Kanstrup Fiehn [3,4], Andreas Kjaer [2] and Christian von Buchwald [1]

[1] Department of Otolaryngology, Head and Neck Surgery and Audiology, Rigshospitalet, Copenhagen University Hospital, 2100 Copenhagen, Denmark
[2] Department of Clinical Physiology, Nuclear Medicine and PET and Cluster for Molecular Imaging, Copenhagen University Hospital-Rigshospitalet & Department of Biomedical Sciences, University of Copenhagen, 2100 Copenhagen, Denmark
[3] Department of Pathology, Rigshospitalet, Copenhagen University Hospital, 2100 Copenhagen, Denmark
[4] Department of Clinical Medicine, University of Copenhagen, 2200 Copenhagen, Denmark
* Correspondence: mads.lawaetz@regionh.dk
† Before this article was published, Kirstine Kim Schmidt Karnov sadly passed away. Our thoughts are with her family.

Abstract: No clinically approved tumor-specific imaging agents for head and neck cancer are currently available. The identification of biomarkers with a high and homogenous expression in tumor tissue and minimal expression in normal tissue is essential for the development of new molecular imaging targets in head and neck cancer. We investigated the expression of nine imaging targets in both primary tumor and matched metastatic tissue of 41 patients with oral squamous cell carcinoma (OSCC) to assess their potential as targets for molecular imaging. The intensity, proportion, and homogeneity in the tumor and the reaction in neighboring non-cancerous tissue was scored. The intensity and proportion were multiplied to obtain a total immunohistochemical (IHC) score ranging from 0–12. The mean intensity in the tumor tissue and normal epithelium were compared. The expression rate was high for the urokinase-type plasminogen activator receptor (uPAR) (97%), integrin αvβ6 (97%), and tissue factor (86%) with a median total immunostaining score (interquartile range) for primary tumors of 6 (6–9), 12 (12–12), and 6 (2.5–7.5), respectively. For the uPAR and tissue factor, the mean staining intensity score was significantly higher in tumors compared to normal epithelium. The uPAR, integrin αvβ6, and tissue factor are promising imaging targets for OSCC primary tumors, lymph node metastases, and recurrences.

Keywords: oral squamous cell carcinoma; lymph node metastases; molecular imaging; immunohistochemistry; urokinase-type plasminogen activator receptor; tissue factor; integrin αvβ6

1. Introduction

Despite advances in diagnostic techniques and postoperative treatment, poor survival and high recurrence rate remain for patients with oral squamous cell carcinoma (OSCC) [1]. The primary curative treatment is surgery, where the adequate resection margins (>5 mm) are one of the most important prognosticators [2,3]. Achieving radical resection margins is challenging when the tumor is surrounded by multiple functionally and aesthetically critical structures and the border between the tumor and normal tissue is not clearly delineated. This is reflected in a positive margin rate of 12–30% for OSCC, one of the highest rates among all solid tumors [2,4,5]. Additionally, the detection and removal

of regional lymph node metastases by neck dissection is a challenge due to a significant risk of occult microscopic disease that is not detected by conventional preoperative imaging [6]. Currently, there are no established real-time intraoperative imaging techniques for distinguishing healthy tissue from tumor tissue in OSCC. The surgeons rely on preoperative imaging and intraoperative visual and tactile information. Intraoperative margin assessment may be performed by use of frozen section microscopy, which is time-consuming and prone to sampling and interpretation errors [7].

Molecular imaging is a rapidly emerging field for the diagnosis and treatment of cancer, particularly head and neck cancer, in which several targets and modalities have been studied and are under development [8]. Due to advancements in imaging hardware and fluorophore biochemistry, targeted fluorescence guided surgery (FGS) is one of the most promising real-time intraoperative imaging techniques. Especially fluorophores with excitation and emission in the near-infrared (NIR) spectrum, such as indocyanine green (ICG) and IRDye800CW, have been investigated due to a relatively high penetration depth compared to other wavelengths [9,10]. Despite intensive research, no clinically approved tumor-specific imaging agents for head and neck cancer surgery are currently available [11]. The identification of biomarkers with a high and homogenous expression in tumor tissue and minimal expression in normal tissue is essential for the development of new molecular imaging targets in head and neck cancer.

The vascular endothelial growth factor receptor 1 and 2 (VEGFR1 and VEGFR2) play important roles in tumor angiogenesis [12]. A high expression of both receptors has been reported in OSCC [13] and several studies have investigated these receptors as targets for molecular imaging in different cancers [14]. Integrin $\alpha v\beta 3$ is another receptor expressed by tumor cells that plays an important role in tumor angiogenesis [15] and molecular imaging, and has been explored in several different cancers with promising results [16]. Integrin $\alpha v\beta 6$ is a member of the same family that has been more thoroughly studied [17–19]. Integrin $\alpha v\beta 6$ is important for cell migration as it facilitates cell-to-cell and cell-to-extracellular matrix adhesion. In OSCC, integrin $\alpha v\beta 6$ has been found to be upregulated, especially at the invasive margin [20], and involved in different hallmarks of cancer including epithelial to mesenchymal transition [21], invasion, and migration [20,22]. The epithelial cell adhesion molecule (EpCAM), like integrins, is a cell adhesion receptor implicated in metastasis. It has been identified as being overexpressed in several malignancies, including OSCC [23], and several studies have already investigated the use of both fluorescence and radionuclide probes [24,25]. Cathepsin E and Poly(ADP-ribose)polymerase-1 (PARP-1) are both intracellular enzymes that have been shown to be overexpressed in a variety of malignancies [26,27]. PARP-1 has been examined as a PET-imaging target and a target for fluorescence imaging in OSCC [28–30], whereas Cathepsin E expression in OSCC has not been previously described. However, a fluorescence probe has been developed for Cathepsin E and tested in vivo [31]. The urokinase-type plasminogen activator receptor (uPAR) is a GPI-anchored cell membrane receptor that turns plasminogen into plasmin at the cell surface, thus degrading the extracellular matrix [32]. uPAR has been found to be upregulated in most solid cancers where it facilitates cell invasion and metastasis, and a high expression has been associated with poor prognosis and metastases [33]. The tissue factor, a transmembrane glycoprotein that stimulates the extrinsic coagulation pathway, is thought to have a significant role in tumor progression [34]. An overexpression of the tissue factor has been reported in several malignancies and is related with poor clinical outcomes [35,36].

Our aim was to investigate the immunohistochemical (IHC) expression of the above mentioned, nine interesting imaging targets in both primary tumor and matched metastatic tissue from OSCC to assess their potential as targets for molecular imaging. For a subgroup, the tissue from recurrent disease was evaluated.

2. Results

2.1. Patient Characteristics

In this population of 41 patients with OSCC, the median age at diagnosis was 58 years (range 23–81 years), and 26 (63%) of the patients were male (Table 1). The majority of tumors (73%) were moderately differentiated, and tumors were located in the floor of mouth (56%) and oral tongue (44%). All pathologic T-stages were represented. The majority of tumors were in stage T1 or T2 at the time of surgery and 38 patients (93%) had histological confirmed lymph node metastases. Surgery aiming radicality was the first line of treatment for all patients.

Table 1. Clinicopathological characteristics of 41 patients with oral squamous cell carcinoma.

Characteristics	n (%) or Median (Range)
Age, years	58, (23–81)
Gender	
Male	26 (63%)
Female	15 (37%)
Location	
Tongue	18 (44%)
Floor of mouth	23 (56%)
Tumor differentiation	
Low	5 (12%)
Moderate	30 (73%)
High	6 (15%)
Pathologic T-stage	
T1	11(27%)
T2	17 (42%)
T3	5 (12%)
T4	5 (12%)
Missing	3 (7%)
Pathologic N-stage	
N0	3 (7%)
N+	38 (93%)

2.2. Immunohistochemical Staining

Primary tumor tissue was obtained from all 41 patients. In a number of patients, there was insufficient remaining tumor tissue to perform IHC staining for all nine targets, and normal mucosa was not present or only present in some sections. Formalin-fixed, paraffin-embedded (FFPE) blocks containing metastatic tissue were available for 28 patients, while local recurrence tissue was obtained from eight patients. A representative image for each target's immunohistochemical staining is shown in Figure 1 and the three most promising biomarkers in matched tumor samples from the same patient is shown in Figure 2. The intensity, proportion, and total immune staining score for all targets are shown in Table 2. An overview of the final expression category in primary tumors and metastases of all biomarkers is illustrated in Figures 3 and 4, respectively.

Table 2. Median and interquartile ranges of intensity, proportion, and total immune staining scores for each target in primary tumor, lymph node metastases, and tissue from local recurrence.

Target	Primary Tumor				Lymph Node Metastases				Local Recurrence				Normal Epithelium	
	n	Intensity score (IQR)	Proportion (IQR)	TIS-score (IQR)	n	Intensity score (IQR)	Proportion (IQR)	TIS-score (IQR)	n	Intensity score (IQR)	Proportion (IQR)	TIS-score (IQR)	n	Intensity score (IQR)
Integrin $\alpha v\beta 6$	40	3 (3-3)	4(4-4)	12(12-12)	28	3(3-3)	4(4-4)	12(9.75-12)	8	3(3-3)	4(4-4)	12(12-12)	47	3(3-3)
Tissue factor	41	3(2-3)	2(1-3)	6(2,5-7.5)	28	2(1-3)	1(1-2)	2(1-5.5)	8	2.5(0-3)	1.5(0-2)	4(0-6)	47	1(1-1)
PARP1	35	2(2-3)	3(3-4)	6(4-9)	24	2(2-3)	3(3-3)	6(6-9)	7	2(2-2)	3(3-4)	6(4-8)	39	2(1-2)
uPAR	34	3(2.75-3)	2(2-3)	6(6-9)	23	3(2-3)	2(2-3)	6(4-6)	6	3(2.75-3)	2.5 (2-3,25)	6(6-9.75)	37	0(0-0)
VEGFR1	35	2(2-2)	4(3-4)	8(6-8)	24	2(2-2)	4(3.25-4)	8(6.5-8)	7	2(1-2)	4(3-4)	8(3-8)	40	1.5(1-2)
EpCAM	34	0.5(0-2)	0.5(0-2)	0.5(0-2.5)	24	1.5(0-3)	1(0-1)	1.5(0-3)	7	1(0-3)	1(0-2)	1(0-6)	34	0(0-0)
VEGFR2	35	1(1-2)	1(1-2)	2(1-4)	24	1(1-2)	2(1-2)	2(1-4)	7	1(0-1)	2(0-2)	2(0-2)	39	0(0-1)
Cathepsin E	35	0(0-0)	0(0-0)	0(0-0)	23	0(0-0)	0(0-0)	0(0-0)	7	0(0-0)	0(0-0)	0(0-0)	40	0 (0-0,5)
Integrin $\alpha v\beta 3$	36	0(0-0)	0(0-0)	0(0-0)	27	0(0-0)	0(0-0)	0(0-0)	8	0(0-0)	0(0-0)	0(0-0)	44	0(0-0)
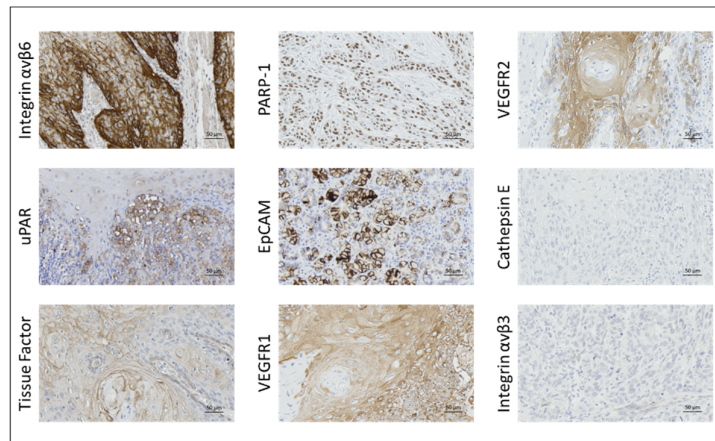
Figure 1. Expression of integrin $\alpha v\beta 6$, tissue factor, PARP-1, uPAR, VEGFR1, EpCAM, VEGFR2, Cathepsin E and integrin $\alpha v\beta 3$ in primary tumor tissue of OSCC.
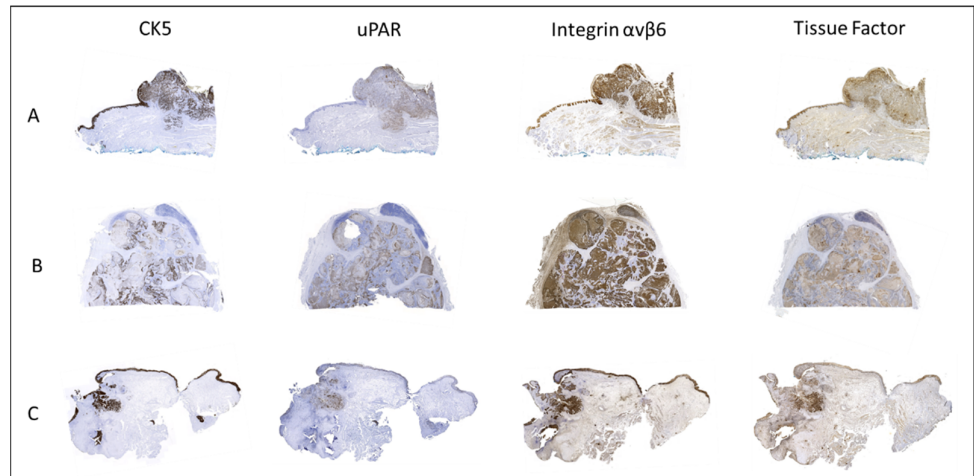
Figure 2. Expression of CK5 (for visualization of tumor localization), uPAR, integrin αvβ6 and tissue factor in (**A**) primary tumor, (**B**) lymph node metastases, and (**C**) local recurrence.
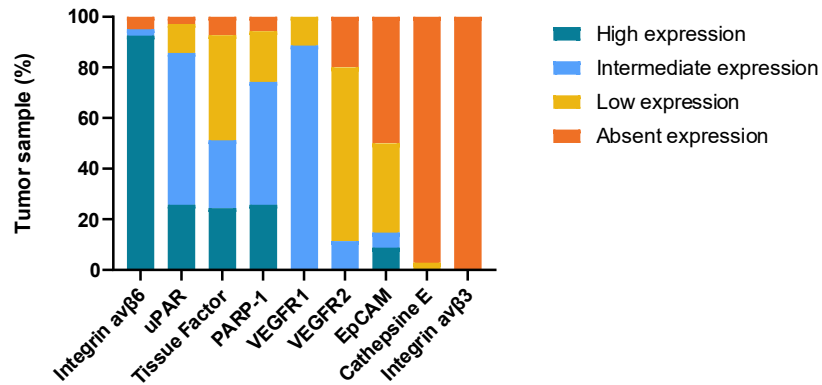
Figure 3. Expression of imaging targets in OSCC primary tumors.
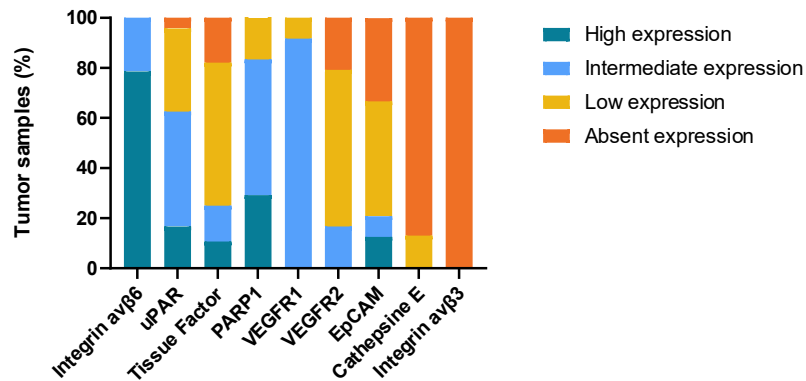
Figure 4. Expression of imaging targets in OSCC lymph node metastases.

2.2.1. Integrin αvβ6

Integrin αvβ6 expression was seen in nearly all tumor samples (97%) with strong membrane and cytoplasmic staining in most tumor cells. There was a distinct demarcation between tumor cells and immune cells in lamina propria and surrounding tissue in

submucosa. The staining was homogenous in 80% of all tumor samples (Table 3). The median staining scores (interquartile range) for primary tumor, lymph node metastases, and local tumor recurrence were 12 (12–12), 12 (9.75–12), and 12 (12–12), respectively. Except for a weak staining of muscle cells and a moderate staining of salivary gland ducts, no other normal cells in the subepithelial layers were positive. Integrin $\alpha v\beta 6$ was also expressed in normal epithelium.

2.2.2. uPAR

The overall expression rate was 97% with highly tumor-specific staining, which was rated as homogeneous in 51% of the samples. uPAR was expressed in 23/24 metastases (96%). Both membrane and cytoplasmic staining were found in tumor cells. The total immune staining scores for primary tumor cells, lymph node metastases, and local tumor recurrence tissue were 6 (6–9), 6 (4–8), and 6 (6–9.75), respectively. Normal epithelium exhibited no staining, except for in four cases where weak epithelial staining was seen. In one case, moderate staining of a lichen planus lesion was observed in the periphery of the tumor. There was a clear contrast between tumor and surrounding tissue at the deep tumor margin. Weak to moderate staining was observed in granulocytes.

2.2.3. Tissue Factor

The overall expression rate of tissue factor in tumor tissue was high (86%), but only with a homogenous pattern in 3% of tumor samples. In half of the primary tumor samples, tissue factor showed moderate to intense expression. In lymph node metastases, expression was mainly weak and moderate. Staining scores for primary tumor cells, lymph node metastases, and local recurrence tumor tissue were 6 (2.5–7.5), 2 (1–5.5), and 4 (0–6), respectively. Normal epithelium expressed tissue factor in approximately 80% of the samples, although the staining in this compartment was mostly weak. Salivary duct and acini cells also showed a weak expression of tissue factor.

2.2.4. PARP-1

A high overall expression rate was seen for PARP-1 (97%), with positive staining of tumor nuclei, albeit heterogeneously. For primary tumor cells, lymph node metastases, and local recurrence tumor tissue, the staining scores were 6 (4–9), 6 (6–9), and 6 (4–8), respectively. Nevertheless, the staining was not very tumor-specific, as several normal cells were also stained. Lymphocytes, endothelium, muscle tissues, nerve fibers, salivary gland tissues, plasma cells, and normal epithelium exhibited variable nuclei staining.

2.2.5. VEGFR1

All tumors were positive for VEGFR1, but the staining was not tumor-specific and contrasted poorly with the normal stroma and epithelium. The VEGFR1 staining scores for primary tumor, lymph node metastases, and recurrent tumor tissue were 8 (6–8), 8 (6.5–8), and 8 (3–6), respectively. Macrophages, plasma cells, nerve fibers, endothelium, muscle tissues, and salivary gland tissues had expression of VEGFR.

2.2.6. EpCAM

EpCAM was expressed in 57% of all tumor samples, but only 3% exhibited a homogenous pattern. In tumor cells, membrane and cytoplasmic stains were seen. The intensity of EpCAM positive tumors varied but was generally weak to moderate. Total IHC scores were 0.5 (0–2.5), 1.5 (0–3), and 1 (0–6) for primary tumor cells, lymph node metastases, and local recurrence tumor tissue, respectively. Rarely were EpCAM-positive macrophages and plasma cells observed. Normal epithelium exhibited no staining.

2.2.7. VEGFR2

The overall expression rate of VEGFR2 was 79%, with no tumors displaying homogenous expression pattern. The VEGFR2 antibody staining was present in the cytoplasm of the tumor cells, although it was mainly weak. The staining scores for primary tumor tissue, lymph node metastases, and local recurrence were 2 (1–4), 2 (1–4), and 2 (0–2), respectively. Moderate to weak expression was also seen in normal oral squamous epithelium in 29% of samples. No expression was seen in the stroma surrounding tumor.

2.2.8. Cathepsin E and Integrin $\alpha v \beta 3$

Only one primary tumor and three lymph node metastases showed Cathepsin E expression. No expression of integrin $\alpha v \beta 3$ was observed in primary tumors, metastases, or tissue from local recurrence. The staining scores for both biomarkers for primary tumor cells, lymph node metastases, and local recurrence tumor tissue were 0 (0–0), 0 (0–0), and 0 (0–0).

2.3. Intensity of Staining in Normal Oral Mucosal Epithelium vs. Tumor Tissue

The mean staining intensity score between normal epithelium and tumor tissue was compared for all samples where both components were present. The staining intensity was significantly higher in tumors compared to normal epithelium in uPAR ($p < 0.001$, n = 37), VEGFR2 ($p = 0.002$, n = 41), VEGFR1 ($p = 0.001$, n= 41), PARP-1 ($p = 0.003$, n= 40), and tissue factor ($p < 0.001$, n = 47). No difference in staining intensity between tumor tissue and normal epithelium was seen for integrin $\alpha v \beta 6$ ($p = 0.380$, n= 47) or EPCAM ($p = 0.130$, n= 39).

2.4. Biomarker Expression in Primary Tumor Compared to Lymph Node Metastases and Tissue from Local Recurrence (T-Site)

We examined the correlation between total immune staining scores in primary tumors and lymph node metastases for each target in cases where tissue from both locations were available. We identified 28 primary cancers with accessible tissue from lymph node metastasis. All targets with tumor staining exhibited a positive Spearman rank correlation value. However, only uPAR (spearman correlation = 0.554, $p = 0.014$), tissue factor (spearman correlation = 0.615, $p= 0.001$), and VEGFR2 (Spearman correlation = 0.765, $p < 0.001$) had a significant positive correlation between total immune staining scores in primary tumor and lymph node metastases. Due to small numbers of cases with recurrence, no significant correlation was found between the total immune staining scores in primary tumors and tumor tissue from local recurrence, but a tendency toward positive correlation was seen for uPAR (spearman correlation = 0.395; $p= 0.510$), EpCAM (spearman correlation = 0.111, $p = 0.834$), and PARP-1 (spearman correlation = 0.064, $p = 0.905$)

Table 3. Overview of the expression pattern for all nine included targets.

Target	Tumor-Specific	Homogenous Expression in Tumor Compartment	Expression Rate Primary Tumor	Expression Rate Lymph Node Metastasis	Superficial Margin Contrast Tumor vs. Epithelium	Profound Margin Contrast Tumor vs. Normal Cells
Integrin $\alpha v \beta 6$	Partly	80%	95%	100%	No	Yes
Tissue factor	Yes	3%	93%	80%	Yes	Yes
PARP1	No	0%	94%	100%	Yes	No
uPAR	Yes	51%	97%	96%	Yes	Yes
VEGFR1	No	5%	100%	100%	Yes	No
EpCAM	No	3%	50%	66%	No	No
VEGFR2	No	0%	80%	81%	Yes	No
Cathepsin E	NA	0%	3%	13%	NA	NA
Integrin $\alpha v \beta 3$	NA	NA	NA	NA	NA	NA

3. Discussion

In this study, we have evaluated nine potential molecular imaging targets from 41 OSCC patients with tissue samples from the primary tumor, lymph node metastases, and local recurrence. This is, to the best of our knowledge, the first study to investigate and compare multiple potential targets in both primary OSCC tumors and their metastases. Based on immunohistochemical expression levels and expression patterns in the tumor, normal epithelium, and surrounding tissue, it was revealed that the uPAR, integrin $\alpha v\beta 6$, and tissue factor represent attractive molecular imaging targets in OSCC due to a high overall expression rate of 97%, 97%, and 86%, respectively. The high expression rates of uPAR (96%) and integrin $\alpha v\beta 6$ (100%) in lymph node metastases indicate a potential in FGS for detecting lymph node metastases during sentinel lymph node biopsy or neck dissection, which could potentially spare healthy nodes.

We found a highly tumor-specific uPAR expression in most tumor samples (97%), with a moderate to intense staining in both primary tumors and metastases. Our results are in accordance with previous immunohistochemical studies that have also found a high tumor-specific expression of uPAR in OSCC, with an absence of staining in the surrounding normal squamous epithelium and weak expression in tumor-associated inflammatory cells (macrophages, neutrophils, and fibroblasts), with a sharp demarcation at the deep tumor margin [37–39]. Interestingly, our current study demonstrated uPAR expression in 96% of metastasis, which indicates that combined targeted strategies against the tumor as well as metastatic disease seem possible. Different molecular imaging modalities have been explored for uPAR. In clinical trials, uPAR-targeted PET imaging using a peptide-based tracer has been studied for several cancers including OSCC, where a prognostic value was demonstrated [40–43]. No studies have yet investigated the diagnostic potential of uPAR-targeted PET imaging in OSCC, but a Phase II clinical trial is currently underway (NCT02960724). Few clinical studies have been conducted on FGS using uPAR-directed probes. In a cell-line-based xenograph proof-of-concept study conducted at our institution, it was shown that uPAR-targeted optical near-infrared fluorescence imaging using ICG conjugated to AE-105 can be used to identify small lymph node metastases during surgery [44]. Boonstra et al. also investigated uPAR-targeted FGS in cell-line-based xenograph models with an antibody-based tracer (hybrid ATN 658) conjugated to a fluorophore (ZW800-1), and showed that this modality could also identify primary tumors and lymph node metastases [45]. Clinical trials investigating uPAR-targeted FGS are ongoing in patients with oral cancer, lung cancer, and glioblastoma (EudraCT no. 2022-001361-12, 2021-004389-37 and 2020-003089-38).

The tissue factor also demonstrated a tumor-specific expression, but at a lower rate (86%) and with a more heterogeneous pattern than uPAR. The expression of the tissue factor in lymph node metastases was less compared to the primary tumor tissue. These results are consistent with similar immunohistochemistry studies on primary tumor tissue from oral and oropharyngeal squamous cell carcinoma, which found tissue factor expression rates of 58% and 76%, respectively [37,46]. As, an imaging target tissue factor has been poorly investigated in OSCC, but the potential in several other cancers has been explored. In preclinical studies, the tissue factor has been investigated as a target for FGS, SPECT, and PET using tissue factor-specific monoclonal antibodies in both anaplastic thyroid cancer, glioblastoma, and pancreatic cancer xenografts with promising effect [47–50]. In 2021, an antibody drug (tisotumab vedotin)-targeting tissue factor was approved by FDA for treatment of metastatic cervical cancer [51]. Subsequently the tissue factor-targeted PET-imaging with a protein (FVIIa) labeled with ^{18}F was successfully tested first in a human study and proposed as a future diagnostic tool prior to tissue factor-targeted treatment [52]. The high expression of the tissue factor in OSCC and the recent development of tissue factor-targeted tracers in other solid cancers makes it a promising imaging agent in OSCC.

Integrin $\alpha v\beta 6$ was also highly expressed in our study, with a clear contrast at the deep tumor margin. However, a high integrin $\alpha v\beta 6$ expression was also seen in normal

squamous cell epithelium without a significant difference in the intensity score between a tumor and normal epithelium. Our findings suggest that molecular imaging drugs targeting integrin $\alpha v\beta 6$ may provide a distinct contrast at the deep margin but less at the superficial margins. These results are in line with those obtained by Baart et al., who investigated the immunohistochemical expression of integrin $\alpha v\beta 6$ in both OSCC and cutaneous squamous cell carcinoma of the head and neck [38]. They also proposed integrin $\alpha v\beta 6$ as a target for FGS in OSCC, especially due to the clear discrimination at the deep margin and compared to EGFR, they found less staining of the normal epithelium. Integrin $\alpha v\beta 6$ has been studied as a PET-imaging target in different cancers. In 2019, Hausner et al. successfully performed a first in human studies by exploring PET/CT with a radiolabeled integrin $\alpha v\beta 6$-binding peptide in patients with metastatic colon, breast, and pancreas cancer [18]. Later, Quigley et al. tested a Ga-68-labeled peptide (Ga-68-Trivehexin) for human PET/CT imaging of head, neck, and pancreatic cancer, with results showing a high tumor-specific uptake and no uptake in tumor-associated inflammation [19]. Integrin $\alpha v\beta 6$ has, to our knowledge, not been tested as a target for fluorescent imaging in OSCC patients. However, Ilyia et al. showed imaging potential in in vitro head and neck cancer models with quantum dots conjugated to an integrin $\alpha v\beta 6$-specific peptide [53]. A human trial by de Valk et al. has studied integrin $\alpha v\beta 6$-targeted near-infrared fluorescent peptides (cRGD-ZW800-1) in 12 patients with colon carcinoma and was able to show cancer-specific imaging in both open and laparoscopic surgery [54]. Studies investigating integrin $\alpha v\beta 6$ as a target for fluorescent imaging in OSCC have not yet been published, but a clinical trial with cRGD-ZW800-1 (NCT 04191460) is planned to investigate whether this modality can improve the rate of adequate surgical resection margins in OSCC.

PARP-1 showed mostly moderate and moderate to high expression levels in the tumor nuclei, but it appears less suitable as an imaging target compared to uPAR, $\alpha v\beta 6$, and tissue factor, owing to the non-specific staining of several different cell-types in the lamina propria and submucosa as well as the staining of normal squamous epithelium. Even though some expressions of PARP-1 are present in normal tissues, this biomarker might not be excluded as a target for molecular imaging, because the density of the nuclei in tumor cells are higher compared to normal tissues [28]. Kossatz et al. recently investigated a topically applied PARP-1-specific fluorescence agent for the use of early diagnosis of OSCC in a Phase 1 study with 12 patients, where the fluorescence signal showed a tumor to normal ratio > 3 [30]. However, the topical approach is probably confined to early stage disease or screening of mucosal lesions, as the penetration depth is limited (300 μm in the trial by Kossatz et al.). VEGFR1 and VEGFR2 did not appear promising for imaging purposes in our study, as their expression was limited, and the tumor specificity was low. No studies have yet examined the molecular imaging of these targets in OSCC, but different angiogenesis inhibitors for the treatment of head and neck squamous cell carcinoma have been thoroughly investigated, with bevacizumab being the most promising [55].

This study has some limitations. First, a biomarkers appropriateness as an imaging target is determined by several factors in addition to its overexpression. The target selection criteria system has been suggested as a tool to identify potential imaging targets and consists of seven different criterions. However, several of these are either difficult to measure (tumor to normal ratio greater than 10) or questionable (internalization of the tracer) [56]. Second, immunohistochemistry has several inherited limitations, including the selection of an antibody clone, which can affect the intensity and proportion of the stained tumor tissue substantially. In addition, both a manual and semi-quantitative scoring method were used, and several different scoring systems exists. This is a subjective estimate and interobserver variability is unavoidable. Third, the small sample size of tissues from lymph node metastases and tissues from local tumor recurrence compared to primary tumors limits the interpretation of the results. This study does not provide new diagnostic methods in pathology to diagnose OSCC earlier than with current methods, but rather focuses on the potential future targets for molecular imaging.

4. Materials and Methods

4.1. Patient and Tissue Selection

From an existing, well-defined database consisting of patients diagnosed with OSCC between 2000–2011 and surgically treated at the department of Otolaryngology, Head and Neck Surgery and Audiology at Rigshospitalet (Copenhagen, Denmark), we randomly selected 41 patients. Microscopy slides were retrieved from the archives of the Department of Pathology and one FFPE tissue block containing both tumor tissue and normal epithelium were selected from each patient for following IHC staining. Of the 41 patients, 28 patients also had available tissue from lymph node metastases and 8 patients from recurrent disease. Clinicopathological data were obtained from medical and pathology reports. The 7th edition of the TNM Union for International Cancer Control (UICC) staging system was used.

4.2. Selection of Imaging Targets

Through literature search, we identified nine targets with previously described overexpression in several cancers, including head and neck, and for which there is a potential for rapid translation into clinical settings due to earlier research/probe development. The following biomarkers were selected: integrin αvβ6, tissue factor, poly(ADP-ribose) polymerase 1 (PARP-1), urokinase plasminogen activator receptor (uPAR), vascular endothelial growth factor receptor 1 (VEGFR1), epithelial cell adhesion molecule (EpCAM), vascular endothelial growth factor receptor 2 (VEGFR2), Cathepsin E, and integrin αvβ3. Immunohistochemical staining for cytokeratin 5 (CK5) was used to visualize tumor location. Despite its great imaging potential, epidermal growth factor receptor (EGFR) was not included as it is very well characterized in OSCC and clinical trials with targeted tracers are currently being performed (NCT03134846 and NCT03733210).

4.3. Immunohistochemistry

The expression of all targets was determined for both the primary tumor, metastasis, and tissue from local recurrence. Tumor tissue had been fixated in 10% formalin solution at room temperature for 24 h and then embedded in paraffin at the time of collection. FFPE blocks were stored at room temperature. Tissue sections of 4 μm were cut and IHC staining with integrin αvβ3, integrin αvβ6, tissue factor, and EPCAM were performed using a semi-automated autostainer, Ventana Benchmark Ultra (Roche Diagnostics). Manual staining was performed for the following biomarkers: Cathepsin E, PARP-1, uPAR, VEGFR1, and VEGFR2. Antibodies, reagents, and methods used for IHC analysis are listed in Appendix A. Briefly, the slides were incubated at 60 °C for 60 min before being deparaffinized in HistoClear solution, rehydrated in graded ethanol, and submerged in water. Different antigen retrieval methods were used depending on the target. All antibodies were used at optimal dilutions, which were determined using positive and negative control staining (data not shown). Secondary staining with HRP-conjugated antibody was performed by incubation for 30–40 min. The reaction was visualized with Envision DAB+ for the manual staining and with DAB+ chromogen solution for the autostainer. Digital pictures for Figure 4 were obtained using Zeiss Axioscan with 10 x zoom.

4.4. Assessment of Immunohistochemical Staining

Two specialized head and neck pathologists (GL and AF) reviewed and scored all samples blinded to clinical data. In the event of a disagreement, individual slides were examined together to obtain a consensus score. Each sample was assessed according to highest staining intensity in tumor compartment, proportion of stained malignant tumor tissue in the total tumor area, expression pattern in tumor tissue (homogenous or heterogeneous), and intensity in normal epithelium. Proportion and intensity scores were generated using a point system: 0% (0), 1–10% (1), 11–50% (2), 51–75% (3), and 76–100% (4), and none (0), weak (1), medium (2), and strong (3), respectively. The staining intensity of

normal epithelium around the tumor tissue was scored in the same way. The proportion and intensity scores for tumor tissue were multiplied to provide a single combined score and a total immune staining score (TIS), which is similar to previous studies [38,57–59]. This resulted in a score ranging from 0 to 12, which was divided into four final expression categories: 0 = absent; 1–5 = low; 6–8 = intermediate; and 9–12 = high expression. For each target, the proportion of patients categorized as low, intermediate, and high expression was calculated. The expression rate was calculated as the proportion of samples with low, intermediate, and high expression.

4.5. Statistical Analysis

Statistical analysis was performed using IBM SPSS statistics 25.0. The median and interquartile range of the staining score were calculated for primary tumor, lymph node metastases, and recurrence. Wilcoxon signed-rank test was used to compare the intensity of immunohistochemistry staining of tumor to normal oral mucosal epithelium. Correlation between total immune staining scores in primary tumor and in lymph node metastases was tested using Spearman's correlation test. Results were considered statistically significant at the level of $p < 0.05$.

Bar charts were made using GraphPad Prism version 9.3 for PC, GraphPad Software, La Jolla, California, USA.

5. Conclusions

In conclusion, the uPAR, integrin $\alpha v \beta 6$, and tissue factor are promising imaging targets for OSCC. Molecular imaging based on a single target that could be used for both pre- and intraoperative imaging of a primary tumor, lymph node metastases, and in cases, of recurrence would be a powerful tool for the diagnosis and treatment of OSCC.

Appendix A

Table A1. Primary antibodies used for immunohistochemistry.

Target	Source	Catalog Number	Species	Monoclonal/Polyclonal	Dilution	Staining Method
Cytokeratin 5	Novocastra	CK5-L-CE	Mouse	Monoclonal	No dilution	Automatic, VENTANA BenchMark IHC
Integrin $\alpha v \beta 3$	R&D Systems	MAB3050	Mouse	Monoclonal	1:500	Automatic, VENTANA BenchMark IHC

Integrin αvβ6	ABCAM	ab181551	Mouse	Monoclonal	1:500	Automatic, VENTANA BenchMark IHC
Tissue Factor	Sekisui	4509	Mouse	Monoclonal	1:50	Automatic, VENTANA BenchMark IHC
EPCAM	Cell Marque	5435676001	Mouse	Monoclonal	No dilution	Automatic, VENTANA BenchMark IHC
Cathepsin E	Abcam	Ab36996	Rabbit	Polyclonal	1:2000	Manual
PARP1	Abcam	Ab32138	Rabbit	Monoclonal	1:25	Manual
uPAR	Genetex	GTX100467	Mouse	Monoclonal	1:500	Manual
VEGFR1	Abcam	Ab32152	Rabbit	Monoclonal	1:75	Manual
VEGFR2	Cell Signaling	55B11	Rabbit	Monoclonal	1:300	Manual

References

1. Leoncini, E.; Vukovic, V.; Cadoni, G.; Giraldi, L.; Pastorino, R.; Arzani, D.; Petrelli, L.; Wünsch-Filho, V.; Toporcov, T.N.; Moyses, R.A.; et al. Tumour Stage and Gender Predict Recurrence and Second Primary Malignancies in Head and Neck Cancer: A Multicentre Study within the INHANCE Consortium. *Eur. J. Epidemiol.* **2018**, *33*, 1205. https://doi.org/10.1007/S10654-018-0409-5.
2. Orosco, R.K.; Tapia, V.J.; Califano, J.A.; Clary, B.; Cohen, E.E.W.; Kane, C.; Lippman, S.M.; Messer, K.; Molinolo, A.; Murphy, J.D.; et al. Positive Surgical Margins in the 10 Most Common Solid Cancers. *Sci. Rep.* **2018**, *8*, 5686. https://doi.org/10.1038/s41598-018-23403-5.
3. Eldeeb, H.; Macmillan, C.; Elwell, C.; Hammod, A. The Effect of the Surgical Margins on the Outcome of Patients with Head and Neck Squamous Cell Carcinoma: Single Institution Experience. *Cancer Biol. Med.* **2012**, *9*, 29–33. https://doi.org/10.3969/j.issn.2095-3941.2012.01.005.
4. Binahmed, A.; Nason, R.W.; Abdoh, A.A. The Clinical Significance of the Positive Surgical Margin in Oral Cancer. *Oral Oncol.* **2007**, *43*, 780–784. https://doi.org/10.1016/j.oraloncology.2006.10.001.
5. Mcmahon, J.; O'brien, C.J.; Pathak, I.; Hamill, R.; Mcneil, E.; Hammersley, N.; Gardiner, S.; Junor, E. Influence of Condition of Surgical Margins on Local Recurrence and Disease-Specific Survival in Oral and Oropharyngeal Cancer. *Br. J. Oral Maxillofac. Surg.* **2003**, *41*, 224–231. https://doi.org/10.1016/S0266-4356(03)00119-0.
6. Ahmed, M.U.; Khawar, A.; Ahmed, J.; Ajmal, M.; Bangash, W.K.; Akhter, M.R. Occult Metastasis in Carcinoma of Oral Cavity. *J. Coll. Physicians Surg. Pak.* **2007**, *17*, 313–315, doi:06.2007/JCPSP.313315.
7. Du, E.; Ow, T.J.; Lo, Y.T.; Gersten, A.; Schiff, B.A.; Tassler, A.B.; Smith, R.V. Refining the Utility and Role of Frozen Section in Head and Neck Squamous Cell Carcinoma Resection. *Laryngoscope* **2016**, *126*, 1768–1775. https://doi.org/10.1002/LARY.25899.
8. Wu, J.; Yuan, Y.; Tao, X.F.; Lyu, P. Targeted Molecular Imaging of Head and Neck Squamous Cell Carcinoma: A Window into Precision Medicine. *Chin. Med. J. (Engl).* **2020**, *133*, 1325. https://doi.org/10.1097/CM9.0000000000000751.
9. Zhang, R.R.; Schroeder, A.B.; Grudzinski, J.J.; Rosenthal, E.L.; Warram, J.M.; Pinchuk, A.N.; Eliceiri, K.W.; Kuo, J.S.; Weichert, J.P. Beyond the Margins: Real-Time Detection of Cancer Using Targeted Fluorophores. *Nat. Rev. Clin. Oncol.* **2017**, *14*, 347. https://doi.org/10.1038/NRCLINONC.2016.212.
10. Van Schaik, J.E.; Halmos, G.B.; Witjes, M.J.H.; Plaat, B.E.C. An Overview of the Current Clinical Status of Optical Imaging in Head and Neck Cancer with a Focus on Narrow Band Imaging and Fluorescence Optical Imaging. *Oral Oncol.* **2021**, *121*, 105504. https://doi.org/10.1016/j.oraloncology.2021.105504.
11. Crawford, K.L.; Pacheco, F.V.; Lee, Y.J.; Hom, M.; Rosenthal, E.L.; Nguyen, Q.T.; Orosco, R.K. A Scoping Review of Ongoing Fluorescence-Guided Surgery Clinical Trials in Otolaryngology. *Laryngoscope* **2022**, *132*, 36–44. https://doi.org/10.1002/LARY.29891.
12. Johnstone, S.; Logan, R.M. The Role of Vascular Endothelial Growth Factor (VEGF) in Oral Dysplasia and Oral Squamous Cell Carcinoma.. https://doi.org/10.1016/j.oraloncology.2005.06.020.
13. Stîngă, A.C.; Mărgăritescu, O.; Stîngă, A.S.; Pirici, D.; Ciurea, R.; Bunget, A.; Cruce, M. VEGFR1 and VEGFR2 Immunohistochemical Expression in Oral Squamous Cell Carcinoma: A Morphometric Study. *Rom. J. Morphol. Embryol.* **2011**, *52*, 1269–1275.
14. Masłowska, K.; Halik, P.K.; Tymecka, D.; Misicka, A.; Gniazdowska, E. The Role of VEGF Receptors as Molecular Target in Nuclear Medicine for Cancer Diagnosis and Combination Therapy. *Cancers* **2021**, *13*, 1072. https://doi.org/10.3390/CANCERS13051072.
15. Brooks, P.C.; Clark, R.A.F.; Cheresh, D.A. Requirement of Vascular Integrin Avβ3 for Angiogenesis. *Science* **1994**, *264*, 569–571. https://doi.org/10.1126/science.7512751.

16. Beer, A.J.; Schwaiger, M. Imaging of Integrin Avβ3 Expression. *Cancer Metastasis Rev.* **2008**, *27*, 631–644. https://doi.org/10.1007/S10555-008-9158-3/FIGURES/4.

17. Niu, J.; Li, Z. The Roles of Integrin Avβ6 in Cancer. *Cancer Lett.* **2017**, *403*, 128–137. https://doi.org/10.1016/j.canlet.2017.06.012.

18. Hausner, S.H.; Bold, R.J.; Cheuy, L.Y.; Chew, H.K.; Daly, M.E.; Davis, R.A.; Foster, C.C.; Kim, E.J.; Sutcliffe, J.L. Preclinical Development and First-in-Human Imaging of the Integrin a v b 6 with [18 F]a v b 6 -Binding Peptide in Metastatic Carcinoma. *Clin. Cancer Res.* **2019**, *25*, 1206–1215. https://doi.org/10.1158/1078-0432.CCR-18-2665.

19. Quigley, N.G.; Steiger, K.; Hoberück, S.; Czech, N.; Zierke, M.A.; Kossatz, S.; Pretze, M.; Richter, F.; Weichert, W.; Pox, C.; et al. PET/CT Imaging of Head-and-Neck and Pancreatic Cancer in Humans by Targeting the "Cancer Integrin" Avβ6 with Ga-68-Trivehexin. *Eur. J. Nucl. Med. Mol. Imaging* **2022**, *49*, 1136–1147. https://doi.org/10.1007/S00259-021-05559-X.

20. Li, H.X.; Zheng, J.H.; Fan, H.X.; Li, H.P.; Gao, Z.X.; Chen, D. Expression of Avβ6 Integrin and Collagen Fibre in Oral Squamous Cell Carcinoma: Association with Clinical Outcomes and Prognostic Implications. *J. Oral Pathol. Med.* **2013**, *42*, 547–556. https://doi.org/10.1111/JOP.12044.

21. Ramos, D.M.; Dang, D.; Sadler, S. The Role of the Integrin Avβ6 in Regulating the Epithelial to Mesenchymal Transition in Oral Cancer. *Anticancer Res.* **2009**, *29*, 125–130.

22. Ramos, D.M.; But, M.; Regezi, J.; Schmidt, B.L.; Atakilit, A.; Dang, D.; Ellis, D.; Jordan, R.; Li, X. Expression of Integrin B6 Enhances Invasive Behavior in Oral Squamous Cell Carcinoma. *Matrix Biol.* **2002**, *21*, 297–307. https://doi.org/10.1016/S0945-053X(02)00002-1.

23. Winter, M.J.; Nagtegaal, I.D.; Van Krieken, J.H.J.M.; Litvinov, S.V. The Epithelial Cell Adhesion Molecule (Ep-CAM) as a Morphoregulatory Molecule Is a Tool in Surgical Pathology. *Am. J. Pathol.* **2003**, *163*, 2139. https://doi.org/10.1016/S0002-9440(10)63570-5.

24. van Driel, P.B.A.A.; Boonstra, M.C.; Prevoo, H.A.J.M.; van de Giessen, M.; Snoeks, T.J.A.; Tummers, Q.R.J.G.; Keereweer, S.; Cordfunke, R.A.; Fish, A.; van Eendenburg, J.D.H.; et al. EpCAM as Multi-Tumour Target for near-Infrared Fluorescence Guided Surgery. *BMC Cancer* **2016**, *16*, 884. https://doi.org/10.1186/S12885-016-2932-7.

25. Boogerd, L.S.F.; Boonstra, M.C.; Prevoo, H.A.J.M.; Handgraaf, H.J.M.; Kuppen, P.J.K.; Van De Velde, J.H.; Fish, A.; Cordfunke, R.A.; Rob, A.; Valentijn, P.M.; et al. Fluorescence-Guided Tumor Detection with a Novel Anti-EpCAM Targeted Antibody Fragment: Preclinical Validation. *Surg. Oncol.* **2019**, *28*, 1–8. https://doi.org/10.1016/j.suronc.2018.10.004.

26. Pontious, C.; Kaul, S.; Hong, M.; Hart, P.A.; Krishna, S.G.; Lara, L.F.; Conwell, D.L.; Cruz-Monserrate, Z. Cathepsin E Expression and Activity: Role in the Detection and Treatment of Pancreatic Cancer. *Pancreatology* **2019**, *19*, 951. https://doi.org/10.1016/J.PAN.2019.09.009.

27. Wang, L.; Liang, C.; Li, F.; Guan, D.; Wu, X.; Fu, X.; Lu, A.; Zhang, G. PARP1 in Carcinomas and PARP1 Inhibitors as Antineoplastic Drugs. *Int. J. Mol. Sci.* **2017**, *18*, 2111. https://doi.org/10.3390/IJMS18102111.

28. Kossatz, S.; Brand, C.; Gutiontov, S.; Liu, J.T.C.; Lee, N.Y.; Gonen, M.; Weber, W.A.; Reiner, T. Detection and Delineation of Oral Cancer with a PARP1 Targeted Optical Imaging Agent. *Sci. Rep.* **2016**, *6*, 21371. https://doi.org/10.1038/srep21371.

29. Sankaranarayanan, R.A.; Kossatz, S.; Weber, W.; Beheshti, M.; Morgenroth, A.; Mottaghy, F.M. Advancements in PARP1 Targeted Nuclear Imaging and Theranostic Probes. *J. Clin. Med.* **2020**, *9*, 2130. https://doi.org/10.3390/JCM9072130.

30. Demétrio de Souza França, P.; Kossatz, S.; Brand, C.; Karassawa Zanoni, D.; Roberts, S.; Guru, N.; Adilbay, D.; Mauguen, A.; Valero Mayor, C.; Weber, W.A.; et al. A Phase I Study of a PARP1-Targeted Topical Fluorophore for the Detection of Oral Cancer. *Eur. J. Nucl. Med. Mol. Imaging* **2021**, *48*, 3618–3630. https://doi.org/10.1007/s00259-021-05372-6.

31. Abd-Elgaliel, W.R.; Cruz-Monserrate, Z.; Logsdon, C.D.; Tung, C.H. Molecular Imaging of Cathepsin E-Positive Tumors in Mice Using a Novel Protease-Activatable Fluorescent Probe. *Mol. Biosyst.* **2011**, *7*, 3207. https://doi.org/10.1039/C1MB05215B.

32. Noh, H.; Hong, S.; Huang, S. Role of Urokinase Receptor in Tumor Progression and Development. *Theranostics* **2013**, *3*, 487–495. https://doi.org/10.7150/thno.4218.

33. Lv, T.; Zhao, Y.; Jiang, X.; Yuan, H.; Wang, H.; Cui, X.; Xu, J.; Zhao, J.; Wang, J. UPAR: An Essential Factor for Tumor Development. *J. Cancer* **2021**, *12*, 7026. https://doi.org/10.7150/JCA.62281.

34. Van Den Berg, Y.W.; Osanto, S.; Reitsma, P.H.; Versteeg, H.H. The Relationship between Tissue Factor and Cancer Progression: Insights from Bench and Bedside. *Blood* **2012**, *119*, 924–932. https://doi.org/10.1182/BLOOD-2011-06-317685.

35. Seto, S.; Onodera, H.; Kaido, T.; Yoshikawa, A.; Ishigami, S.; Arii, S.; Imamura, M. Tissue Factor Expression in Human Colorectal Carcinoma Correlation with Hepatic Metastasis and Impact on Prognosis. *Cancer* **2000**, *88*, 295–301. https://doi.org/10.1002/(SICI)1097-0142(20000115)88:2.

36. Akashi, T.; Furuya, Y.; Ohta, S.; Fuse, H. Tissue Factor Expression and Prognosis in Patients with Metastatic Prostate Cancer. *Urology* **2003**, *62*, 1078–1082. https://doi.org/10.1016/S0090-4295(03)00768-4.

37. Christensen, A.; Grønhøj, C.; Jensen, J.S.; Lelkaitis, G.; Kiss, K.; Juhl, K.; Charabi, B.W.; Mortensen, J.; Kjær, A.; Buchwald, C. von Expression Patterns of UPAR, TF and EGFR and Their Potential as Targets for Molecular Imaging in Oropharyngeal Squamous Cell Carcinoma. *Oncol. Rep.* **2022**, *48*, 147. https://doi.org/10.3892/OR.2022.8359.

38. Baart, V.M.; van Duijn, C.; van Egmond, S.L.; Dijckmeester, W.A.; Jansen, J.C.; Vahrmeijer, A.L.; Sier, C.F.M.; Cohen, D. Egfr and Avβ6 as Promising Targets for Molecular Imaging of Cutaneous and Mucosal Squamous Cell Carcinoma of the Head and Neck Region. *Cancers* **2020**, *12*, 1474. https://doi.org/10.3390/cancers12061474.

39. Serpa, M.S.; Mafra, R.P.; Queiroz, S.I.M.L.; da Silva, L.P.; de Souza, L.B.; Pinto, L.P. Expression of Urokinase-Type Plasminogen Activator and Its Receptorin Squamous Cell Carcinoma of the Oral Tongue. *Braz. Oral Res.* **2018**, *32*. https://doi.org/10.1590/1807-3107bor-2018.vol32.0093.

40. Carlsen, E.A.; Loft, M.; Loft, A.; Berthelsen, A.K.; Langer, S.W.; Knigge, U.; Kjaer, A. Prospective Phase II Trial of Prognostication by 68 Ga-NOTA-AE105 UPAR PET in Patients with Neuroendocrine Neoplasms: Implications for UPAR Targeted Therapy. *J. Nucl. Med.* **2022**, *63*, 1371–1377. https://doi.org/10.2967/JNUMED.121.263177.

41. Fosbøl, M.Ø.; Kurbegovic, S.; Johannesen, H.H.; Røder, M.A.; Hansen, A.E.; Mortensen, J.; Loft, A.; Petersen, P.M.; Madsen, J.; Brasso, K.; et al. Urokinase-Type Plasminogen Activator Receptor (UPAR) PET/MRI of Prostate Cancer for Noninvasive Evaluation of Aggressiveness: Comparison with Gleason Score in a Prospective Phase 2 Clinical Trial. *J. Nucl. Med.* **2021**, *62*, 354–359. https://doi.org/10.2967/JNUMED.120.248120.

42. Persson, M.; Skovgaard, D.; Brandt-Larsen, M.; Christensen, C.; Madsen, J.; Nielsen, C.H.; Thurison, T.; Klausen, T.L.; Holm, S.; Loft, A.; et al. First-in-Human UPAR PET: Imaging of Cancer Aggressiveness. *Theranostics* **2015**, *5*, 1303–1316. https://doi.org/10.7150/thno.12956.

43. Risoer, L.M.; Clausen, M.M.; ujmajuridze, zaza; Farhadi, M.; Andersen, K.F.; Loft, A.; Kjaer, A. Prognostic Value of Urokinase-Type Plasminogen Activator Receptor (UPAR)-PET/CT in Head and Neck Squamous Cell Carcinomas and Comparison with 18 F-FDG-PET/CT: A Single-Center Prospective Study. *J. Nucl. Med.* **2021**, *63*, 1169–1176. https://doi.org/10.2967/jnumed.121.262866.

44. Christensen, A.; Juhl, K.; Persson, M.; Charabi, B.W.; Mortensen, J.; Kiss, K.; Lelkaitis, G.; Rubek, N.; von Buchwald, C.; Kjær, A. UPAR-Targeted Optical near-Infrared (NIR) Fluorescence Imaging and PET for Image-Guided Surgery in Head and Neck Cancer: Proof-of-Concept in Orthotopic Xenograft Model. *Oncotarget* **2017**, *8*, 15407–15419. https://doi.org/10.18632/oncotarget.14282.

45. Boonstra, M.C.; Van Driel, P.B.A.A.; Keereweer, S.; Prevoo, H.A.J.M.; Stammes, M.A.; Baart, V.M.; Löwik, C.W.G.M.; Mazar, A.P.; van de Velde, C.J.H.; Vahrmeijer, A.L.; et al. Preclinical UPAR-Targeted Multimodal Imaging of Locoregional Oral Cancer. *Oral Oncol.* **2017**, *66*, 1–8. https://doi.org/10.1016/j.oraloncology.2016.12.026.

46. Christensen, A.; Kiss, K.; Lelkaitis, G.; Juhl, K.; Persson, M.; Charabi, B.W.; Mortensen, J.; Forman, J.L.; Sørensen, A.L.; Jensen, D.H.; et al. Urokinase-Type Plasminogen Activator Receptor (UPAR), Tissue Factor (TF) and Epidermal Growth Factor Receptor (EGFR): Tumor Expression Patterns and Prognostic Value in Oral Cancer. *BMC Cancer* **2017**, *17*, 572. https://doi.org/10.1186/s12885-017-3563-3.

47. Wei, W.; Liu, Q.; Jiang, D.; Zhao, H.; Kutyreff, C.J.; Engle, J.W.; Liu, J.; Cai, W. Tissue Factor-Targeted ImmunoPET Imaging and Radioimmunotherapy of Anaplastic Thyroid Cancer. *Adv. Sci.* **2020**, *7*, 1903595. https://doi.org/10.1002/ADVS.201903595.

48. Nielsen, C.H.; Erlandsson, M.; Jeppesen, T.E.; Jensen, M.M.; Kristensen, L.K.; Madsen, J.; Petersen, L.C.; Kjaer, A. Quantitative PET Imaging of Tissue Factor Expression Using 18F-Labeled Active Site–Inhibited Factor VII. *J. Nucl. Med.* **2016**, *57*, 89–95. https://doi.org/10.2967/JNUMED.115.154849.

49. Takashima, H.; Tsuji, A.B.; Saga, T.; Yasunaga, M.; Koga, Y.; Kuroda, J.I.; Yano, S.; Kuratsu, J.I.; Matsumura, Y. Molecular Imaging Using an Anti-Human Tissue Factor Monoclonal Antibody in an Orthotopic Glioma Xenograft Model. *Sci. Rep.* **2017**, *71*, 12341. https://doi.org/10.1038/s41598-017-12563-5.

50. Sugyo, A.; Aung, W.; Tsuji, A.B.; Sudo, H.; Takashima, H.; Yasunaga, M.; Matsumura, Y.; Saga, T.; Higashi, T. Anti-tissue Factor Antibody-mediated Immuno-SPECT Imaging of Tissue Factor Expression in Mouse Models of Pancreatic Cancer. *Oncol. Rep.* **2019**, *41*, 2371–2378. https://doi.org/10.3892/OR.2019.7017.

51. Food and Drug Administration FDA Grants Accelerated Approval to Tisotumab Vedotin-Tftv for Recurrent or Metastatic Cervical Cancer. Available online: https://www.fda.gov/drugs/resources-information-approved-drugs/fda-grants-accelerated-approval-tisotumab-vedotin-tftv-recurrent-or-metastatic-cervical-cancer (accessed on 19 September 2022).

52. Loft, M.; Christensen, C.; Clausen, M.M.; Carlsen, E.A.; Hansen, C.P.; Kroman, N.; Langer, S.W.; Høgdall, C.; Madsen, J.; Gillings, N.; et al. First-in-Human PET Imaging of Tissue Factor in Patients with Primary and Metastatic Cancers Using 18F-Labeled Active-Site Inhibited Factor VII (18F-ASIS): Potential as Companion Diagnostic. *J. Nucl. Med.* **2022**, *63*, 1871–1879. https://doi.org/10.2967/JNUMED.122.264068.

53. Yakavets, I.; Francois, A.; Guiot, M.; Lequeux, N.; Fragola, A.; Pons, T.; Bezdetnaya, L.; Marchal, F. NIR Imaging of the Integrin-Rich Head and Neck Squamous Cell Carcinoma Using Ternary Copper Indium Selenide/Zinc Sulfide-Based Quantum Dots. *Cancers* **2020**, *12*, 3727. https://doi.org/10.3390/cancers12123727.

54. de Valk, K.S.; Deken, M.M.; Handgraaf, H.J.M.; Bhairosingh, S.S.; Bijlstra, O.D.; van Esdonk, M.J.; Terwisscha van Scheltinga, A.G.T.; P.M.; Valentijn, A.R.; March, T.L.; Vuijk, J.; et al. First-in-Human Assessment of CRGD-ZW800-1, a Zwitterionic, Integrin-Targeted, Near-Infrared Fluorescent Peptide in Colon Carcinoma. *Clin. Cancer Res.* **2020**, *26*, 3990–3998. https://doi.org/10.1158/1078-0432.CCR-19-4156/15460/AM/FIRST-IN-HUMAN-ASSESSMENT-OF-CRGD-ZW800-1-A.

55. Hyytiäinen, A.; Wahbi, W.; Väyrynen, O.; Saarilahti, K.; Karihtala, P.; Salo, T.; Al-Samadi, A. Angiogenesis Inhibitors for Head and Neck Squamous Cell Carcinoma Treatment: Is There Still Hope? *Front. Oncol.* **2021**, *11*, 2123. https://doi.org/10.3389/FONC.2021.683570/FULL.

56. Van Oosten, M.; Crane, L.M.A.; Bart, J.; Van Leeuwen, F.W.; Van Dam, G.M. Selecting Potential Targetable Biomarkers for Imaging Purposes in Colorectal Cancer Using TArget Selection Criteria (TASC): A Novel Target Identification Tool. *Transl. Oncol.* **2011**, *4*, 71–82. https://doi.org/10.1593/tlo.10220.

57. van der Fels, C.A.M.; Palthe, S.; Buikema, H.; van den Heuvel, M.C.; Leliveld, A.; de Jong, I.J. Potential Receptors for Targeted Imaging of Lymph Node Metastases in Penile Cancer. *Diagnostics* **2020**, *10*, 694. https://doi.org/10.3390/diagnostics10090694.

58. de Gooyer, J.M.; Versleijen-Jonkers, Y.M.H.; Hillebrandt-Roeffen, M.H.S.; Frielink, C.; Desar, I.M.E.; de Wilt, J.H.W.; Flucke, U.; Rijpkema, M. Immunohistochemical Selection of Biomarkers for Tumor-Targeted Image-Guided Surgery of Myxofibrosarcoma. *Sci. Rep.* **2020**, *10*, 2915. https://doi.org/10.1038/S41598-020-59735-4.

59. Linders, D.; Deken, M.; van der Valk, M.; Tummers, W.; Bhairosingh, S.; Schaap, D.; van Lijnschoten, G.; Zonoobi, E.; Kuppen, P.; van de Velde, C.; et al. CEA, EpCAM, Avβ6 and UPAR Expression in Rectal Cancer Patients with a Pathological Complete Response after Neoadjuvant Therapy. *Diagnostics* **2021**, *11*, 516. https://doi.org/10.3390/DIAGNOSTICS11030516.

MDPI

Article

Diagnostic Value of Preoperative uPAR-PET/CT in Regional Lymph Node Staging of Oral and Oropharyngeal Squamous Cell Carcinoma: A Prospective Phase II Trial

Mads Lawaetz [1,2], Anders Christensen [1,2], Karina Juhl [2], Giedrius Lelkaitis [3], Kirstine Karnov [1,2,†], Esben Andreas Carlsen [2], Birgitte W. Charabi [1], Annika Loft [2], Dorota Czyzewska [2], Christian von Buchwald [1] and Andreas Kjaer [2,*]

1   Department of Otolaryngology, Head and Neck Surgery and Audiology, Rigshospitalet, Copenhagen University Hospital, 2100 Copenhagen, Denmark; mads.lawaetz@regionh.dk (M.L.)
2   Department of Clinical Physiology, Nuclear Medicine and PET and Cluster for Molecular Imaging, Copenhagen University Hospital—Rigshospitalet & Department of Biomedical Sciences, University of Copenhagen, 2100 Copenhagen, Denmark; dorota.czyzewska@regionh.dk (D.C.)
3   Department of Pathology, Rigshospitalet, Copenhagen University Hospital, 2100 Copenhagen, Denmark
*   Correspondence: akjaer@sund.ku.dk
†   Kirstine Karnov sadly passed away before publication of this study.

Abstract: The detection of lymph node metastases is a major challenge in oral and oropharyngeal squamous cell carcinoma (OSCC and OPSCC). ^{68}Ga-NOTA-AE105 is a novel positron emission tomography (PET) radioligand with high affinity to urokinase-type plasminogen activator receptor (uPAR), a receptor expressed on the surfaces of tumor cells. The aim of this study was to investigate the diagnostic value of uPAR-PET/CT (computerized tomography) in detecting regional metastatic disease in patients with OSCC and OPSCC compared to the current imaging work-up. In this phase II trial, patients with OSCC and OPSCC referred for surgical treatment were prospectively enrolled. Before surgery, ^{68}Ga-NOTA-AE105 uPAR-PET/CT was conducted, and SUVmax values were obtained from the primary tumor and the suspected lymph nodes. Histology results from lymph nodes were used as the standard of truth of metastatic disease. The diagnostic values of ^{68}Ga-uPAR-PET/CT were compared to conventional routine preoperative imaging results (CT and/or MRI). The uPAR expression in resected primary tumors and metastases was determined by immunohistochemistry and quantified digitally (H-score). A total of 61 patients underwent uPAR-PET/CT. Of the 25 patients with histologically verified lymph node metastases, uPAR-PET/CT correctly identified regional metastatic disease in 14 patients, with a median lymph node metastasis size of 14 mm (range 3–27 mm). A significant correlation was found between SUVmax and the product of the H-score and tumor depth (r = 0.67; *p* = 0.003). The sensitivity and specificity of uPAR-PET/CT in detecting regional metastatic disease were 56% and 100%, respectively. When added to CT/MRI, uPAR-PET was able to upstage 2/11 (18%) of patients with occult metastases and increase the sensitivity to 64%. The sensitivity and specificity of ^{68}Ga-NOTA-AE105 uPAR-PET/CT were equivalent to those of CT/MRI. The significant correlation between SUVmax and uPAR expression verified the target specificity of ^{68}Ga-NOTA-AE105. Despite the target specificity, the sensitivity of imaging is too low for nodal staging and it cannot replace neck dissection.

Keywords: urokinase-type plasminogen activator receptor (uPAR); PET/CT; ^{68}Ga-NOTA-AE105; lymph node metastases; head and neck cancer

1. Introduction

Oral (OSCC) and oropharyngeal (OPSCC) squamous cell carcinomas are two of the most frequent malignancies of the head and neck [1]. The occurrence of cervical lymph node metastases is the most important clinical prognostic factor [2–5]. The detection of

lymph node metastases remains a major challenge in OSCC and OPSCC, where 21–33% of patients without clinically suspicious regional lymph nodes (cN0 neck) have occult regional metastases at the time of diagnosis that are not detected on magnetic resonance imaging (MRI), computed tomography (CT) or ultrasound [6–8]. Other imaging modalities, like ^{18}F-FDG-PET, play an important role in head and neck squamous cell carcinoma (HNSCC), particularly in post-treatment evaluation, but lack the sensitivity to replace sentinel node biopsy or elective neck dissection, for staging and surgical planning [9]. Sentinel node biopsy is a minimally invasive method of staging the clinically and radiologically cN0 neck in patients with early-stage OSCC or OPSCC, and it has demonstrated equivalency with elective neck dissection [10]. The accurate and noninvasive identification of patients with lymph node metastases is critical in selecting the most effective treatment and reducing the frequency of unnecessary neck procedures. Unfortunately, there are currently no noninvasive imaging methods that can accomplish this.

Urokinase-type plasminogen activator receptor (uPAR) is a glyciphosphatidyliunositol (GPI)-anchored cell membrane receptor that facilitates cell invasion and metastasis by converting plasminogen into plasmin at the cell surface and thus degrading the extracellular matrix [11]. uPAR has been found upregulated in tumor cells in many solid cancers, including HNSCC, with low or absent expression in normal tissue [12–15]. Due to the tumor-specific expression of uPAR and its significance in cancer, our research group developed ^{68}Ga-NOTA-AE105, a novel PET radioligand with a strong affinity to uPAR. The biodistribution, safety and tumor detection ability of ^{68}Ga-NOTA-AE105 have been investigated in a phase I study [16], and recent phase II studies have shown the significant prognostic value of uPAR-PET/CT in patients with HNSCC [17] and in patients with neuroendocrine neoplasms [18]. However, the diagnostic value of uPAR-PET/CT in OSCC and OPSCC has not yet been explored.

The aim of this phase II study was therefore to investigate the diagnostic value of ^{68}Ga-NOTA-AE105 uPAR-PET/CT in detecting regional metastatic disease in patients with OSCC and OPSCC compared to the current imaging work-up.

2. Materials and Methods

2.1. Study Design and Patients

In this prospective phase II trial, patients with biopsy-verified OSCC and OPSCC, with or without suspicion of regional neck metastases, referred for primary surgery at the Department of Otolaryngology, Head & Neck Surgery and Audiology, Rigshospitalet, Copenhagen University Hospital, Denmark, were prospectively enrolled between November 2016 and January 2022. Patients between the ages of 18 and 85 years, who were able to read, comprehend and provide informed consent, were eligible. Exclusion criteria were previous surgery or radiation therapy to the neck, obesity (bodyweight > 140 kg), allergy to ^{68}Ga-NOTA-AE105 or pregnancy. Patients were enrolled in this trial following a standard evaluation and imaging work-up. The study design is shown in Figure 1. From patient records, data on age, gender, stage, preoperative imaging modalities, laboratory findings and histology results were obtained. Patients' disease stage was classified according to the 8th edition of the Union for International Cancer Control (UICC) staging manual [19]. Patients included between 2016 and 2018, i.e., prior to the introduction of the 8th edition of the UICC staging manual, were subsequently reclassified according to this edition, so that all patients were classified according to the most recent TNM staging manual. The study was approved by the Danish Research Ethics Committee (protocol no. H-16032922) and the Danish Medicines Agency (protocol no. 2016122500). The trial was registered in the European Union Drug Regulating Authorities Clinical Trials Database (EudraCT no. 2016-002360-14) and on ClinicalTrials.gov (Identifier: NCT02960724) and conducted in compliance with the Good Clinical Practice (GCP) recommendations.
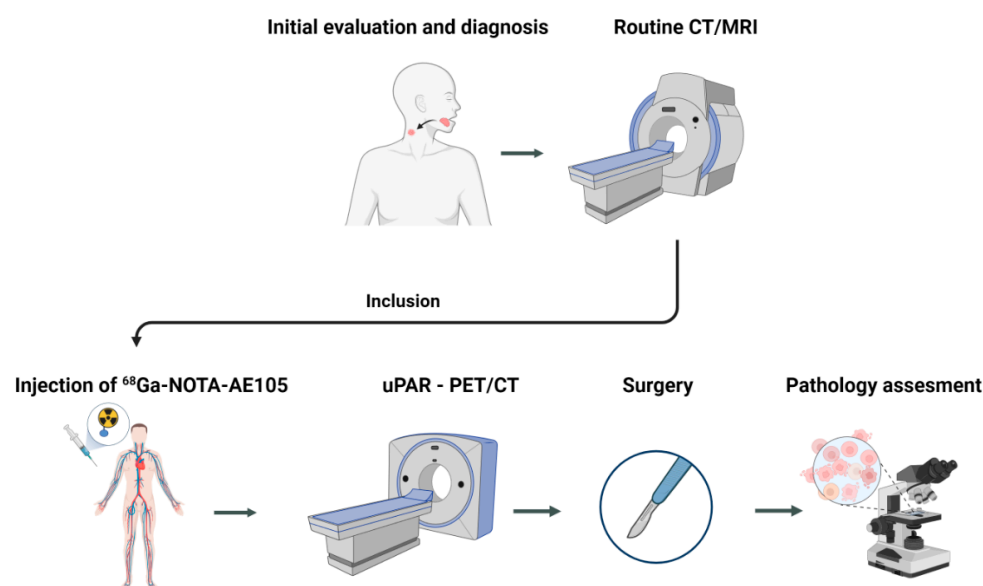
Figure 1. The study design. Patients, regardless of lymph node status, were included after routine evaluation and imaging. Following uPAR-PET/CT, patients underwent surgical excision of the primary tumor and the removal of regional lymph nodes (sentinel node dissection and/or elective neck dissection). uPAR-PET/CT-positive lymph nodes were finally compared to the pathology results.

2.2. Image Acquisition

The radioligand, ^{68}Ga-NOTA-AE105, was produced in-house as previously published [16]. Before surgery, patients underwent a whole-body PET/CT scan 20 min after the injection of approximately 200 MBq (median 199 MBq, range 112–214 MBq) of ^{68}Ga-NOTA-AE105. Whole-body PET and diagnostic CT with iodine intravenous contrast (skull base to proximal thigh) were performed in the same session with an integrated whole-body PET/CT system (Siemens Biograph mCT 64 slice, Siemens, Munich, Germany) with patients placed in a supine position. The PET data were reconstructed using an iterative reconstruction technique that used time of flight, point spread function and attenuation correction with 2 iterations, 21 subsets and a 2 mm Gaussian filter. The CT scan was carried out with 120 kV, 170 mAs and a pitch of 0.8. Any adverse events were recorded within 24 h following ^{68}Ga-NOTA-AE105 injection.

2.3. Image Analysis

All ^{68}Ga-uPAR-PET/CT scans were evaluated by an experienced physician in nuclear medicine and an experienced radiologist working side by side, both blinded to all clinical data, including the TNM stage and results from the previous routine imaging work-up (CT/MRI). The lymph nodes were classified as positive if the team visually found higher uptake in a lymph node compared with surrounding normal tissue. In the case of a positive lymph node on uPAR-PET/CT, the volume of the entire lymph node was contoured and, from this, the maximum standardized uptake value (SUV_{max}) was obtained. The radiologist determined the anatomic lymph node level of each uPAR-PET/CT-positive lymph node. Later, the neck uPAR-PET/CT results were compared to the histology report (considered the gold standard) in which the dissected levels were documented. The diagnostic performance of uPAR-PET/CT was determined as the presence or absence of lymph node metastases in a neck region compared to the histology report. The results from uPAR-PET/CT were compared with results from the previous routine imaging work-up (CT/MRI).

2.4. Tissue Selection and Immunohistochemistry

A specialized head and neck pathologist analyzed all resected primary tumor specimens and lymph nodes. The maximum depth of the primary tumor was measured microscopically. All resected tissue was formalin-fixed and paraffin-embedded. Smaller

nodes were embedded in paraffin in toto, whereas larger nodes were divided and then embedded. Representative diagnostic slides were obtained from alle blocks as part of the routine pathology examination.

All formalin-fixated paraffin-embedded tumor samples from resected primary tumors and lymph node metastases were collected for this study. uPAR expression was determined by immunohistochemistry on 4 μm slides. Slides were incubated in 60 °C for 60 min and afterwards deparaffinized with xylene and rehydrated in decreasing grades of alcohol. Antigen retrieval was carried out in CC1 antigen retrieval buffer (Ventana Medical Systems, Tucson, AZ, USA) for 10 min at 95 °C. Endogenous peroxidase was blocked for 8 min with peroxidase-blocking solution (DAKO s2023). Blocking for unspecific antibody binding was performed using 2% BSA. Slides were incubated with uPAR-specific antibody (GeneTex, Irwine, CA, USA, product no. GTX100467, concentration 1:500) for 1 h. After this, the slides were incubated with the secondary antibody (DAKO anti-rabbit K4003) for 45 min. Staining was visualized using the DAB+ substrate chromogen system (DAKO K3468) and the specimens were lastly stained with hematoxylin for 60 s. The primary antibody was used at optimal dilution using positive and negative control staining.

2.5. Immunohistochemistry Scoring

An experienced head and neck pathologist digitally annotated the tumor compartments in both primary tumors and lymph node metastases and excluded necrotic areas using the open-source software Qupath version 0.3.2 [20]. Within the tumor compartment, cells were digitally identified as positive or negative based on the mean DAB signal in the cell cytoplasm. Cell expansion was set to 5 μm and the intensity threshold was set to 0.12 for weak intensity (+1), 0.25 for moderate intensity (+2) and 0.50 for strong intensity (+3). From these settings, the positive proportion of tumor cells and the H-score within the tumor compartment were calculated. The H-score ranged from 0 to 300 based on the following formula: $3 \times$ percentage of strongly stained cells + $2 \times$ percentage of moderately stained cells + percentage of poorly stained cells. The product of the H-score and tumor depth were correlated to SUV_{max} for all primary tumors.

2.6. Statistical Analysis

Sensitivity, specificity and negative and positive predictive values (NPV and PPV) were calculated per patient. McNemar's test was used for comparison between uPAR-PET/CT and standard-of-care tests (CT/MRI). Pathology results from surgery were used as the gold standard. Correlation between SUV_{max} and the histology findings in primary tumors was performed using Spearman's rank correlation test. The Mann–Whitney U test was used to compare the mean tumor depth between groups. All continuous values are reported as the median and range or mean $\pm$ SD. A p-value less than 0.05 was regarded as statistically significant. All statistical analyses were performed using IBM SPSS statistics version 25.0.

3. Results

3.1. Patients

We included 66 patients with OSCC and OPSCC in this phase II trial between November 2016 and January 2022. Five patients were excluded due to failed radiopharmaceutical production, leaving 61 patients with an ^{68}Ga-NOTA-AE105uPAR-PET/CT for the final analyses (Figure 2). No adverse reactions or clinically detectable side effects related to the radioligand administration were observed. Patient characteristics are shown in Table 1. The median age of patients was 66 years, and the majority (79%) were diagnosed with OSCC. Sixty percent of patients were diagnosed in the early stage (stage I-II) and the vast majority (79%) of patients had small (T1-T2) primary tumors. Of the 13 patients with oropharyngeal cancer, ten patients had p16-positive tumors, eight of them with confirmed HPV-positive status (two not tested). All patients underwent standard-of-care examinations (CT and/or MRI), and 15/61 (23%) patients were preoperatively diagnosed with

image- or pathology-verified lymph node metastases. The neck was managed with sentinel node biopsy (39%), selective neck dissection (51%) or a combination of both (7%). Sentinel node biopsies were only performed for patients with preoperative N0 neck. One of the 24 patients who underwent sentinel node biopsy was diagnosed with a lymph node metastasis. This patient was subsequently treated with a neck dissection, but no additional lymph node metastases were found. Two patients elected observation over neck surgery, leaving the N-stage histologically unconfirmed. Ten patients were upstaged to pN+ due to the detection of subclinical lymph node metastases following surgery, bringing the total number of patients with histologically verified regional metastases to 25 (41%). The median time from uPAR-PET/CT to surgery was 2 days (range 1–12).
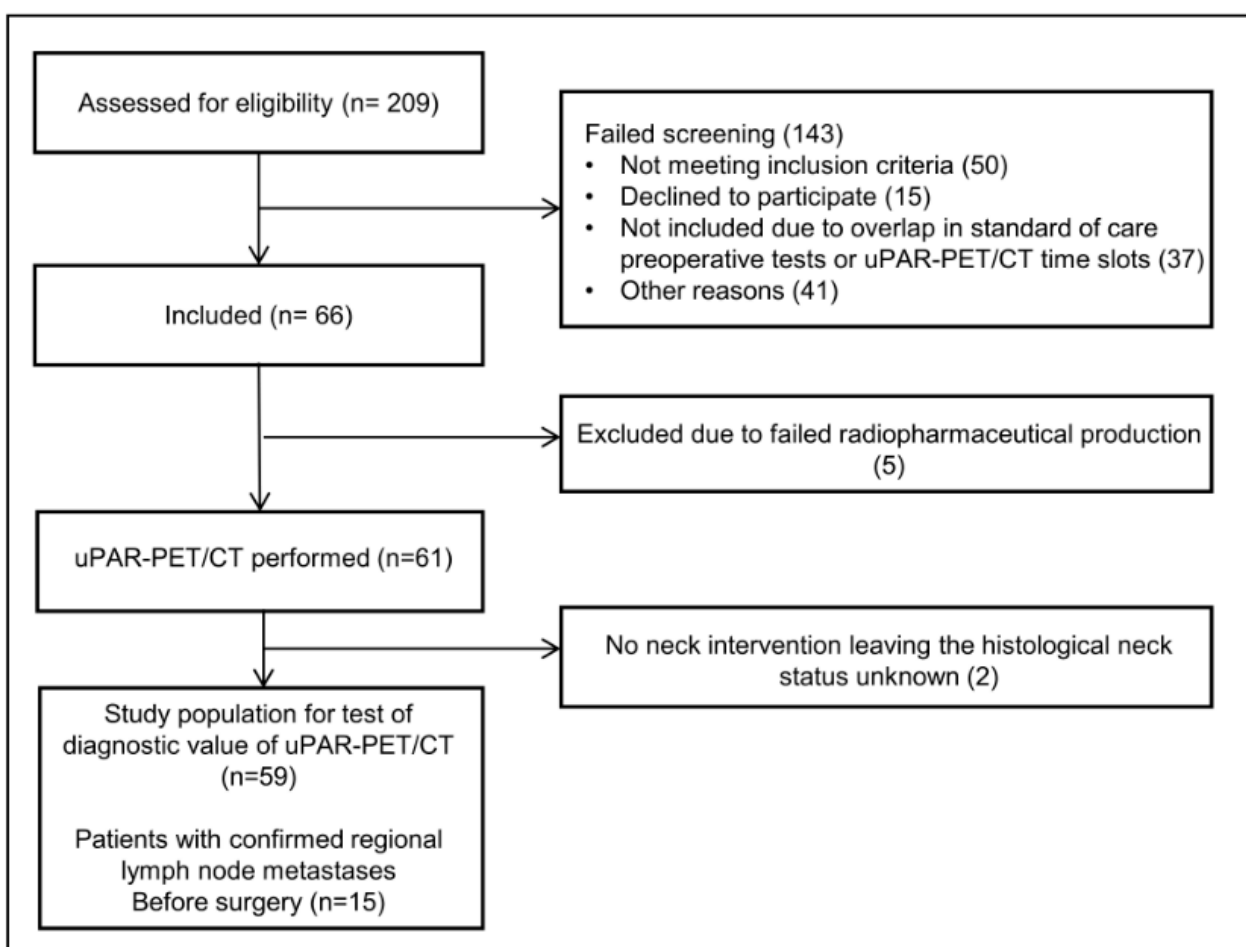
Figure 2. CONSORT flow diagram of the study.

Table 1. Characteristics of included patients and their tumor stages. All included patients were treated with primary surgery at the T-site. Neck interventions were performed as part of the primary surgery.

Characteristics	Value
Age (years)	Median, 66; range, 39–80
Male/female (n)	21/40 (34%/66%)
Primary site (n)	
Oral cavity	48 (79%)
Oropharynx	13 (21%)

Table 1. *Cont.*

Characteristics	Value
Treatment on N-site	
Sentinel node	24 (39%)
Oropharynx (N0/N+)	0/0
Oral (N0/N+)	23/1
Selective neck	31 (51%)
Combination	4 (7%)
No neck surgery	2 (3%)
Stage (n)	
pI	34 (55%)
pII	6 (10%)
pIII	7 (11.5%)
pIV	14 (23%)
T-stage (n)	
pT1	31 (51%)
pT2	17 (28%)
pT3	2 (3%)
pT4	11 (18%)
Preoperative N-stage (n)	
cN0	46 (75%)
cN+	15 (25%)
Postoperative N-stage (n)	
pN0	36 (59%)
pN+	25 (51%)

3.2. Diagnostic Value of uPAR-PET/CT

In total, 59 patients with a neck intervention and histology-defined neck status were included in the calculation of sensitivity, specificity, PPV and NPV (Table 2). Among the 25 patients with histologically verified lymph node metastases, uPAR-PET/CT found regional metastatic disease in 14 patients (example shown in Figure 3). The same number of patients were also identified with regional metastatic disease after standard-of-care preoperative CT/MRI. However, there was a discordance between CT/MRI and uPAR-PET/CT in four cases. In two patients, uPAR-PET/CT correctly detected lymph node disease while CT/MRI was negative, whereas the inverse was observed in the two other patients. The lymph node metastases not identified by uPAR-PET/CT were significantly smaller than those detected ($p = 0.006$), with a median size in the undetected of 5 mm (range 0.1–10), compared to the median size in the detected of 14 mm (range 3–27 mm). For both uPAR-PET/CT and CT/MRI, the sensitivity and specificity on a per patient basis were 56% and 100%, respectively (no significant differences).

Table 2. Diagnostic accuracy of uPAR PET/CT compared to CT/MRI for assessment of regional metastatic disease in patients with OSCC and OPSCC using pathology results as gold standard. uPAR: urokinase-type plasminogen activator receptor. pN+: pathology-verified lymph node metastatic disease. pN0: no lymph node metastases after pathology assessment of surgically removed lymph nodes.

Imaging Modality		Pathology Results, n (%)		
		Positive (pN+)	Negative (pN0)	Total
uPAR-PET/CT	Positive	14	0	14
	Negative	11	34	45
	Total	25	34	59
	Sensitivity = 56%	**Specificity = 100%**	**PPV = 100%**	**NPV = 76%**

Table 2. *Cont.*

Imaging Modality		Pathology Results, n (%)		
		Positive (pN+)	Negative (pN0)	Total
CT/MRI (standard examinations)	Positive	14	0	14
	Negative	11	34	45
	Total	25	34	59
	Sensitivity = 56%	**Specificity = 100%**	**PPV = 100%**	**NPV = 76%**
uPAR-PET/CT and CT/MRI combined	Positive	16	0	16
	Negative	9	34	43
	Total	25	34	59
	Sensitivity = 64%	**Specificity = 100%**	**PPV = 100%**	**NPV = 79%**
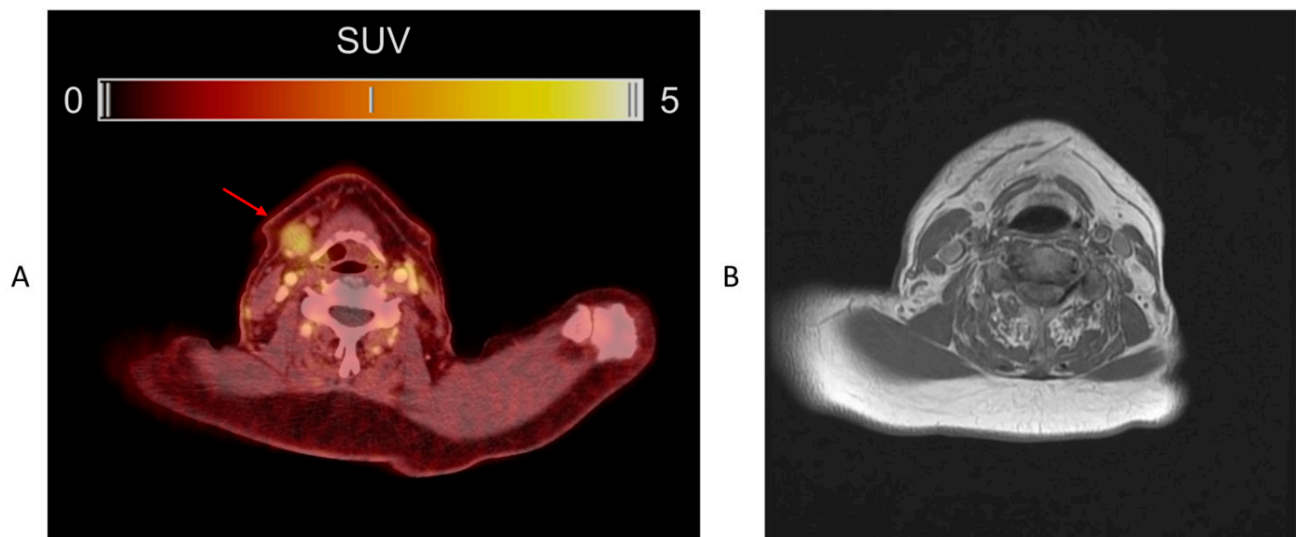
Figure 3. (**A**) ^{68}Ga-NOTA-AE105 uPAR-PET/CT of a patient with lymph node metastasis, not detected by routine imaging work-up (CT/MRI). (**B**) MRI from the same patient.

If standard-of-care examinations were combined with uPAR-PET/CT, the sensitivity could be increased from 56% to 64% and the NPV from 76% to 79%. An additional 2 of 11 (18%) patients with occult metastases would have been upstaged. uPAR-PET/CT was not able to detect additional metastases in patients with clinically N+ neck (patients with cervical lymph nodes already detected by routine clinical/imaging work-up).

The median SUV_{max} for lymph node metastasis was 2.62 (range 1.81–4.57); for primary tumors, it was 2.82 (range 2.00–4.40). Due to the presence of several small and superficial primary tumors, the image analysis team was only able to measure SUV values for 18/61 primary tumors for the comparison of SUV values and uPAR expression. The primary tumors identified by CT were significantly larger than the undetected tumors, with a mean tumor depth of 10.2 ± 6.2 mm versus 4.6 ± 3.5 mm ($p < 0.001$), respectively.

3.3. Immunohistochemistry

All primary tumors and lymph node metastases detected by CT exhibited uPAR-expression. Seventeen of the eighteen primary tumors with measurable SUV values were available for immunohistochemical examination and were assessed digitally using Qupath (Figure 4). The mean proportion of positive cells in the tumor compartments of the uPAR-PET/CT-detected tumors was 44.7 ± 22.7% and they had an H-score of 66.9 ± 36.2. A

significant correlation was found in primary tumors between the SUV_{max} and the product of the H-score and tumor depth ($p = 0.003$; r = 0.67) (Figure 5). There was not sufficient tissue available from lymph node metastases to obtain a meaningful correlation between the SUV values and immunohistochemistry results.
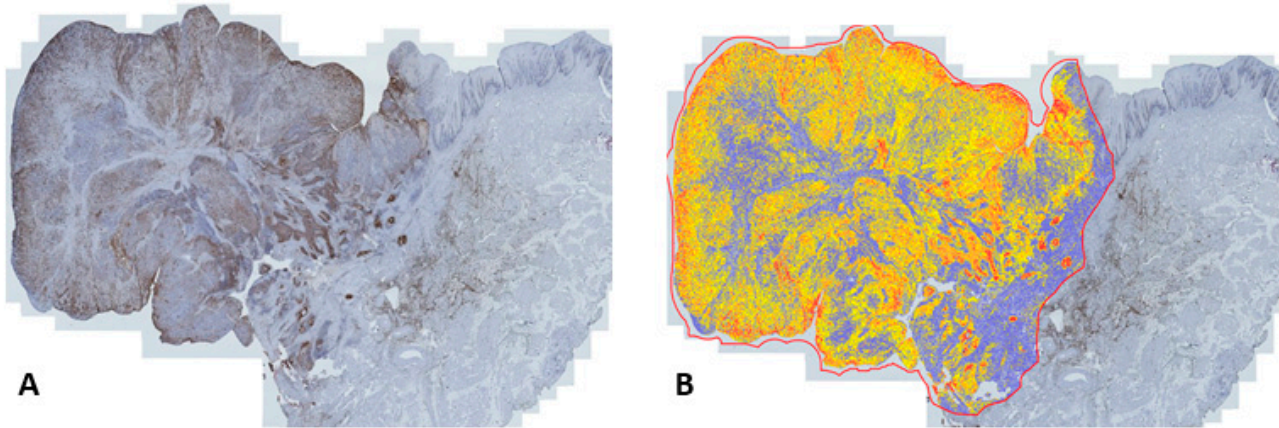

Figure 4. (**A**) uPAR expression in the primary tumor compartment determined with immunohistochemistry. (**B**) Digital scoring of staining intensity using Qupath (yellow = 1+, orange = 2+ and red = 3+).
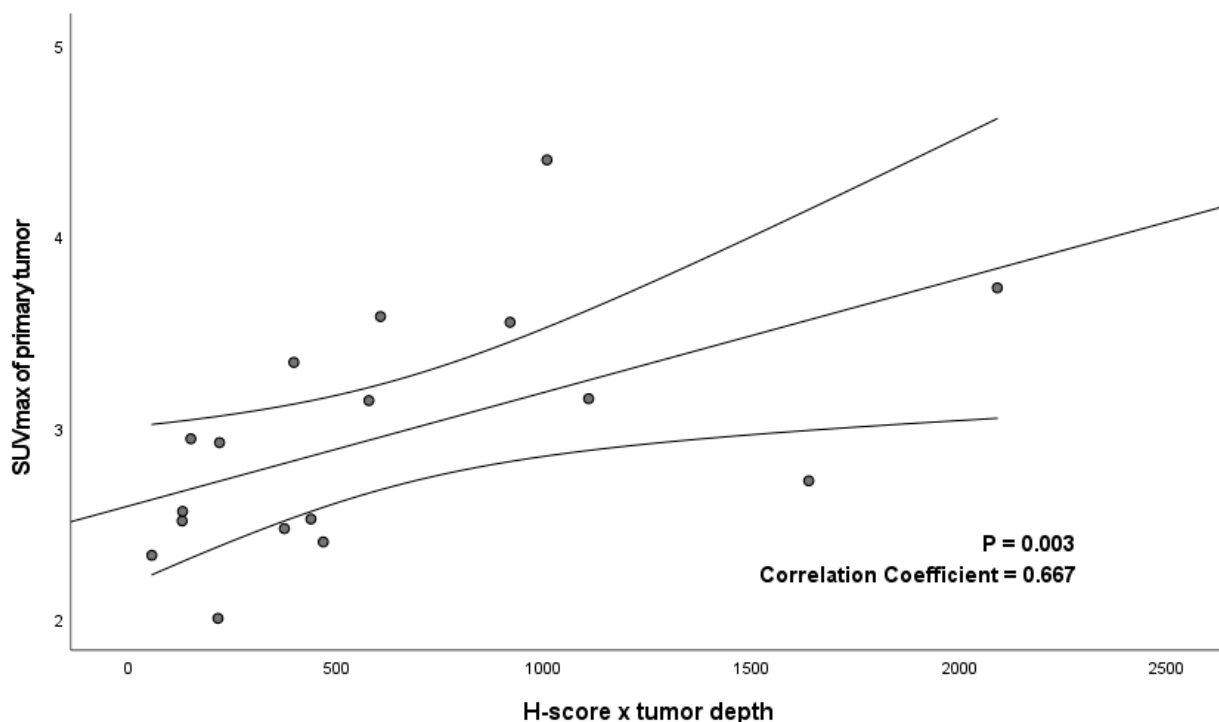
Figure 5. Correlation between SUV_{max} and the immunohistochemical uPAR expression expressed as the product of H-score and tumor depth in 17 primary tumors.

4. Discussion

This prospective phase II trial including 61 patients is the first study to examine the diagnostic value of uPAR-PET/CT in patients surgically treated for OSCC and OPSCC. We found that ^{68}Ga-NOTA-AE105 uPAR-PET/CT had, on a per-patient basis, sensitivity and specificity in detecting regional metastatic disease of 56% and 100%. All patients with a uPAR-PET/CT-positive neck had a histologically verified nodal malignancy, which resulted in a positive predictive value of 100%. Additionally, we found a significant correlation

between SUV_{max} in the primary tumor tissue and uPAR expression, demonstrating the uPAR specificity of the PET signal.

uPAR-PET/CT and CT/MRI detected an equal number of individuals with lymph node disease; however, a discordance was seen in four patients. As a result, the combination of these modalities enhanced the diagnostic value and enabled the detection of 2/11 (18%) patients with occult metastases, rendering the sentinel node procedure unnecessary for this group. These findings suggest that uPAR-PET in combination with CT/MRI could be used to enhance the diagnostic value for tumor tissue detection in OSCC and OPSCC.

In this study, we used the in-house-produced radiotracer composed of the uPAR-specific peptide AE105, the chelator NOTA and the radiometal ^{68}Ga. The advantage of ^{68}Ga-labeled peptides is that they can be produced without the need for a cyclotron onsite [21]. However, the short half-life of ^{68}Ga ($T_{\frac{1}{2}}$ = 68 min) also represents challenges as it needs to be radiolabeled onsite, requiring radiochemistry laboratories. Using ^{64}Cu ($T_{1/2}$: 12.7 h) instead would allow for the central production and distribution of the radiopharmaceutical. Furthermore, the positron range for ^{68}Ga (4 mm) is longer than that of, e.g., ^{64}Cu (1 mm), which could increase the detection of smaller tumor deposits due to the increased spatial resolution, as demonstrated by our group in a head-to-head comparison of ^{64}Cu and ^{68}Ga-based PET tracers in neuroendocrine tumors [22]. This issue was also reported in a study using a ^{68}Ga-labeled radiotracer for the PET/CT imaging of lymph node metastases in prostate cancer, which concluded that the detection rate was influenced by the metastasis size [23]. Prior animal and phase I studies have shown good resolutions with the ^{64}Cu-based uPAR-PET tracer ^{64}Cu-DOTA-AE105. Accordingly, it could be interesting to explore this uPAR-PET tracer in OSCC and OPSCC patients in future studies to increase the detection of occult metastasis and smaller lesions [24,25]. In our study, indeed, we experienced a challenge in identifying smaller quantities of tumor tissue, as both primary tumors and metastases not detected by ^{68}Ga uPAR-PET/CT were significantly smaller than those detected. Nonetheless, some primary tumors and metastases of reasonable size were not detected by ^{68}Ga-uPAR-PET/CT, indicating that the magnitude of the PET signal is not dependent on the tumor size alone, but may be a combination of the uPAR expression in tumor cells and the tumor volume. This was supported by the significant correlation between SUV_{max} and the product of the H-score and tumor depth (Figure 5). Furthermore, this correlation confirms findings from the previous phase I study that the uPAR-PET-signal in tumors is uPAR-specific [24,26].

So far, the use of PET in HNSCC has focused on ^{18}F-fluorodeoxyglucose (^{18}F-FDG) [27]. It has been shown that the combination of ^{18}F-FDG-PET and CT is useful in detecting unknown primary tumors, secondary primary tumors and distant metastases [28,29], but the detection of small metastases in patients with a clinically N0 neck has been a challenge [30]. However, a recent prospective multicenter study investigating the diagnostic value of ^{18}F-FDG-PET/CT in patients with HNSCC showed a high negative predictive value for N0 neck in patients with more advanced disease, i.e., T2–T4 tumors [31]. In recent years, there has been increasing interest in a new PET tracer, ^{68}Ga-labeled fibroblast activation protein inhibitor (^{68}Ga-FAPI), in different cancers, including head and neck. Fibroblast activation protein (FAP) has, in immunohistochemical studies, been found upregulated in various head and neck malignancies [32,33]. Imaging with ^{68}Ga-FAPI PET/CT in head and neck cancer has demonstrated high-contrast imaging in both primary tumors and metastases and low uptake in healthy tissue [34]. For the staging of HNSCC, ^{68}Ga-FAPI PET/CT has also demonstrated promising results in prospective trials, and it was recently found to outperform ^{18}FDG-PET/CT in preoperative lymph node staging [35].

It was not possible to compare uPAR-PET/CT to ^{18}F-FDG-PET/CT in our study due to the short window of time between diagnosis and surgery and because ^{18}F-FDG-PET is not a part of the normal imaging work-up prior to surgery at our institution. However, neither ^{18}F-FDG-PET/CT nor uPAR-PET/CT appear capable of replacing sentinel node biopsies or elective neck dissection in the nodal staging of OPSCC and OSCC. However, uPAR-PET/CT might have another role in patients with OSCC and OPSCC; a recent study investigating

the prognostic value of ^{68}Ga-NOTA-AE105 uPAR-PET/CT in HNSCC patients referred for curatively intended radiotherapy revealed that the SUV$_{max}$ value is a prognostic factor for recurrence and may be a tool to identify patients with a high risk of recurrence [17]. Furthermore, uPAR-PET/CT has the potential to serve as a diagnostic tool to select patients for uPAR-targeted optically guided surgery, a modality currently being tested in a phase II trial in OSCC and OPSCC patients (EudraCT no. 2022-001361-12), or uPAR-targeted radionuclide therapy, which has previously been demonstrated to be effective in animal models of human prostate cancer [36] and colorectal cancer [37].

This study had some limitations. First, the CT/MRI was performed and described as part of the clinical routine examination; thus, the radiologist was not blinded to the clinical information gathered prior to imaging (e.g., clinical description, ultrasound or fine needle aspiration). In contrast, the uPAR PET/CT operator was blinded to all clinical data; consequently, there was a risk of uPAR PET/CT underperformance in comparison to CT/MRI. Secondly, this was a relatively small study and some of the findings may need to be substantiated in larger phase III studies.

5. Conclusions

This phase II study, evaluating the diagnostic value of ^{68}Ga-NOTA-AE105 uPAR-PET/CT in identifying lymph node metastases in patients with OSCC or OPSCC, showed sensitivity and specificity equivalent to CT/MRI, with limitations in identifying smaller volumes of tumor tissue. Adding uPAR-PET to the current imaging work-up led to the identification of an additional 18% of patients with occult metastatic disease. In addition, a strong correlation was found between the uPAR expression in primary tumors and the ^{68}Ga-NOTA-AE105 uPAR-PET signal measured as SUV$_{max}$, confirming the uPAR specificity of the radiotracer. However, despite the target specificity and the ability to increase the sensitivity when added to CT/MRI, the sensitivity is too low for nodal staging and this method cannot replace neck dissection.

Author Contributions: Conceptualization, M.L., K.K., A.C., K.J., B.W.C., C.v.B. and A.K.; Formal analysis, M.L., K.K., A.C., K.J., D.C., A.L. and A.K.; Funding acquisition, C.v.B. and A.K.; Investigation, M.L., K.J. and A.K.; Methodology, M.L., K.K., A.C., K.J., G.L., E.A.C., C.v.B. and A.K.; Project administration, M.L., K.K., C.v.B. and A.K.; Software, M.L., K.J. and G.L.; Supervision, A.C., K.J., C.v.B. and A.K.; Validation, M.L., K.J. and G.L.; Visualization, M.L. and K.J.; Writing—original draft, M.L.; Writing—review and editing, A.C., K.J., G.L., E.A.C., B.W.C., D.C., A.L., C.v.B. and A.K. All authors have read and agreed to the published version of the manuscript.

Institutional Review Board Statement: The study was conducted in accordance with the Declaration of Helsinki and approved by the Danish Research Ethics Committee (protocol no. H-16032922) and the Danish Medicines Agency (protocol no. 2016122500). The trial was registered in the European Union Drug Regulating Authorities Clinical Trials Database (EudraCT no. 2016-002360-14) and at ClinicalTrials.gov (Identifier: NCT02960724) and was conducted in compliance with the Good Clinical Practice (GCP) recommendations.

Informed Consent Statement: Informed consent was obtained from all patients involved in the study.

Data Availability Statement: Data are not publicly available due to protection of personal data and medical confidentiality.

Conflicts of Interest: Andreas Kjaer is the inventor of the uPAR-PET radiotracer ^{68}Ga-NOTA-AE105 (WO 2014086364) and co-founder of Curasight, which is further developing uPAR-PET. There are no other conflict of interest associated with this article.

References

1. Sung, H.; Ferlay, J.; Siegel, R.L.; Laversanne, M.; Soerjomataram, I.; Jemal, A.; Bray, F. Global Cancer Statistics 2020: GLOBOCAN Estimates of Incidence and Mortality Worldwide for 36 Cancers in 185 Countries. *CA Cancer J. Clin.* **2021**, *71*, 209–249. [CrossRef] [PubMed]
2. Zanoni, D.K.; Montero, P.H.; Migliacci, J.C.; Shah, J.P.; Wong, R.J.; Ganly, I.; Patel, S.G. Survival Outcomes after Treatment of Cancer of the Oral Cavity (1985–2015). *Oral Oncol.* **2019**, *90*, 115–121. [CrossRef]
3. Faisal, M.; Dhanani, R.; Ullah, S.; Bakar, M.A.; Irfan, N.; Malik, K.I.; Loya, A.; Boban, E.M.; Hussain, R.; Jamshed, A. Prognostic Outcomes of Treatment Naïve Oral Tongue Squamous Cell Carcinoma (OTSCC): A Comprehensive Analysis of 14 Years. *Eur. Arch. Oto-Rhino-Laryngol.* **2021**, *278*, 3045–3053. [CrossRef] [PubMed]
4. Teraphongphom, N.; Kong, C.S.; Warram, J.M.; Rosenthal, E.L. Specimen Mapping in Head and Neck Cancer Using Fluorescence Imaging. *Laryngoscope Investig. Otolaryngol.* **2017**, *2*, 447. [CrossRef]
5. Layland, M.K.; Sessions, D.G.; Lenox, J. The Influence of Lymph Node Metastasis in the Treatment of Squamous Cell Carcinoma of the Oral Cavity, Oropharynx, Larynx, and Hypopharynx: N0 versus N+. *Laryngoscope* **2005**, *115*, 629–639. [CrossRef] [PubMed]
6. Shimizu, K.I.; Inoue, H.; Saitoh, M.; Ohtsuki, N.; Ishida, H.; Makino, K.; Amatsu, M.; Nibu, K.I. Distribution and Impact of Lymph Node Metastases in Oropharyngeal Cancer. *Acta Otolaryngol.* **2006**, *126*, 872–877. [CrossRef]
7. Amit, M.; Yen, T.C.; Liao, C.T.; Binenbaum, Y.; Chaturvedi, P.; Agarwal, J.P.; Kowalski, L.P.; Ebrahimi, A.; Clark, J.R.; Cernea, C.R.; et al. Clinical Nodal Stage Is a Significant Predictor of Outcome in Patients with Oral Cavity Squamous Cell Carcinoma and Pathologically Negative Neck Metastases: Results of the International Consortium for Outcome Research. *Ann. Surg. Oncol.* **2013**, *20*, 3575–3581. [CrossRef]
8. Barrera, J.E.; Miller, M.E.; Said, S.; Jafek, B.W.; Campana, J.P.; Shroyer, K.R. Detection of Occult Cervical Micrometastases in Patients with Head and Neck Squamous Cell Cancer. *Laryngoscope* **2003**, *113*, 892–896. [CrossRef]
9. Plaxton, N.A.; Brandon, D.C.; Corey, A.S.; Harrison, C.E.; Kendi, A.T.K.; Halkar, R.K.; Barron, B.J. Characteristics and Limitations of FDG PET/CT for Imaging of Squamous Cell Carcinoma of the Head and Neck: A Comprehensive Review of Anatomy, Metastatic Pathways, and Image Findings. *Am. J. Roentgenol.* **2015**, *205*, W519–W531. [CrossRef] [PubMed]
10. Garrel, R.; Poissonnet, G.; Plana, A.M.; Fakhry, N.; Dolivet, G.; Lallemant, B.; Sarini, J.; Vergez, S.; Guelfucci, B.; Choussy, O.; et al. Equivalence Randomized Trial to Compare Treatment on the Basis of Sentinel Node Biopsy versus Neck Node Dissection in Operable T1-T2N0 Oral and Oropharyngeal Cancer. *J. Clin. Oncol.* **2020**, *38*, 4010–4018. [CrossRef]
11. Noh, H.; Hong, S.; Huang, S. Role of Urokinase Receptor in Tumor Progression and Development. *Theranostics* **2013**, *3*, 487–495. [CrossRef]
12. Lawaetz, M.; Christensen, A.; Juhl, K.; Karnov, K.; Lelkaitis, G.; Fiehn, A.-M.K.; Kjaer, A.; Von Buchwald, C. Potential of UPAR, Avβ6 Integrin, and Tissue Factor as Targets for Molecular Imaging of Oral Squamous Cell Carcinoma: Evaluation of Nine Targets in Primary Tumors and Metastases by Immunohistochemistry. *Int. J. Mol. Sci.* **2023**, *24*, 3853. [CrossRef]
13. Lv, T.; Zhao, Y.; Jiang, X.; Yuan, H.; Wang, H.; Cui, X.; Xu, J.; Zhao, J.; Wang, J. UPAR: An Essential Factor for Tumor Development. *J. Cancer* **2021**, *12*, 7026. [CrossRef] [PubMed]
14. Christensen, A.; Grønhøj, C.; Jensen, J.S.; Lelkaitis, G.; Kiss, K.; Juhl, K.; Charabi, B.W.; Mortensen, J.; Kjær, A.; Von Buchwald, C. Expression Patterns of UPAR, TF and EGFR and Their Potential as Targets for Molecular Imaging in Oropharyngeal Squamous Cell Carcinoma. *Oncol. Rep.* **2022**, *48*, 147. [CrossRef] [PubMed]
15. Christensen, A.; Kiss, K.; Lelkaitis, G.; Juhl, K.; Persson, M.; Charabi, B.W.; Mortensen, J.; Forman, J.L.; Sørensen, A.L.; Jensen, D.H.; et al. Urokinase-Type Plasminogen Activator Receptor (UPAR), Tissue Factor (TF) and Epidermal Growth Factor Receptor (EGFR): Tumor Expression Patterns and Prognostic Value in Oral Cancer. *BMC Cancer* **2017**, *17*, 572. [CrossRef]
16. Skovgaard, D.; Persson, M.; Brandt-Larsen, M.; Christensen, C.; Madsen, J.; Klausen, T.L.; Holm, S.; Andersen, F.L.; Loft, A.; Berthelsen, A.K.; et al. Safety, Dosimetry, and Tumor Detection Ability of 68Ga-NOTA-AE105: First-in-Human Study of a Novel Radioligand for UPAR PET Imaging. *J. Nucl. Med.* **2017**, *58*, 379–386. [CrossRef] [PubMed]
17. Risør, L.M.; Clausen, M.M.; Ujmajuridze, Z.; Farhadi, M.; Andersen, K.F.; Loft, A.; Kjaer, A. Prognostic Value of Urokinase-Type Plasminogen Activator Receptor (UPAR)-PET/CT in Head and Neck Squamous Cell Carcinomas and Comparison with 18 F-FDG-PET/CT: A Single-Center Prospective Study. *J. Nucl. Med.* **2022**, *63*, 1169–1176. [CrossRef]
18. Carlsen, E.A.; Loft, M.; Loft, A.; Berthelsen, A.K.; Langer, S.W.; Knigge, U.; Kjaer, A. Prospective Phase II Trial of Prognostication by 68Ga-NOTA-AE105 UPAR PET in Patients with Neuroendocrine Neoplasms: Implications for UPAR-Targeted Therapy. *J. Nucl. Med.* **2022**, *63*, 1371–1377. [CrossRef]
19. Huang, S.H.; O'Sullivan, B. Overview of the 8th Edition TNM Classification for Head and Neck Cancer. *Curr. Treat. Options Oncol.* **2017**, *18*, 40. [CrossRef]
20. Bankhead, P.; Loughrey, M.B.; Fernández, J.A.; Dombrowski, Y.; McArt, D.G.; Dunne, P.D.; McQuaid, S.; Gray, R.T.; Murray, L.J.; Coleman, H.G.; et al. QuPath: Open Source Software for Digital Pathology Image Analysis. *Sci. Rep.* **2017**, *7*, 16878. [CrossRef]
21. Banerjee, S.R.; Pomper, M.G. Clinical Applications of Gallium-68. *Appl. Radiat. Isot.* **2013**, *76*, 2–13. [CrossRef]

22. Johnbeck, C.B.; Knigge, U.; Loft, A.; Berthelsen, A.K.; Mortensen, J.; Oturai, P.; Langer, S.W.; Elema, D.R.; Kjaer, A. Head-to-Head Comparison of 64Cu-DOTATATE and 68Ga-DOTATOC PET/CT: A Prospective Study of 59 Patients with Neuroendocrine Tumors. *J. Nucl. Med.* **2017**, *58*, 451–457. [CrossRef]

23. Budäus, L.; Leyh-Bannurah, S.R.; Salomon, G.; Michl, U.; Heinzer, H.; Huland, H.; Graefen, M.; Steuber, T.; Rosenbaum, C. Initial Experience of 68Ga-PSMA PET/CT Imaging in High-Risk Prostate Cancer Patients Prior to Radical Prostatectomy. *Eur. Urol.* **2016**, *69*, 393–396. [CrossRef]

24. Persson, M.; Skovgaard, D.; Brandt-Larsen, M.; Christensen, C.; Madsen, J.; Nielsen, C.H.; Thurison, T.; Klausen, T.L.; Holm, S.; Loft, A.; et al. First-in-Human UPAR PET: Imaging of Cancer Aggressiveness. *Theranostics* **2015**, *5*, 1303. [CrossRef]

25. Persson, M.; Madsen, J.; Østergaard, S.; Jensen, M.M.; Jørgensen, J.T.; Juhl, K.; Lehmann, C.; Ploug, M.; Kjaer, A. Quantitative PET of Human Urokinase-Type Plasminogen Activator Receptor with 64Cu-DOTA-AE105: Implications for Visualizing Cancer Invasion. *J. Nucl. Med.* **2012**, *53*, 138–145. [CrossRef] [PubMed]

26. Skovgaard, D.; Persson, M.; Kjaer, A. Urokinase Plasminogen Activator Receptor–PET with 68Ga-NOTA-AE105: First Clinical Experience with a Novel PET Ligand. *PET Clin.* **2017**, *12*, 311–319. [CrossRef] [PubMed]

27. Eyassu, E.; Young, M. Nuclear Medicine PET/CT Head and Neck Cancer Assessment, Protocols, and Interpretation. In *StatPearls*; StatPearls Publishing: Treasure Island, FL, USA, 2022.

28. Johansen, J.; Buus, S.; Loft, A.; Keiding, S.; Overgaard, M.; Hansen, H.S.; Grau, C.; Bundgaard, T.; Kirkegaard, J.; Overgaard, J. Prospective Study of 18FDG-PET in the Detection and Management of Patients with Lymph Node Metastases to the Neck from an Unknown Primary Tumor. Results from the DAHANCA-13 Study. *Head Neck* **2008**, *30*, 471–478. [CrossRef]

29. Kim, S.Y.; Roh, J.L.; Yeo, N.K.; Kim, J.S.; Lee, J.H.; Choi, S.H.; Nam, S.Y. Combined 18F-Fluorodeoxyglucose-Positron Emission Tomography and Computed Tomography as a Primary Screening Method for Detecting Second Primary Cancers and Distant Metastases in Patients with Head and Neck Cancer. *Ann. Oncol.* **2007**, *18*, 1698–1703. [CrossRef]

30. Evangelista, L.; Cervino, A.R.; Chondrogiannis, S.; Marzola, M.C.; Maffione, A.M.; Colletti, P.M.; Muzzio, P.C.; Rubello, D. Comparison between Anatomical Cross-Sectional Imaging and 18F-FDG PET/CT in the Staging, Restaging, Treatment Response, and Long-Term Surveillance of Squamous Cell Head and Neck Cancer: A Systematic Literature Overview. *Nucl. Med. Commun.* **2014**, *35*, 123–134. [CrossRef]

31. Lowe, V.J.; Duan, F.; Subramaniam, R.M.; Sicks, J.R.D.; Romanoff, J.; Bartel, T.; Jian, Q.; Nussenbaum, B.; Richmon, J.; Arnold, C.D.; et al. Multicenter Trial of [18F]Fluorodeoxyglucose Positron Emission Tomography/Computed Tomography Staging of Head and Neck Cancer and Negative Predictive Value and Surgical Impact in the N0 Neck: Results From ACRIN 6685. *J. Clin. Oncol.* **2019**, *37*, 1704. [CrossRef] [PubMed]

32. Mona, C.E.; Benz, M.R.; Hikmat, F.; Grogan, T.R.; Lueckerath, K.; Razmaria, A.; Riahi, R.; Slavik, R.; Girgis, M.D.; Carlucci, G.; et al. Correlation of 68Ga-FAPi-46 PET Biodistribution with FAP Expression by Immunohistochemistry in Patients with Solid Cancers: A Prospective Translational Exploratory Study. *J. Nucl. Med.* **2022**, *63*, 1021–1026. [CrossRef]

33. Röhrich, M.; Syed, M.; Liew, D.P.; Giesel, F.L.; Liermann, J.; Choyke, P.L.; Wefers, A.K.; Ritz, T.; Szymbara, M.; Schillings, L.; et al. 68Ga-FAPI-PET/CT Improves Diagnostic Staging and Radiotherapy Planning of Adenoid Cystic Carcinomas—Imaging Analysis and Histological Validation. *Radiother. Oncol.* **2021**, *160*, 192–201. [CrossRef] [PubMed]

34. Syed, M.; Flechsig, P.; Liermann, J.; Windisch, P.; Staudinger, F.; Akbaba, S.; Koerber, S.A.; Freudlsperger, C.; Plinkert, P.K.; Debus, J.; et al. Fibroblast Activation Protein Inhibitor (FAPI) PET for Diagnostics and Advanced Targeted Radiotherapy in Head and Neck Cancers. *Eur. J. Nucl. Med. Mol. Imaging* **2020**, *47*, 2836–2845. [CrossRef] [PubMed]

35. Jiang, Y.; Wen, B.; Li, C.; Tian, Y.; Xiao, Z.; Xu, K.; Xing, D.; Yu, Z.; Huang, J.; Jia, J.; et al. The Performance of 68Ga-FAPI-04 PET/CT in Head and Neck Squamous Cell Carcinoma: A Prospective Comparison with 18F-FDG PET/CT. *Eur. J. Nucl. Med. Mol. Imaging* **2023**, *50*, 2114–2126. [CrossRef]

36. Persson, M.; Juhl, K.; Rasmussen, P.; Brandt-Larsen, M.; Madsen, J.; Ploug, M.; Kjaer, A. UPAR Targeted Radionuclide Therapy with 177Lu-DOTA-AE105 Inhibits Dissemination of Metastatic Prostate Cancer. *Mol. Pharm.* **2014**, *11*, 2796–2806. [CrossRef]

37. Persson, M.; Rasmussen, P.; Madsen, J.; Ploug, M.; Kjaer, A. New Peptide Receptor Radionuclide Therapy of Invasive Cancer Cells: In Vivo Studies Using 177 Lu-DOTA-AE105 Targeting UPAR in Human Colorectal Cancer Xenografts. *Nucl. Med. Biol.* **2012**, *39*, 962–969. [CrossRef] [PubMed]

RESEARCH ARTICLE

Urokinase-Type Plasminogen Activator Receptor (uPAR) Expression and [64Cu]Cu-DOTA-AE105 uPAR-PET/CT in Patient-Derived Xenograft Models of Oral Squamous Cell Carcinoma

Mads Lawaetz[1,2] · Tina Binderup[2] · Anders Christensen[1,2] · Karina Juhl[2] · Giedrius Lelkaitis[3] · Eva Lykke[1] · Line Knudsen[2] · Christian von Buchwald[1] · Andreas Kjaer[2]

Abstract

Purpose [64Cu]Cu-DOTA-AE105 urokinase-type plasminogen activator receptor (uPAR)-PET/CT is a novel and promising imaging modality for cancer visualization, although it has not been tested in head and neck cancer patients nor in preclinical models that closely resemble these heterogenous tumors, i.e., patient-derived xenograft (PDX) models. The aim of the present study was to establish and validate oral squamous cell carcinoma (OSCC) PDX models and to evaluate [64Cu]Cu-uPAR-PET/CT for tumor imaging in these models.

Procedures PDX flank tumor models were established by engrafting tumor tissue from three patients with locally advanced OSCC into immunodeficient mice. [64Cu]Cu-DOTA-AE105 was injected in passage 2 (P2) mice, and [64Cu]Cu-uPAR-PET/CT was performed 1 h and 24 h after injection. After the last PET scan, all animals were euthanized, and tumors dissected for autoradiography and immunohistochemical (IHC) staining.

Results Three PDX models were established, and all of them showed histological stability and unchanged heterogenicity, uPAR expression, and Ki67 expression through passages. A significant correlation between uPAR expression and tumor growth was found. All tumors of all models ($n=29$) showed tumor uptake of [64Cu]Cu-DOTA-AE105. There was a clear visual concordance between the distribution of uPAR expression (IHC) and [64Cu]Cu-DOTA-AE105 uptake pattern in tumor tissue (autoradiography). No significant correlation was found between IHC (H-score) and PET-signal (SUV_{max}) ($r=0.34$; $p=0.07$).

Conclusions OSCC PDX models in early passages histologically mimic donor tumors and could serve as a valuable platform for the development of uPAR-targeted imaging and therapeutic modalities. Furthermore, [64Cu]Cu-uPAR-PET/CT showed target- and tumor-specific uptake in OSCC PDX models demonstrating the diagnostic potential of this modality for OSCC patients.

Keywords Urokinase-type plasminogen activator receptor · Patient-derived xenograft models · PET/CT · 64Cu-DOTA-AE105 · Oral squamous cell carcinoma

✉ Mads Lawaetz
madslawaetz@gmail.com

[1] Department of Otolaryngology, Head and Neck Surgery and Audiology, Rigshospitalet, Copenhagen University Hospital, Copenhagen, Denmark

[2] Department of Clinical Physiology, Nuclear Medicine and PET and Cluster for Molecular Imaging, Copenhagen University Hospital - Rigshospitalet & Department of Biomedical Sciences, University of Copenhagen, Copenhagen, Denmark

[3] Department of Pathology, Rigshospitalet, Copenhagen University Hospital, Copenhagen, Denmark

Introduction

Head and neck cancer is the seventh most prevalent malignancy worldwide, with more than 850,000 new cases per year [1]. Of these, cancer of the oral squamous cell carcinoma (OSCC) represents the most frequent type. Despite advancement in treatment, the prognosis in the recent decades has stayed poor with a 5-year overall survival of approximately 45–65 % [2, 3]. One of the major challenges in OSCC is to identify metastases to regional lymph nodes especially in patients with early-stage disease, which is reflected in a high number of patients with occult metastases (20–30%) [4–6]. Current non-invasive imaging techniques

like computerized tomography (CT), magnetic resonance imaging (MRI), or ^18F-flouro-deoxy-glucose positron emission tomography (^18F-FDG-PET) lack the ability to accurately identify small nodal tumor deposits, and therefore, patients with early-stage disease without clinical metastases are recommended removal of regional lymph nodes either as sentinel node or elective neck dissection [7, 8]. Accurate staging and effective treatment are essential for improving the prognosis for patients with OSCC. Consequentially, there is a clinical need to improve existing OSCC diagnostic approaches. In this search, targeted molecular imaging is expected to play an important role. Tumor-targeted molecular imaging enables tumor-specific visualization and has the potential to identify patients who may benefit from targeted treatment (e.g., radionuclide therapy) as well as monitoring treatment effect [9]. Numerous biomarkers have been examined as targets for PET imaging of head and neck cancer. These biomarkers encompass integrin αvβ6 [10], integrin αvβ3 [11], epidermal growth factor receptor (EGFR) [12], and poly(ADP-ribose)polymerase-1 (PARP-1) [13]. However, none of these has been applied in clinical practice.

The urokinase-type plasminogen activator receptor (uPAR) is a cell membrane receptor converting plasminogen to plasmin, thereby activating several proteases leading to degradation of extracellular matrix, which facilitates cancer cell invasion. uPAR has been shown to be involved in many aspects of tumor development including tumor invasion and metastasis [14, 15]. The utilization of uPAR as a biomarker for PET imaging of OSCC is a topic of significant interest. One of the notable advantages associated with uPAR is its significant expression in OSCC, observed in primary tumors, lymph node metastases, and recurring tumor tissue. Moreover, uPAR is highly expressed along the invasive front within tumors and in tumor-related activated stromal cells, while its expression in normal tissue is limited [14, 16–18]. Thus, uPAR is an attractive imaging and therapeutic target. uPAR has in clinical phase II studies been investigated as a nuclear medicine-based molecular imaging target for PET in different cancers including prostate [19], neuroendocrine [20], and head and neck [21], where it has shown a significant prognostic value. All clinical uPAR-PET studies have used the peptide (AE105), with high affinity to uPAR, radiolabelled with galium-68 ([^68Ga]Ga). The peptide AE105, consisting of nine amino acids, exhibits a strong binding affinity to the human uPAR protein. It forms a stable complex in a 1:1 stoichiometry, with a dissociation constant (KD) of 0.4 nM. AE105 has been found to be a highly effective competitive inhibitor of the uPA-uPAR interaction, with an inhibitory concentration (IC50) of 11 nM [22]. [^68Ga]Ga has a known limitation in spatial resolution compared to other isotopes like copper-64 ([^64Cu]Cu) [23]. [^64Cu]Cu-uPAR-PET with [^64Cu]Cu-DOTA-AE105 has only been evaluated in preclinical models in different cancers and in one phase I clinical trial in patients with breast, prostate, and lung cancer [24, 25] but never in head and neck cancer patients nor preclinical models that closely resembles OSCC tissue characteristics.

Most preclinical studies investigating imaging targets like uPAR have been performed in cell line-derived xenograft models. These models only partially mimic human malignancies and lack tumor heterogeneity and the cellular stromal tumor micro-environment-like cancer-associated fibroblasts and tumor-associated macrophages [26]. Patient-derived xenograft (PDX) models are models created by implantation of small and minimally processed patient-derived tumor pieces into immunodeficient mice. It has been demonstrated that these models preserve the tumor micro-environment, the heterogeneity, and mutations and have a high predictive value regarding patients [27, 28]. PDX models are thus expected to be a better and more realistic platform for developing new imaging modalities and therapy, especially for a target like uPAR, which is also expressed by tumor-infiltrating macrophages and fibroblasts in the tumor stromal compartment [29, 30]. PDX models of head and neck cancer have previously been studied and shown to be able to replicate human disease in terms of both histopathological and molecular characteristics [31–33]. In addition, PDX models of head and neck cancer have been demonstrated to mimic therapeutic response and have been proposed as a paraclinical model for investigating personalized therapy [34, 35]. To our knowledge, the expression of uPAR in PDX models has not previously been studied.

The primary aim of this study was to establish new OSCC PDX models, and the secondary goal was to investigate the use of [^64Cu]Cu-uPAR-PET/CT in PDX models and evaluate the distribution of the tracer ([^64Cu]Cu-DOTA-AE105) in tumor tissue.

Materials and Methods

Patient Selection and Study Design

Patients diagnosed with OSCC referred for primary surgery at the Department of Otolaryngology, Head and Neck Surgery and Audiology, Rigshospitalet between 2020 and 2021, were included and contacted regarding the donation of tumor tissue. Signed informed consent was obtained for all included patients. Clinicopathological data was collected from pathology reports. A biopsy was harvested from the resected primary tumor by a specialized head and neck pathologist (GL) without compromising tumor margin analysis. The primary tumor was divided into three pieces, one for formalin fixation, one for RNA analysis, and one for implantation in mice. The following implantation process

and *ex vivo* analyses are shown in Fig. 1 and explained in detail below.

The study was approved by the Danish National Committee on Health and Research Ethics (H-17025452) and conducted in accordance with the Declaration of Helsinki (2002). Data were handled in accordance with the guidelines set by the Danish Data Protection Agency (No. 2012-58-0004)

Animals

All animal experiments were performed in accordance with Danish laws under the license no. 2021-15-0201-01041. Female NMRI nude mice were used for the study (*n*=53 in total for establishment, expansion, and imaging study), Janvier Labs (Le Genest-Saint-Isle, France).

Establishment of PDX Models

Within 1 h after the operation, tissue was implanted in mice. The pathologist localized viable tumor tissue in the resected specimen from primary tumor and placed the tissue in cold Gibco RPMI 1640 Media mixed with 10% Fetal Bovine Serum (Thermofisher Scientific, DK). Under aseptic conditions, tissue was chopped into a mesh, mixed 1:1 with Corning™ Matrigel™ (Thermofisher Scientific, DK) and

divided in 5×5 mm samples for implantation in the flank of the mice (iteration 1, passage 0 (P0)). When tumor reached exponential growth, it was further passaged to 5 mice (P1) for expansion. Once tumors in P1 reached a volume > 1000 mm^3, it was further passaged to 10–16 mice (P2) for use in the PET/CT study. The three models utilized were those that exhibited the highest degree of similarity in terms of growth and were available at the same time. The uPAR expression in these models was unknown at the time of inclusion. At date of PET scans, mice with tumors larger than 300 mm^3 were included in the imaging study: model 1 (*n*=9), model 2 (*n*=10), and model 3 (*n*=10).

Radiochemistry

The production of [^{64}Cu]Cu-DOTA-AE105 is described in detail in supplementary material.

Imaging Protocol and Imaging Analysis

Mice were anesthetized with 1.5% sevoflurane (Baxter Healthcare Ltd, UK) mixed with 35% O2 in ambient air through a nose cone, and 2 mice were scanned simultaneously. A dedicated small-animal PET/CT scanner (Inveon®, Siemens Medical Systems, PA, USA) were used. [^{64}Cu]Cu -DOTA-AE105 was injected in a lateral tail vein and
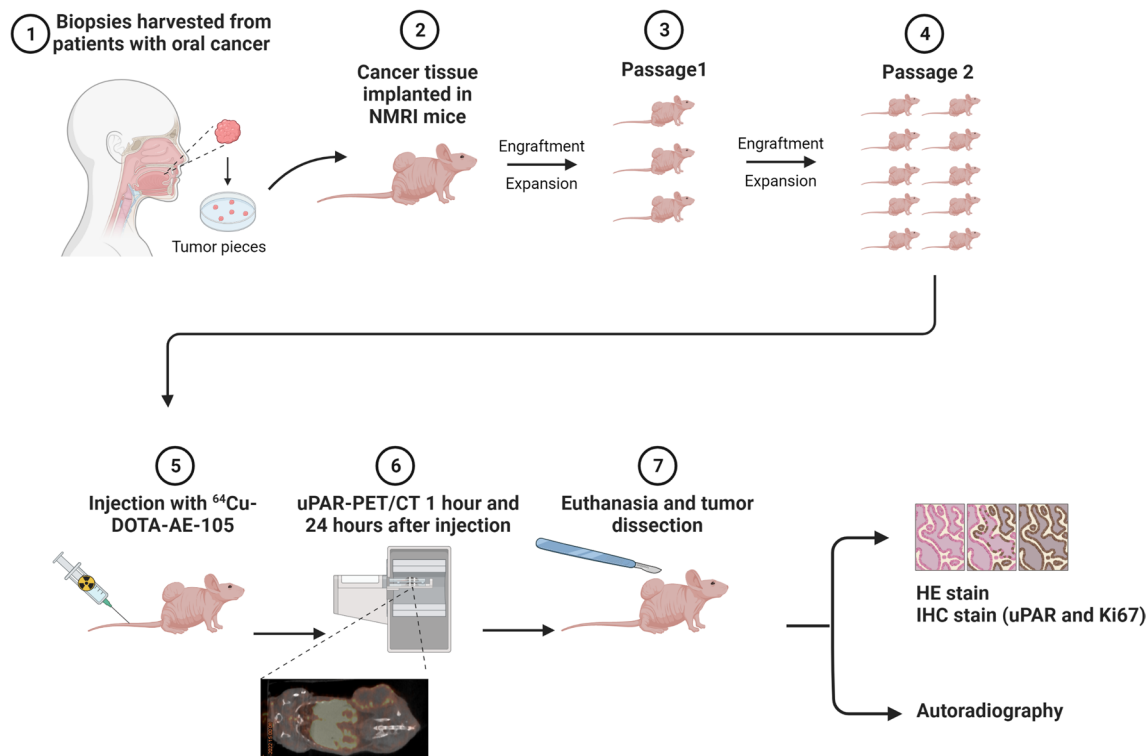

Fig. 1 An overview of the study design showing the establishment of patient-derived xenograft models from three primary OSCC tumors, uPAR-PET/CT of 9–10 mice (passage 2) per tumor model followed by *ex vivo* analysis. (Created with BioRender.com)

allowed to circulate in awake mice for 60 min before image acquisition. Images were analyzed as fused PET/CT images were circular regions of interest (ROIs) were drawn on CT images and superimposed on the fused PET image. ROIs were placed on every 4 slides in the axial plane on tumors and volumes calculated based on all ROIs in the tumor. Standardized uptake values (SUV), mean (SUV_{mean}), and max (SUV_{max}) were calculated for each tumor (more details in supplementary material).

Autoradiography

Cryosections of 30 µm were cut on a Cryostat CM1860 (Leica Biosystems) with corresponding muscle and tumor samples placed on the same glass slide. Glass slides were covered with plastic foil and exposed for 1 h against a phosphor imaging plate (BAS-IP MS 2040E, GE Healthcare, MA, USA) in a light-shed cassette. Following exposure, phosphor imaging plates were analyzed using the Amersham Biomolecular Imager system (GE Healthcare, MA, USA) at a resolution of 10 µm.

Immunohistochemistry

Formalin-fixated paraffin-embedded tumor samples from patients and the following PDX passages (0–2) were collected. Tumor samples from the P2 mice were gathered after the PET scan by sacrificing the animals. Three cross-sectional samples of the tumor were obtained and underwent hematoxylin and eosin (H&E) staining, Ki67 staining, and uPAR staining, respectively. All analysis was performed on 4 µm slides (see supplementary material for further details).

Histology and Immunohistochemistry Evaluation

The biological stability of the PDX tumors was evaluated by a specialized head and neck pathologist by comparing the histological characteristics of the original patient tumor to matched tumor tissue from P0, P1, and P2. The following characteristics were evaluated: nuclear pleomorphism, stromal proportion, inflammatory cell infiltration, degenerative changes, the invasive front, proliferation ratio by Ki67 expression, and uPAR expression. All IHC-stained tumor samples were digitally scored using the open-source software Qupath [36]. For each sample, the tumor compartment, excluding necrosis and cystic regions, was digitally annotated. Positive and negative cells were digitally identified within the tumor compartment based on the mean DAB signal in the cell cytoplasm. Cell expansion was set to 5 µm, and intensity threshold was for uPAR and Ki67 set to 0.12 and 0.20 for weak intensity (+1), 0.25 and 0.40 for moderate intensity (+2), and 0.50 and 0.6 for strong intensity (+3), respectively. The H-score was digitally calculated for the annotated tumor compartments by adding 3 × percentage of strongly stained cells, 2 × percentage of moderately stained cells, and 1 × percentage of weakly stained cells, resulting in a score ranging from 0 to 300 [37].

Statistical Analysis

Statistical analysis and bar charts were performed using GraphPad Prism version 9.3 for PC, GraphPad Software, La Jolla, CA, USA. To evaluate correlation between continuous variables, Pearson's R squared test was applied. The unpaired t-test was used to determine the differences between two groups containing continuous variables. To evaluate tumor growth, we measured the number of days from implantation to tumor volume of 400 mm3. The tumor growth for the different PDX models was then visualized using Kaplan–Meier analysis. To determine the relationship between biomarker expression and tumor progression, the number of days from implanthation to tumor volume of 400mm^3 was correlated to H-scores of uPAR and Ki67. Continuous variables were reported as mean ± standard deviation (SD) or median with range. A p-value of less than 0.05 was considered statistically significant.

Results

PDX Models

PDX models were established from primary tumors of three patients with OSCC. The clinicopathological characteristics for alle donor patients are shown in Table 1. All three models were derived from aggressive tumors, which is reflected in their tumor characteristics, prognosis, and postoperative treatment. All three patients had stage III or stage IV disease with moderate to poor differentiation, non-cohesive invasion pattern, and perineural invasion, and two patients had vascular invasion. The patients were surgical treated with excision of primary tumor and neck dissection, followed by postoperative radiotherapy. Two patients experienced local recurrence within 1 year of the primary operation.

For all models, we experienced an increasing tumor growth rate from initial implantation (P0) to the next passages. For the P2 models, the mean time from implantation to PET/CT was 67 days (range: 29–106 days). The median tumor size for P2 tumors at the time of PET/CT was 526 mm^3 (range 301–1371 mm^3).

Histological Stability of PDX Model Tumors Compared to Patient Tumor

To ensure that tumors from PDX models resembled the primary tumor from patients, histopathological characteristics

Table 1 Clinicopathological characteristics of the included OSCC patients

Characteristics	Donor patients for PDX models		
	Patient 1 (model 1)	Patient 2 (model 2)	Patient 3 (model 3)
Gender	Male	Male	Female
Age (years)	71	57	66
Tumor localization	Tongue	Floor of mouth	Floor of mouth
TNM stage (UICC 8)	T3N2bM0	T3N0M0	T2N2bM0
Depth of Invasion	8 mm	13 mm	10 mm
Perineural invasion	Yes	Yes	Yes
Vascular invasion	No	Yes	Yes
Pattern of invasion	Non-cohesive	Non-cohesive	Non-cohesive
HPV status	Negative	Negative	Negative
Histological grade of differentiation	Moderate	Poor	Moderate

of donor tumors and subsequent passages were examined (Fig. 2). We found unchanged pleomorphism, grade of degenerative changes (cystic formation, focal necrosis, and keratinization), and pattern of the invasive front through the passages. Similarly, the expression of uPAR in the cytoplasm, membrane, and surrounding stroma of tumor cells remained unchanged from patient tumor to the different PDX models (P0–P2). In all models, uPAR was expressed more strongly in the invasive front and around necrosis/cysts. The extent of necrosis/cysts observed was limited in size and confined to a minority of tumors. In later passages, the tumor compartment contained a slightly reduced amount of stroma, a greater density of tumor cells, and less inflammatory cell infiltration. The tumors effectively capture the heterogeneity of primary tumors in terms of uPAR expression, as seen by the variable levels of uPAR expression observed in tumor tissue among mice within each model and across different PDX models (Table 2).
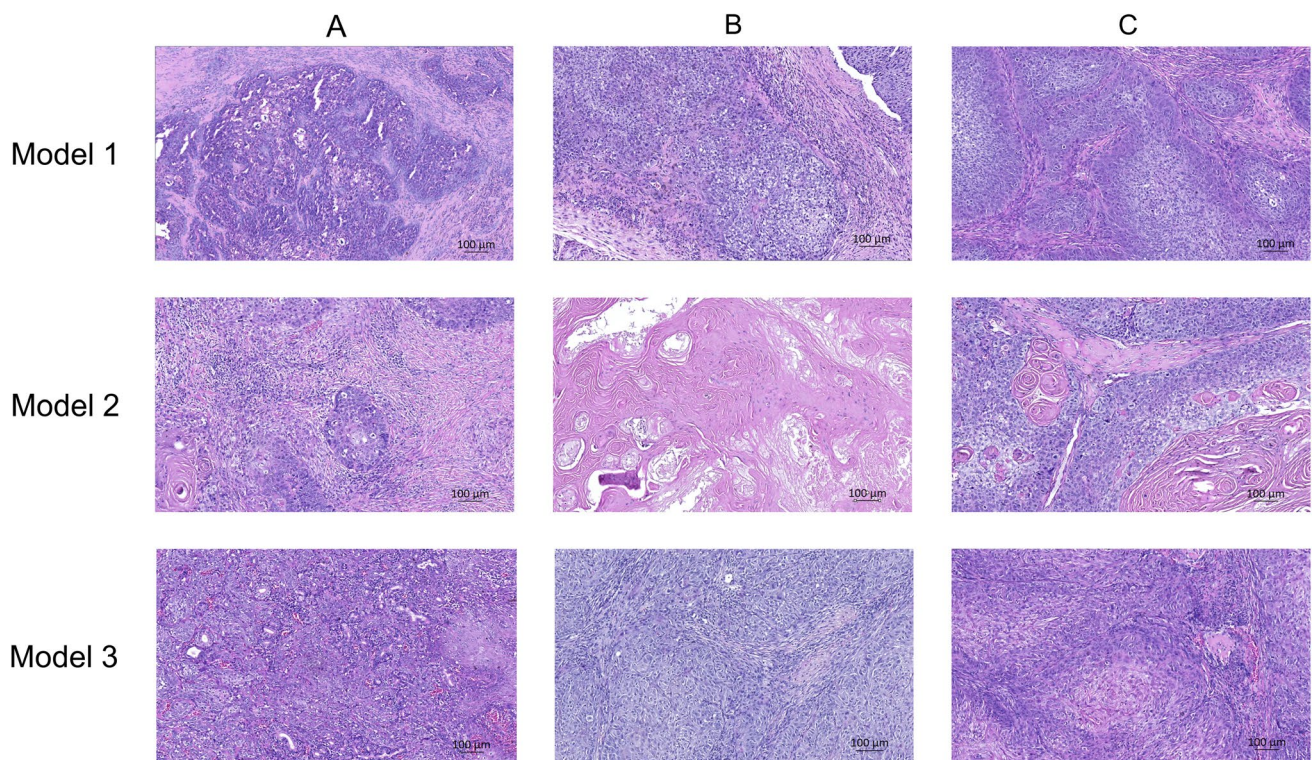
Fig. 2 Representative samples of HE-stained tumor tissue from all three models at various passages demonstrating the histological stability in tumor tissue from the patient tumor to passage 2 PDX tumors. **A** Patient tumors. **B** Tumor from passage 1 PDX models. **C** Tumor from passage 2 PDX models

Table 2 Digital quantification of uPAR expression in IHC-stained tumor tissue from all the PET/CT-scanned mice. The varying staining intensity of tumor cells displays the heterogenous uPAR expression in tumor tissue across the different models. The H-score was digitally calculated by adding 1 × percentage of weakly stained cells, 2 × percentage of moderately stained cells, and 3 × percentage of strongly stained cells, yielding a score between 0 and 300

| | PDX models | | |
uPAR expression	Model 1	Model 2	Model 3
Median H-score (range)	28.5 (11.5–96.5)	76.2 (58.8–98.2)	97.6 (70.7–127.7)
Median percentage of weakly stained tumor cells (range)	23.2 (10.1–65.9)	38.6 (20.8–44.1)	40.9 (39.2–50.9)
Median percentage of moderately stained tumor cells (range)	2.3 (0.6–13.7)	12.3 (8.5–18.7)	23.4 (11.9–36.2)
Median percentage of strongly stained tumor cells (range)	0.2 (0.1–1.1)	4.0 (1.9–9.4)	3.5 (0.7–8.5)
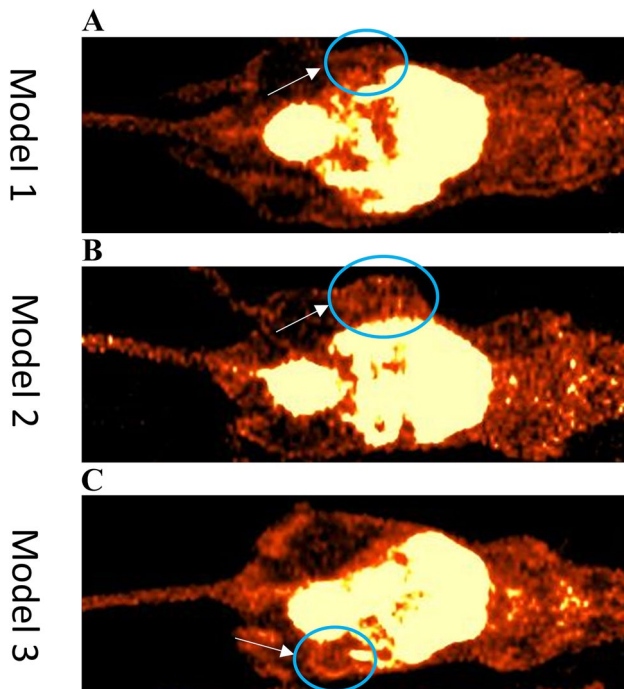
Fig. 3 ^{64}Cu-uPAR-PET/CT 1 h after tracer injection in three OSCC PDX models. White arrows indicate tumor lesions, all of them located in the flank. **A** Model 1 with low diffuse uptake. **B** Model 2 with high diffuse uptake. **C** Model 3 showing high uptake with hot spots and rim enhancement around cystic tumor lesion

Small-Animal PET/CT with [^{64}Cu]Cu-DOTA-AE105

All models (29 mice) showed uptake of [^{64}Cu]Cu-DOTA-AE105 in tumor compartment after both 1 h and 24 h. A heterogenic uptake pattern was seen in most tumors. A diffuse and lower uptake was seen in model 1 compared to the other models. Model 3 showed a generally higher uptake with hot spots in tumor tissue. Several tumors showed rim enhancement. Representative PET/CT images are shown in Fig. 3.

Ex Vivo Validation of [^{64}Cu]Cu-DOTA-AE105 Distribution Within Tumors

In Fig. 4, representative samples from each of the three PDX models show the uPAR expression determined by IHC staining in comparison to autoradiography of the same tumor. Topographically, the distribution of [^{64}Cu]Cu-DOTA-AE105 in tumor tissue corresponds to the uPAR expression pattern revealed by IHC staining. In model 1 and model 3, a low and high expression was seen, respectively. In model 2, the IHC-stained cystic degeneration in the tumor compartment was also visible on the autoradiography sample. The muscle samples showed minimal [^{64}Cu]Cu-DOTA-AE105 uptake on autoradiography for all PDX models confirming the low background uptake of the tracer and favorable tumor-to-muscle ratios.

All tumors expressed uPAR, but the H-score varied between the different models (Figs. 4 and 5A). The mean ± SD for SUV_{max} after 1 h for model 1, model 2, and model 3 was 1.50±0.24, 1.96±0.33, and 1.97±0.41, respectively. Significant difference in SUV_{max} values after 1 h was seen between model 1 and the two other models ($p=0.0018$). The same pattern was seen for uPAR expression (H-score) between the same models ($p<0.0001$) (Fig. 5B).

There was no significant positive correlation ($r = 0.34$; $p = 0.07$) between uPAR expression (H-score) and [^{64}Cu]Cu-DOTA-AE105 tumor uptake after 1 h (SUV_{max}) for all included tumor models (Fig. 6).

Correlation Between Tumor Growth and uPAR Expression

We found a significant correlation between uPAR expression (H-score) in the tumor compartment and the number of days from implantation to tumor volume of 400 mm^3 ($r=-0.40$, $p=0.03$), indicating that greater uPAR expression is associated with increased tumor growth rate (supplementary figure 1). No significant correlation was found between Ki67 expression and number of days from implantation to tumor volume of 400 mm^3.
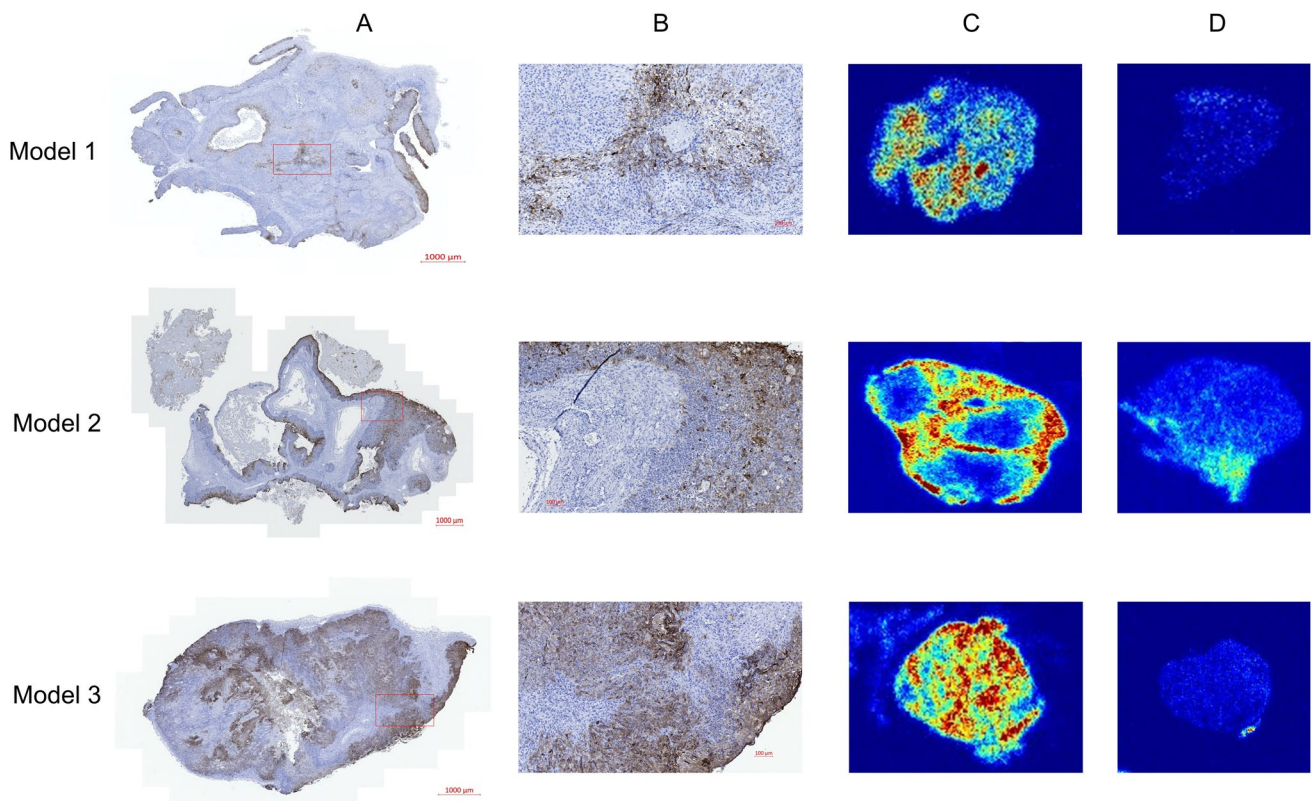
Fig. 4 uPAR expression in tumor tissue by immunohistochemistry in each of the three PET/CT-scanned OSCC PDX models and autoradiography of the same tumors after tracer injection. This figure depicts the positive correlation between tumor regions exhibiting high tracer uptake and tumor regions with elevated levels of uPAR expression. **A** Microscopic image with low magnification of uPAR expression in tumor. **B** Microscopic section of uPAR expression showing both positive and negative cells. **C** Autoradiography from primary tumor. **D** Autoradiography from normal quadriceps muscle from the same mice

Fig. 5 **A** Average SUV_{max} in tumor compartment for ^{64}Cu-DOTA-AE105 PET/CT for three different PDX models (model 1 ($n=9$), model 2 ($n=10$), model 3 ($n=10$)). **B** Mean uPAR expression in tumor tissue quantified with H-score for the same three PDX models
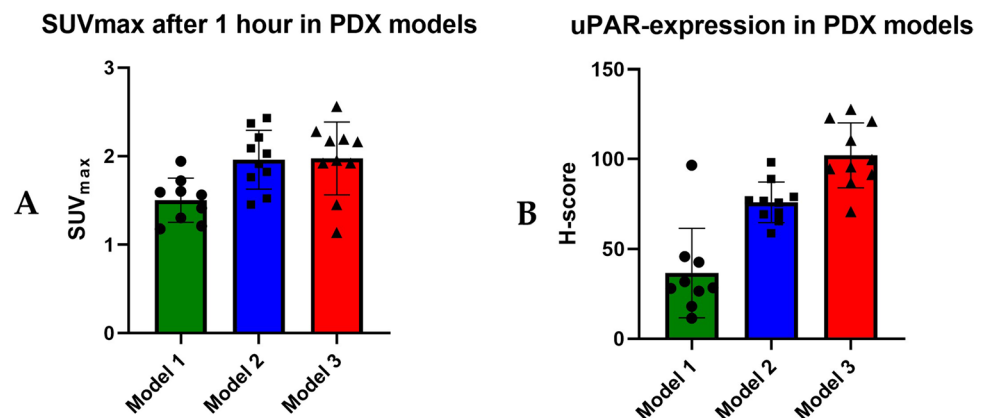
Discussion

We successfully established three novel PDX models of OSCC by engrafting patient-derived tumor tissue from locally advanced OSCC into immunodeficient mice. Importantly, the models maintained histological stability, heterogeneity, uPAR expression, and Ki67 expression through passages. In these three OSCC PDX models, we studied the use of [^{64}Cu]Cu-uPAR-PET/CT for imaging in a total of 29 tumors, a modality that has not previously been evaluated in head and neck cancer patients nor in heterogeneous preclinical PDX tumor models. We found a heterogenous tracer uptake in tumor tissue in all models. The tracer uptake and distribution in tumor were validated
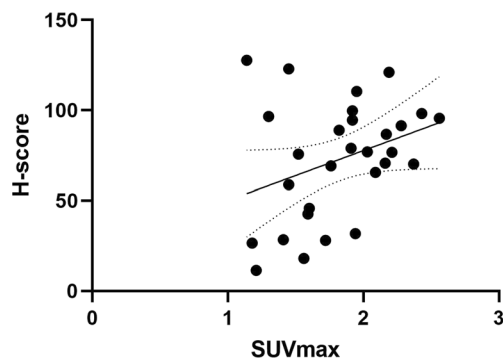
Fig. 6 Correlation between ^{64}Cu-uPAR-PET/CT SUV_{max} and uPAR expression, quantified with H-score, in tumor tissue from three different PDX models (n=29). No significant positive correlation was seen between SUVmax and H-score (r=0.34; p=0.07)

visually with autoradiography in comparison to IHC staining; however, quantitatively, there was no significant positive correlation between SUV_{max} and H-score. The lack of significant correlation may be due to the inherent limitations with IHC staining of tumor tissue which only samples a small section of the tumor, in contrast to PET imaging which captures the entire tumor. The tumor specificity of the tracer was demonstrated by the high autoradiography signal in tumor tissue compared to a minimal signal in samples from normal muscle. In addition, we observed a significant correlation between tumor growth and uPAR expression in the tumor compartment, demonstrating the prognostic potential of uPAR-targeted imaging in head and neck cancer.

These results indicate that OSCC PDX models can be used for investigating new molecular imaging modalities, such as ^{64}Cu-uPAR-PET/CT, and might resemble human tumor tissue better than the more homogenous cell line xenograft models. Especially, when exploring targets like uPAR, which is expressed on tumor-associated activated stromal cells. Our findings regarding the histological stability of PDX tumor tissue through passages are consistent with previous studies, in which it has been demonstrated that histological properties, biomarker expression, and mutational profile are stable through passages [35, 38–40]. Therapeutic response to anti-cancer therapy in PDX models has also been shown to resemble the clinical response in matched patients [35, 40]. However, it has also been demonstrated that the human stromal composition is only maintained for early passages, after which the murine stroma dominates, suggesting that early passages may be better at resembling the donor tumor [41].

So far, only a few studies have investigated the use of uPAR-targeted PET imaging in head and neck cancer, but several studies have examined this imaging modality in other cancer types. In preclinical studies, ^{64}Cu-labeled

uPAR-targeting radioligands have been explored in different cancer cell line xenograft models [42, 43], and the correlation between ^{64}Cu-DOTA-AE105 uptake in tumor and the uPAR expression was established by uPAR ELISA [43]. Other studies have investigated alternative chelators to DOTA [44] and established the dosimetry of ^{64}Cu-DOTA-AE105 for planning clinical trials [45]. In humans, ^{64}Cu-labeled PET imaging using ^{64}Cu-DOTA-AE105 has so far only been investigated in a phase I clinical trial in 10 patients with breast, prostate, and bladder cancer demonstrating tumor uptake and providing evidence for safe use [24]. In OSCC, ^{64}Cu-DOTA-AE105 has in a single preclinical cell line xenograft study demonstrated tracer-specific uptake in small orthotopic primary tongue tumors [25]. This current study is the first to study the use of ^{64}Cu-DOTA-AE105 PET/CT in heterogenous, i.e., PDX, head and neck cancers tissue. The target specificity of this tracer has not previously been shown in PDX models with autoradiography nor with comparison between uPAR expression (quantified as H-score) and SUV_{max} value. The pronounced association between uPAR expression and ^{64}Cu-DOTA-AE105 uptake found in this study has to our knowledge not previously been showed in cancer. These results emphasize the specificity of ^{64}Cu-DOTA-AE105 PET/CT for imaging uPAR positive cancer tissue.

Another uPAR-PET tracer labeled with [68]Ga (^{68}Ga-NOTA-AE105) has previously been investigated in head and neck cancer patients [21]. As the positron range for [64]Cu (1mm) is shorter than for [68]Ga (4mm), a ^{64}Cu-labeled uPAR-PET tracer, like ^{64}Cu-DOTA-AE105, may enhance detection of smaller tumor volumes as previously demonstrated by us in a head to head comparison of [68]Ga- and ^{64}Cu-labeled radiotracers targeting the somatostatin receptors in neuroendocrine tumors [23]. A tumor-specific imaging modality with high spatial resolution could have a significant impact on staging and treatment planning of patients with OSCC, particularly for those with early-stage disease with a high frequency of occult lymph node metastases. In addition, for studying tumor heterogeneity in a PDX model, the spatial resolution likewise is important.

We recently investigated the prognostic value of ^{68}Ga-uPAR-PET/CT in 54 patients with head and neck cancer and found that high SUV_{max} values in primary tumor was significantly associated with poor survival and proposed this modality as a future tool for selecting patients to uPAR-targeted radionuclide therapy [21]. This theranostic concept has previously been demonstrated in both colorectal and prostate cancer cell line models using DOTA-AE105 radiolabeled with ^{177}Lu for uPAR-targeted radionuclide therapy [9, 46]. Our OSCC PDX models, with a well characterized uPAR expression, could serve as a suitable translational platform

for development of uPAR-targeted radionuclide therapy or other uPAR-targeted antitumor treatment strategies [47] for OSCC.

Conclusions

We successfully established OSCC PDX models and demonstrated that their histological characteristics and uPAR expression closely resemble those of human tumors. [^{64}Cu] Cu-uPAR-PET/CT showed target- and tumor-specific uptake in OSCC PDX models demonstrating the diagnostic potential of this modality for OSCC patients. In addition, we found that uPAR expression in OSCC PDX tumors was correlated with tumor growth rate emphasizing the prognostic potential of this biomarker. These findings suggest that OSCC PDX models could serve as a valuable preclinical platform for evaluating uPAR-targeted molecular imaging and therapy modalities.

Supplementary Information The online version contains supplementary material available at https://doi.org/10.1007/s11307-023-01858-x.

Declarations

References

1. Sung H, Ferlay J, Siegel RL, Laversanne M, Soerjomataram I, Jemal A, Bray F (2021) Global Cancer Statistics 2020: GLOBOCAN estimates of incidence and mortality worldwide for 36 cancers in 185 countries. CA Cancer J Clin 71:209–249. https://doi.org/10.3322/CAAC.21660

2. Zanoni DK, Montero PH, Migliacci JC, Shah JP, Wong RJ, Ganly I, Patel SG (2019) Survival outcomes after treatment of cancer of the oral cavity (1985–2015). Oral Oncol 90:115–121. https://doi.org/10.1016/j.oraloncology.2019.02.001

3. De Angelis R, Sant M, Coleman MP, Francisci S, Baili P, Pierannunzio D, Trama A, Visser O, Brenner H, Ardanaz E et al (2014) Cancer survival in Europe 1999-2007 by country and age: results of EUROCARE-5-a population-based study. Lancet Oncol 15:23–34. https://doi.org/10.1016/S1470-2045(13)70546-1

4. Barrera JE, Miller ME, Said S, Jafek BW, Campana JP, Shroyer KR (2003) Detection of occult cervical micrometastases in patients with head and neck squamous cell cancer. Laryngoscope 113:892–896. https://doi.org/10.1097/00005537-200305000-00022

5. Schilling C, Stoeckli SJ, Haerle SK, Broglie MA, Huber GF, Sorensen JA, Bakholdt V, Krogdahl A, Von Buchwald C, Bilde A et al (2015) Sentinel European Node Trial (SENT): 3-year results of sentinel node biopsy in oral cancer. Eur J Cancer 51:2777–2784. https://doi.org/10.1016/j.ejca.2015.08.023

6. Amit M, Yen TC, Liao CT, Binenbaum Y, Chaturvedi P, Agarwal JP, Kowalski LP, Ebrahimi A, Clark JR, Cernea CR et al (2013) Clinical nodal stage is a significant predictor of outcome in patients with oral cavity squamous cell carcinoma and pathologically negative neck metastases: results of the international consortium for outcome research. Ann Surg Oncol 20:3575–3581. https://doi.org/10.1245/s10434-013-3044-0

7. Ding Z, Li Y, Pan X, Xuan M, Xie H, Wang X (2021) Sentinel lymph node biopsy versus elective neck dissection in squamous cell carcinoma of the oral cavity with a clinically n0 neck: systematic review and meta-analysis of prospective studies. Head Neck 43:3185–3198. https://doi.org/10.1002/HED.26803

8. D'Cruz AK, Vaish R, Kapre N, Dandekar M, Gupta S, Hawaldar R, Agarwal JP, Pantvaidya G, Chaukar D, Deshmukh A et al (2015) Elective versus therapeutic neck dissection in node-negative oral cancer. N Engl J Med 373:521–529. https://doi.org/10.1056/nejmoa1506007

9. Persson M, Juhl K, Rasmussen P, Brandt-Larsen M, Madsen J, Ploug M, Kjaer A (2014) UPAR targeted radionuclide therapy with 177Lu-DOTA-AE105 inhibits dissemination of metastatic prostate cancer. Mol Pharm 11:2796–2806. https://doi.org/10.1021/mp500177c

10. Quigley NG, Steiger K, Hoberück S, Czech N, Zierke MA, Kossatz S, Pretze M, Richter F, Weichert W, Pox C et al (2022) PET/CT imaging of head-and-neck and pancreatic cancer in humans by targeting the "cancer integrin" Avβ6 with Ga-68-trivehexin. Eur J Nucl Med Mol Imaging 49:1136–1147. https://doi.org/10.1007/S00259-021-05559-X

11. Durante S, Dunet V, Gorostidi F, Mitsakis P, Schaefer N, Delage J, Prior JO (2020) Head and neck tumors angiogenesis imaging

with 68Ga-NODAGA-RGD in comparison to 18F-FDG PET/CT: a pilot study. EJNMMI Res 10. https://doi.org/10.1186/S13550-020-00638-W

12. van Loon J, Even AJG, Aerts HJWL, Öllers M, Hoebers F, van Elmpt W, Dubois L, Dingemans AMC, Lalisang RI, Kempers P et al (2017) PET imaging of zirconium-89 labelled cetuximab: a phase I Trial in patients with head and neck and lung cancer. Radiother Oncol 122:267–273. https://doi.org/10.1016/j.radonc.2016.11.020

13. Schöder H, de Souza França PD, Nakajima R, Burnazi E, Roberts S, Brand C, Grkovski M, Mauguen A, Dunphy MP, Ghossein RA et al (2020) Safety and feasibility of PARP1/2 imaging with 18F-PARPi in patients with head and neck cancer. Clin Cancer Res 26:3110–3116. https://doi.org/10.1158/1078-0432.CCR-19-3484

14. Noh H, Hong S, Huang S (2013) Role of urokinase receptor in tumor progression and development. Theranostics 3:487–495

15. Dass K, Ahmad A, Azmi AS, Sarkar SH, Sarkar FH (2008) Evolving role of UPA/UPAR system in human cancers. Cancer Treat Rev 34:122–136. https://doi.org/10.1016/j.ctrv.2007.10.005

16. Lawaetz M, Christensen A, Juhl K, Karnov K, Lelkaitis G, Fiehn A-MK, Kjaer A, von Buchwald C (2023) Potential of UPAR, Avβ6 integrin, and tissue factor as targets for molecular imaging of oral squamous cell carcinoma: evaluation of nine targets in primary tumors and metastases by immunohistochemistry. Int J Mol Sci 24:3853. https://doi.org/10.3390/IJMS24043853

17. Christensen A, Kiss K, Lelkaitis G, Juhl K, Persson M, Charabi BW, Mortensen J, Forman JL, Sørensen AL, Jensen DH et al (2017) Urokinase-type plasminogen activator receptor (uPAR), tissue factor (TF) and epidermal growth factor receptor (EGFR): tumor expression patterns and prognostic value in oral cancer. BMC Cancer 17. https://doi.org/10.1186/s12885-017-3563-3

18. Boonstra MC, Verspaget HW, Ganesh S, FJGM K, Vahrmeijer AL, CJH v d V, PJK K, PHA Q, CFM S (2011) Clinical applications of the urokinase receptor (UPAR) for cancer patients. Curr Pharm Des 17:1890–1910. https://doi.org/10.2174/138161211796718233

19. Fosbøl MØ, Kurbegovic S, Johannesen HH, Røder MA, Hansen AE, Mortensen J, Loft A, Petersen PM, Madsen J, Brasso K et al (2021) Urokinase-type plasminogen activator receptor (UPAR) PET/MRI of prostate cancer for noninvasive evaluation of aggressiveness: comparison with gleason score in a prospective phase 2 clinical trial. J Nucl Med 62:354. https://doi.org/10.2967/JNUMED.120.248120

20. Carlsen EA, Loft M, Loft A, Berthelsen AK, Langer SW, Knigge U, Kjaer A (2022) Prospective phase II trial of prognostication by 68Ga-NOTA-AE105 uPAR PET in patients with neuroendocrine neoplasms: implications for uPAR targeted therapy. J Nucl Med 63(9):1371–1377. https://doi.org/10.2967/JNUMED.121.263177

21. Risør LM, Clausen MM, Ujmajuridze Z, Farhadi M, Andersen KF, Loft A, Friborg J, Kjaer A (2022) Prognostic value of urokinase-type plasminogen activator receptor PET/CT in head and neck squamous cell carcinomas and comparison with 18F-FDG-PET/CT: a single-center prospective study. J Nucl Med 63(8):1169–1176. https://doi.org/10.2967/jnumed.121.262866

22. Ploug M, Østergaard S, Gårdsvoll H, Kovalski K, Holst-Hansen C, Holm A, Ossowski L, Danø K (2001) Peptide-derived antagonists of the urokinase receptor. Affinity maturation by combinatorial chemistry, identification of functional epitopes, and inhibitory effect on cancer cell intravasation. Biochemistry 40:12157–12168. https://doi.org/10.1021/bi010662g

23. Johnbeck CB, Knigge U, Loft A, Berthelsen AK, Mortensen J, Oturai P, Langer SW, Elema DR, Kjaer A (2017) Head-to-head comparison of 64Cu-DOTATATE and 68Ga-DOTATOC PET/CT: a prospective study of 59 patients with neuroendocrine tumors. J Nucl Med 58:451–457. https://doi.org/10.2967/jnumed.116.180430

24. Persson M, Skovgaard D, Brandt-Larsen M, Christensen C, Madsen J, Nielsen CH, Thurison T, Klausen TL, Holm S, Loft A et al (2015) First-in-human UPAR PET: imaging of cancer aggressiveness. Theranostics 5:1303. https://doi.org/10.7150/THNO.12956

25. Christensen A, Juhl K, Persson M, Charabi BW, Mortensen J, Kiss K, Lelkaitis G, Rubek N, von Buchwald C, Kjær A (2017) UPAR-targeted optical near-infrared (NIR) fluorescence imaging and PET for image-guided surgery in head and neck cancer: proof-of-concept in orthotopic xenograft model. Oncotarget 8:15407–15419. https://doi.org/10.18632/oncotarget.14282

26. Abdolahi S, Ghazvinian Z, Muhammadnejad S, Saleh M, Asadzadeh Aghdaei H, Baghaei K (2022) Patient-derived xenograft (PDX) models, applications and challenges in cancer research. J Transl Med 20. https://doi.org/10.1186/S12967-022-03405-8

27. Izumchenko E, Paz K, Ciznadija D, Sloma I, Katz A, Vasquez-Dunddel D, Ben-Zvi I, Stebbing J, McGuire W, Harris W et al (2017) Patient-derived xenografts effectively capture responses to oncology therapy in a heterogeneous cohort of patients with solid tumors. Ann Oncol 28:2595. https://doi.org/10.1093/ANNONC/MDX416

28. Julien S, Merino-Trigo A, Lacroix L, Pocard M, Goéré D, Mariani P, Landron S, Bigot L, Nemati F, Dartigues P et al (2012) Characterization of a large panel of patient-derived tumor xenografts representing the clinical heterogeneity of human colorectal cancer. Clin Cancer Res 18:5314–5328. https://doi.org/10.1158/1078-0432.CCR-12-0372/85035/AM/CHARACTERIZATION-OF-A-LARGE-PANEL-OF-PATIENT

29. Illemann M, Bird N, Majeed A, Lærum OD, Lund LR, Danø K, Nielsen BS (2009) Two distinct expression patterns of urokinase, urokinase receptor and plasminogen activator inhibitor-1 in colon cancer liver metastases. Int J Cancer 124:1860–1870. https://doi.org/10.1002/ijc.24166

30. Jacobsen B, Ploug M (2008) The urokinase receptor and its structural homologue c4.4a in human cancer: expression, prognosis and pharmacological inhibition. Curr Med Chem 15:2559–2573. https://doi.org/10.2174/092986708785909012

31. Seshadri M, Merzianu M, Tang H, Rigual NR, Sullivan M, Loree TR, Popat SR, Repasky EA, Hylander BL (2009) Establishment and characterization of patient tumor-derived head and neck squamous cell carcinoma xenografts. Cancer Biol Ther 8(23):2275–83

32. Kimple RJ, Harari PM, Torres AD, Yang RZ, Soriano BJ, Yu M, Armstrong EA, Blitzer GC, Smith MA, Lorenz LD et al (2013) Development and characterization of HPV-positive and HPV-negative head and neck squamous cell carcinoma tumorgrafts. Clin Cancer Res 19:855–864. https://doi.org/10.1158/1078-0432.CCR-12-2746

33. Peng S, Creighton CJ, Zhang Y, Sen B, Mazumdar T, Myers JN, Woolfson A, Lorenzi MV, Bell D, Williams MD et al (2013) Tumor grafts derived from patients with head and neck squamous carcinoma authentically maintain the molecular and histologic characteristics of human cancers. J Transl Med 11. https://doi.org/10.1186/1479-5876-11-198

34. Cosper PF, Abel L, Lee YS, Paz C, Kaushik S, Nickel KP, Alexandridis R, Scott JG, Bruce JY, Kimple RJ (2020) Patient derived models to study head and neck cancer radiation response. Cancers (Basel) 12(2):419

35. Kang HN, Kim JH, Park AY, Choi JW, Lim SM, Kim J, Shin EJ, Hong MH, Pyo KH, Yun MR et al (2020) Establishment and characterization of patient-derived xenografts as paraclinical models for head and neck cancer. BMC Cancer 20. https://doi.org/10.1186/s12885-020-06786-5

36. Bankhead P, Loughrey MB, Fernández JA, Dombrowski Y, McArt DG, Dunne PD, McQuaid S, Gray RT, Murray LJ, Coleman HG et al (2017) QuPath: open source software for digital pathology image analysis. Sci Rep 7. https://doi.org/10.1038/S41598-017-17204-5

37. Goulding H, Pinder S, Cannon P, Pearson D, Nicholson R, Snead D, Bell J, Elston CWE, Robertson JF, Blamey RW et al (1995) A new immunohistochemical antibody for the assessment of estrogen receptor status on routine formalin-fixed tissue samples. Hum Pathol 26:291–294. https://doi.org/10.1016/0046-8177(95)90060-8

38. Swick AD, Stein AP, McCulloch TM, Hartig GK, Ong IM, Sampene E, Prabakaran PJ, Liu CZ, Kimple RJ (2017) Defining the boundaries and expanding the utility of head and neck cancer patient derived xenografts. Oral Oncol 64:65. https://doi.org/10.1016/J.ORALONCOLOGY.2016.11.017

39. Campbell KM, Lin T, Zolkind P, Barnell EK, Skidmore ZL, Winkler AE, Law JH, Mardis ER, Wartman LD, Adkins DR et al (2018) Oral cavity squamous cell carcinoma xenografts retain complex genotypes and intertumor molecular heterogeneity. Cell Rep. 24:2167–2178. https://doi.org/10.1016/j.celrep.2018.07.058

40. Makita H, Endo K, Kasahara Y, Nakata A, Moriyama-Kita M, Ishikawa K, Ueno T, Nakanishi Y, Kondo S, Wakisaka N et al (2021) Xenografts derived from patients with head and neck cancer recapitulate patient tumour properties. Oncol Lett 21. https://doi.org/10.3892/OL.2021.12646

41. Rosfjord E, Lucas J, Li G, Gerber HP (2014) Advances in patient-derived tumor xenografts: from target identification to predicting clinical response rates in oncology. Biochem Pharmacol 91:135–143

42. Li ZB, Niu G, Wang H, He L, Yang L, Ploug M, Chen X (2008) Imaging of urokinase-type plasminogen activator receptor expression using a 64cu-labeled linear peptide antagonist by MicroPET. Clin Cancer Res 14:4758–4766. https://doi.org/10.1158/1078-0432.CCR-07-4434

43. Persson M, Madsen J, Østergaard S, Jensen MM, Jørgensen JT, Juhl K, Lehmann C, Ploug M, Kjaer A (2012) Quantitative PET of human urokinase-type plasminogen activator receptor with 64Cu-DOTA-AE105: implications for visualizing cancer invasion. J Nucl Med 53:138–145. https://doi.org/10.2967/jnumed.110.083386

44. Persson M, Hosseini M, Madsen J, Jørgensen TJD, Jensen KJ, Kjaer A, Ploug M (2013) Improved PET imaging of UPAR expression using new 64Cu-labeled cross-bridged peptide ligands: comparative *in vitro* and *in vivo* studies. Theranostics 3:618. https://doi.org/10.7150/THNO.6810

45. Persson M, El Ali HH, Binderup T, Pfeifer A, Madsen J, Rasmussen P, Kjaer A (2014) Dosimetry of 64Cu-DOTA-AE105, a PET tracer for UPAR imaging. Nucl Med Biol 41:290–295. https://doi.org/10.1016/j.nucmedbio.2013.12.007

46. Persson M, Rasmussen P, Madsen J, Ploug M, Kjaer A (2012) New peptide receptor radionuclide therapy of invasive cancer cells: *in vivo* studies using 177 Lu-DOTA-AE105 targeting UPAR in human colorectal cancer xenografts. Nucl Med Biol 39:962–969. https://doi.org/10.1016/j.nucmedbio.2012.05.007

47. Zhai BT, Tian H, Sun J, Zou JB, Zhang XF, Cheng JX, Shi YJ et al (2022) Urokinase-type plasminogen activator receptor (uPAR) as a therapeutic target in cancer. J Transl Med 20. https://doi.org/10.1186/s12967-022-03329-3